The Growth and Enrichment of the Intragroup Gas

by

Lichen Liang
B.Sc., Zhejiang University, 2011

A Thesis Submitted in Partial Fulfillment of the
Requirements for the Degree of

MASTER OF SCIENCE

in the Department of Physics and Astronomy

The Growth and Enrichment of the Intragroup Gas

by

Lichen Liang
B.Sc., Zhejiang University, 2011

Supervisory Committee

Dr. Arif Babul, Supervisor
(Department of Physics and Astronomy)

Dr. Christopher Pritchet, Departmental Member
(Department of Physics and Astronomy)

Dr. Alexandre Brolo, Outside Member
(Department of Chemistry)

Supervisory Committee

Dr. Arif Babul, Supervisor
(Department of Physics and Astronomy)

Dr. Christopher Pritchet, Departmental Member
(Department of Physics and Astronomy)

Dr. Alexandre Brolo, Outside Member
(Department of Chemistry)

ABSTRACT

The observable properties of galaxy groups, and especially the thermal and chemical properties of the intragroup medium (IGrM), provide important constraints on the different feedback processes associated with massive galaxy formation and evolution. In this work, we present a detailed analysis of the global properties of simulated galaxy groups with X-ray temperatures in the range $0.5 - 2$ keV over the redshift range $0 \leq z \leq 3$. The groups are drawn from a cosmological smoothed particle hydrodynamics simulation that includes a well-constrained prescription for momentum-driven, galactic outflows powered by stars and supernovae but no explicit treatment of AGN feedback. Our aims are (a) to establish a baseline against which we will compare future models; (b) to identify model successes that are genuinely due to stellar/supernovae-powered outflows; and (c) to pinpoint mismatches that not only signal the need for AGN feedback but also constrain the nature of this feedback.

We find that even without AGN feedback, our simulation successfully reproduces the observed present-day group properties such as the IGrM mass fraction, the various X-ray luminosity-temperature-entropy scaling relations, as well as both the mass-weighted and the emission-weighted IGrM iron and silicon abundance versus IGrM temperature relationships, for all but the most massive groups. We also show that these trends evolve self-similarly for $z < 1$, in agreement with the observations. In

contrast to the usual expectations, we do not see any evidence of the IGrM undergoing catastrophic cooling. And yet, the $z = 0$ group stellar mass is a factor of ~ 2 too high. Probing further, we find that the latter is due to the build-up of cold gas in the massive galaxies *before* they are incorporated inside groups. This not only indicates that another feedback mechanism must activate as soon as the galaxies achieve $M_* \approx$ a few $\times 10^{10}$ $M_\odot$ but that this feedback mechanism must be powerful enough to expel a significant fraction of the halo gas component from the galactic halos. "Maintenance-mode" AGN feedback of the kind observed in galaxy clusters will not do. At the same time, we find that stellar/supernovae-powered winds are essential for understanding the metal abundances in the IGrM and these results are expected to be relatively insensitive to the addition of AGN feedback.

We further examine the detailed distribution of the metals within the groups and their origin. We find that our simulated abundance profiles fit the observational data pretty well except that in the innermost regions, there appears to have an excess of metals in the IGrM, which is attributed to the overproduction of stars in the central galaxies. The fractional contribution of the different types of galaxies varies with radial distances from the group center. While the enrichment in the core regions of the groups is dominated by the central and satellite galaxies, the external galaxies become more important contributors to the metals at $r \gtrsim R_{500}$. The IGrM at the groups' outskirts is enriched at comparatively higher redshifts, and by relatively less massive galaxies.

Contents

List of Figures

List of Special Terms, Abbreviations and Acronyms Used in this Thesis

Term	Definition
A&A	Astronomy & Astrophysics
AJ	Astronomical Journal
ApJ	Astrophysical Journal
ArXiv	astro-ph preprint server
ApJS	Astrophysical Journal Supplement Series
ARA&A	Annual Review of Astronomy and Astrophysics
MNRAS	Monthly Notice of the Royal Astronomical Society
PASJ	Publications of the Astronomical Society of Japan
PASP	Publications of the Astronomical Society of the Pacific
AGB	asymptotic giant branch
AGN	active galactic nucleus
CDM	cold dark matter
CMB	cosmic microwave background
GMC	giant molecular cloud
GR	general relativity
HBI	heat flux driven buoyancy instability
ICM	intra-cluster medium
IGM	inter-galactic medium
IGrM	intra-group medium
IMF	initial mass function
IGS	intra-group star
ISM	intersteller medium
MMP	most massive progenitor
MTI	magnetothermal instability
SMBH	supermassive blackhole
SN/SNe	supernova/supernovae (plural)
UV	ultra-violet
WMAP	Wilkinson Microwave Anistropy Probe

Chandra	space-based X-ray telescope
XMM-Newton	space-based X-ray telescope

ACKNOWLEDGEMENTS

There are so many people to whom I would like to deliver my sincere thanks for their support during my master work, without which this work could not have been completed.

First of all, I would like to acknowledge my thesis supervisor, Prof. Arif Babul, for taking me as his master student, guiding me through the research and providing me with financial support. Special thanks should be delivered to him for his impact on my way of conveying physics concepts. He made me realize that verbal description is as important as math, and in many cases, it gives the sign of true understanding.

I would like to thank Prof. Chris Pritchet and Prof. Alex Brolo for being in my supervisory committee and providing me with many insightful questions and discussions, which have helped me a lot with my research and thesis. I also thank the external examiner, Prof. Afzal Suleman, for his careful reading of my thesis.

Thanks Dr. Fabrice Durier for the time he has devoted to my project, for attending my talks and giving me helpful feedback every time. He teaches me professionality.

Thanks to the administrative staff in the department who have done a great job in keeping me on track in the grad school, including Megan, Amanda and Michelle. I am also grateful to Stephenson for his 24/7 help in resolving my computer problems. He is incredibly supportive.

Among many of my young friends, I would like to express my deepest gratitude to Christian, Epson and Farbod, for offering me so much fun and joy in Victoria, sharing my concerns and supporting me when I face difficulties. I cherish the time we have had together.

To my fellow astronomy graduate students, thanks for creating such a wonderful atmosphere in the department and offering me so much great help. A special thank you goes to Divya, Ivar, Matthias, Connor, Jared, Steve, Mike, Charli and Hannah. I appreciate the time with all of you.

"A path is made by walking on it."

Zhuang Tzu

DEDICATION

Dedicated to my mother, for her constant support.

Chapter 1

INTRODUCTION

Galaxy formation and evolution is one of the most challenging problems in modern physical cosmology. With the advancement in instrumentation and observational techniques, emerging evidence has revealed that galaxies are not simply isolated systems of stars, but they and their structural environment should be viewed as a ecosystem where there is frequent exchange of matter and energy. Understanding this galaxy-environment interplay is essential for comprehending many of the observable properties of both galaxies and their environment.

This thesis attempts to study such interplay using a large-scale cosmological hydrodynamic simulation. In Section 1.1, we introduce the readers to the cosmological framework for this work and as well as some physical quantities and concepts essential for describing the simulation setup in the next chapter. In Section 1.2, we will review the recent efforts to use galaxy groups and clusters as probes for cosmology and astrophysics and the reasons why groups are particularly interesting systems for study on galaxy formation and evolution. We will than present the detailed aims, followed by the outline of this thesis in Section 1.3.

1.1 The Cosmology

Modern cosmological models are based on the presumption that the Universe is, on sufficiently large scales, homogeneous and isotropic. In other words, if we consider some large volume, the average properties of the Universe is independent of where the volume is located, and that the universe looks the same in every direction. This presumption has been confirmed by a wide variety of modern observations, such as

the number counts of galaxies and radio sources on very large scales, the Lyman-α forest distribution, the X-ray background (XRB), and the 3K cosmic microwave background (CMB).

In 1915, Einstein proposed the General Theory of Relativity (GR), which described gravity as the geometric property of space and time (or spacetime). In particular, the curvature of spacetime is related to the matter/energy distribution through Einstein's field equations. In the 1920s and 1930s, A. Friedmann, G. Lemaître, H. P. Robertson, and A.G. Walker independently found a (metric) solution to Einstein's field equations that characterizes the homogeneity and isotropy of Universe on large scales:

$$ds^2 = c^2dt^2 - a^2(t)[\frac{dr^2}{1-Kr^2} + r^2(d\theta^2 + sin^2\theta d\phi^2)], \tag{1.1}$$

where r,θ, and ϕ are called the co-moving coordinates, c is the speed of light, K represents the curvature, a is the scale factor that accounts for the expansion of the Universe and t is the proper time of the fundamental observers (*i.e.,*the observers whose co-moving position is fixed). Substituting this metric into Einstein's field equations, it is straightforward to obtain a set of partial differential equations which yield both the curvature and the time evolution of the Universe as a function of its matter/energy density, called the Friedmann's equations. Specifically, for a given rate of expansion, $H = \dot{a}/a$, there exists a critical density,

$$\rho_{\rm crit} = \frac{3H^2}{8\pi G}, \tag{1.2}$$

which will yield a spatially flat ($K = 0$) Universe, and an over/under-dense Universe will be spatially closed/open ($K = -1/K = 1$). For a Universe comprised of pressure-less matter, radiation and vacuum energy (dark energy), of which the densities are ρ_m, ρ_r and ρ_Λ, respectively, $a(t)$ can be obtained by integrating the following equation (Mo, van den Bosch & White, 2010):

$$\frac{\dot{a}}{a} = H_0E(a), \tag{1.3}$$

where

$$E(a)^2 = \Omega_{r,0}a^{-4} + \Omega_{m,0}a^{-3} + \Omega_{\Lambda,0} + (1-\Omega_0)a^{-2}, \tag{1.4}$$

with $\Omega_{i,0} = \rho_{i,0}/\rho_{\rm crit,0}$ ($i = m, r$,or Λ), and $\Omega_0 = \Sigma_i\Omega_{i,0}$=$1 + Kc^2/H_0^2$. The subscripts "0" denote that the quantities are measured at present day, *i.e.,*$z = 0$. The first two terms on the right of equation (1.4) imply that the particle number density is diluted

as the Universe expands ($n \propto a^{-3}$), while photons also have their energy reduced as a^{-1} by the redshift; the third term infers that the dark energy has density independent of volume; and the last term vanishes for a spatially flat Universe ($\Omega_0 = 1$). As shown by the above expressions, the dynamics of the Universe can be fully constrained by the four measurable parameters H_0 and $\Omega_{i,0}$. The values for these parameters obtained from the recent 9-year Wilkinson Microwave Anisotropy Probe (WMAP) survey are (Hinshaw et al., 2013)

$$\begin{aligned} H_0 = 100\ h = 69.7\ \mathrm{km\ s^{-1}\ Mpc^{-1}}, \\ \Omega_{m,0} = 0.28, \Omega_\Lambda = 0.72 \text{ and } \Omega_{r,0} = 8.5 \times 10^{-5}, \end{aligned} \tag{1.5}$$

indicating that we are currently living in a dark energy-dominated, spatially flat ($K \sim \Omega_0 - 1 = 0$) Universe in accelerated expansion.

While the general properties of the Universe is very close to being homogeneous on very large scales, it is also characterized by a wealth of detail on the scales ranging from single galaxies to over 100 Mpc at present day. A fundamental assumption of modern cosmology is that the lumpy distribution of galaxies and their clusters develop from the growth of the gravitationally unstable fluctuations in the matter density field $\rho_m(\mathbf{x}, t)$. Most cosmologists today believe that the Universe has undergone a period of exponential growth called *inflation*. During this period, quantum perturbations on the microscopic scales are magnified to cosmic size, are "frozen-in" as classical matter density fluctuations, and eventually become the seeds for all structures in the Universe.

The ordinary baryonic matter accounts for approximately 1/5 of the cosmic matter, whereas the remaining bulk is believed to be nonbaryonic "dark matter" that does not experience strong or electromagnetic interactions. Though there has been no confirmed detection of any dark matter particle to date, many of its properties are constrained by the observable structures in the Universe. In particular, dark matter is thought to decouple from radiation not too long after it becomes non-relativistic at $t \sim 10^{-9}$ s, with the mass enclosed within the horizon (*i.e.,*the furthest distance within which two events can have casual relationship) being $\ll M_\odot$ at its decoupling. This indicates that fluctuations in dark matter field can survive from suppression by free-steaming on all scales of astrophysical interest, which is essential for galaxy formation as the baryon fluctuations are almost erased within the scales of ≈ 10 Mpc

comoving at $t \sim 378,000$ yrs ($z \simeq 1100$) due to the Silk damping effect, with enclosed baryon mass of $\sim 10^{14} M_{\odot}$ being smoothed. Thanks to the small-scale fluctuations having persisted in the dark-matter density field, the baryonic matter subsequently falls into the potential wells which they generate and the fluctuations in both baryonic and dark matter essentially co-evolve from then on.

It is a useful first order approximation to neglect the impact from baryons when modelling the evolution of density fluctuations in cosmic matter given that the collisionless dark matter dominates in mass, and therefore the gravitational forces involved. Using the continuity, Euler and Poisson equations, it can be shown that the overdensity of cosmic matter, $\delta(\mathbf{x}, t) \equiv \frac{\rho_m(\mathbf{x},t)}{\overline{\rho_m}(t)} - 1$, follows the equation

$$\frac{d^2\delta}{dt^2} + 2\frac{\dot{a}}{a}\frac{d\delta}{dt} = 4\pi G\overline{\rho_m}\delta, \text{ for } \delta \ll 1, \tag{1.6}$$

where $\overline{\rho_m}$ is the average density of matter over a sufficiently large volume at time t, within which the Universe can be viewed as homogeneous. This equation has two solutions, but only one of them represents growing perturbations with time, which can be approximated by $\delta_{m+} = g(z)/(1+z) \propto D(z)$, where (Carroll, Press & Turner, 1992)

$$g(z) \approx \frac{5}{2}\Omega_m(z)\left\{\Omega_m^{4/7}(z) - \Omega_\Lambda(z) + [1 + \frac{1}{2}\Omega_m(z)][1 + \frac{1}{70}\Omega_\Lambda(z)]\right\}^{-1} \tag{1.7}$$

and $D(z)$ is called the linear growth factor. This solution becomes invalid once the perturbations enter the nonlinear regime, *i.e.,*δ is of order of unity. To follow the nonlinear structure growth, one has to adopt an alternative approach. A good approximate model is the spherical collapse model. Consider a spherically symmetric density fluctuation at some time t_i, such that the volume-averaged overdensity within its radius r_i is $\delta_i \ll 1$. The total mass enclosed within the shell is therefore

$$M = \frac{4}{3}\pi(1 + \delta_i)\overline{\rho_m}(t_i)r_i^3. \tag{1.8}$$

In a universe with non-zero cosmological constant, the motion of the mass shell is given by

$$\frac{d^2r(t)}{dt^2} = -\frac{GM}{r^2(t)} + \frac{\Lambda}{3}r, \tag{1.9}$$

where the first and second terms on the right side, respectively, represent the gravitational attraction by the interior mass M, being a constant provided no mass flow across the shell, and the repulsion resulting from the cosmological constant, $\Lambda = 3H^2\Omega_\Lambda$, through an effective density $\rho + 3P/c^2 = -2\rho = -\Lambda c^2/(4\pi G)$. Integrating equation (1.9) once we obtain

$$\frac{1}{2}\Big(\frac{dr}{dt}\Big)^2 - \frac{GM}{r} - \frac{\Lambda c^2}{6}r^2 = \mathcal{E}, \tag{1.10}$$

where $\mathcal{E}$ is a constant. Since $dr/dt = 0$ when the shell reaches its maximum radius, $r_{\rm max}$, we have $-GM/r_{\rm max} - \Lambda c^2/6r_{\rm max}^2 = \mathcal{E}$. The solution of equation (1.10) can then be written as (Mo, van den Bosch & White, 2010)

$$t = \begin{cases} \frac{1}{H_0}\Big(\frac{\zeta}{\Omega_{\Lambda,0}}\Big)^{1/2}\int_0^{r/r_{\rm max}} dx\ [\frac{1}{x} - 1 + \zeta(x^2-1)]^{-1/2} \ \ (r \le r_{\rm max}), \\ \\ t_{\rm max} + \frac{1}{H_0}\Big(\frac{\zeta}{\Omega_{\Lambda,0}}\Big)^{1/2}\int_{r/r_{\rm max}}^1 dx\ [1 - \frac{1}{x} - \zeta(x^2-1)]^{-1/2} \ \ (r > r_{\rm max}), \end{cases} \tag{1.11}$$

where

$$t_{\rm max} = \frac{1}{H_0}\Big(\frac{\zeta}{\Omega_{\Lambda,0}}\Big)^{1/2}\int_0^1 dx\ [\frac{1}{x} - 1 + \zeta(x^2-1)]^{-1/2} \tag{1.12}$$

is the time of maximum expansion and

$$\zeta \equiv (\Lambda c^2 r_{\rm max}^3/6GM) < 1/2, \tag{1.13}$$

with the inequity following from $\ddot{r} < 0$ at $r = r_{\rm max}$. It can be proved that in an early flat Universe ($\Omega_\Lambda + \Omega_m = 1$), when $t_i \ll t_0$ and $r_i \ll r_{\rm max}$, the initial overdensity δ_i can be written as (Mo, van den Bosch & White, 2010)

$$\delta_i = \frac{3}{5}(1+\zeta)\Big(\frac{\omega_i}{\zeta}\Big)^{1/3}, \tag{1.14}$$

where $\omega_i = \Omega_\Lambda(t_i)/\Omega_m(t_i) = (\Omega_{\Lambda,0}/\Omega_{m,0})(1+z_i)^{-3} = \Omega_{m,i}^{-1} - 1$. Assuming that this perturbation collapses at $t_{\rm col} = 2t_{\rm max}$, the linearly extrapolated overdensity at $t_{\rm col}$ is

$$\delta_L(t_{\rm col}) = \frac{a(t_{\rm col}){\rm g}(t_{\rm col})}{a_i {\rm g}_i}\delta_i = \frac{3}{5}{\rm g}(t_{\rm col})(1+\zeta)\Big[\frac{\omega(t_{\rm col})}{\zeta}\Big]^{1/3}, \tag{1.15}$$

where we have used that $\omega_i = \omega(t_{\rm col})[a_0/a(t_{\rm col})]^3$ and that ${\rm g}_i \to 1$ for $a_i \ll a_0$. The

above equation specifies the relation between δ_L and $t_{\rm col}$, and can be approximated by

$$\delta_L(t_{\rm col}) = \frac{3}{5}\Big(\frac{3\pi}{2}\Big)^{2/3}[\omega_m(t_{\rm col})]^{0.0055} \approx 1.686[\Omega_m(t_{\rm col})]^{0.0055}, \tag{1.16}$$

with an accuracy to better than 1%. This relation indicates that regions in which the overdensity exceeds δ_L predicted by the linear theory are deemed to have already collapsed. Note from equation (1.16) that the dependance of this critical value on Ω_m is weak and $\delta_L \simeq 1.68$ should be good approximation to all realistic cosmologies, and the entire period during which structures are formed.

In practice, the sphere will never collapse to a singularity as predicted by equation (1.11) but some kinetic energy of collapse will be converted into random motions via dissipative processes. The infalling material undergoes violent phase mixing, relaxation and finally settles into an equilibrium configuration that fulfills the virial theorem, called *halo*. A particularly useful quantity is the ratio of the halo density to the critical density of the Universe at virialization,

$$\Delta_c(t_{\rm col}) = \frac{\rho_{\rm vir}(t_{\rm col})}{\rho_{\rm crit}(t_{\rm col})}. \tag{1.17}$$

For the spherical collapse in an Einstein-de Sitter Universe ($\Omega_m = 1, \Omega_\Lambda = 0$), $\Delta_c \simeq 175$, assuming that the equilibrium configuration is reached when the sphere collapses to half of the turnaround radius, at about $t = 2t_{\rm max}$ (Binney & Tremaine, 1987). Unlike δ_L, Δ_c is cosmology-sensitive. For a flat Universe with a non-zero cosmological constant, Δ_c still can be approximated by the value derived based on the Einstein-de Sitter Universe over matter-dominated epoch, whereas the disparity becomes significant after the Universe enters the accelerated expansion epoch (Lokas & Hoffman, 2001).

The halos formed through gravitational collapse are not isolated in the Universe but they are expected to undergo continuous accretion of matter from the environment and mergers with other nearby halos to form larger structures, following a bottom-up fashion. This scenario is the result from the combination of the cold dark matter model and a presumed power spectrum for the primordial perturbations — $P(k) \propto k$, or Harrizon-Zeldovich spectrum, the latter being close to the predictions by many inflation models. At present, structures of $10^{15} M_\odot$ are in process of collapsing, and yet structure growth will freeze out at some point when gravity can no longer conquer the expansion rate of the Universe.

Such a Universe, described by equation (1.1), with a presumed primordial density fluctuation and the present-day cosmological parameters given approximately by equation (1.5), and where cold dark matter dominates the matter density field, is called a standard ΛCDM Universe, which constitutes the framework of this thesis.

1.2 Groups and Clusters

When the overdensities of dark matter collapse, the baryons follow, condense and cool down in the halo, and eventually form the galaxies we see today. Being gravitationally "glued" to the underlying dark matter, galaxies trace the hierarchical formation of cosmic structures, in the sense that the present-day galaxies have been formed via successive merger of smaller objects in the past; on the large scales, galaxies are trapped and virialized in halos collapsed from long-wavelength perturbations in cosmic matter.

Galaxy clusters are the largest virialized structures in the present-day Universe, containing hundreds to thousands of gravitationally bound galaxies within a scale of a few Mpc. Their smaller counterparts, galaxy groups, host a few to about a hundred bound galaxies in closer proximity. They are characterized by the hot and diffuse gas component that permeates the entire halo and produces strong X-ray emission, called the intra-group or intra-cluster medium (IGrM/ICM) depending on the system where it is trapped. The temperature of this hot halo gas component should be close to the virial temperature ($T_{\rm vir}$) of the system, given by

$$k_{\rm B}T_{\rm vir} = \frac{GM_{\rm vir}\mu m}{3R_{\rm vir}}, \tag{1.18}$$

where $k_{\rm B}$ is the Boltzmann constant, μ is the mean molecular weight, m is the hydrogen mass, and $R_{\rm vir}$ is the virial radius within which cosmic matter is in virial equilibrium. In massive clusters, ICM is fully collisionally ionized and emits X-ray mainly in the form of thermal bremsstrahlung (free-free emission), whereas in groups, the IGrM is relatively cooler ($k_{\rm B}T_{\rm vir} \lesssim 1$ keV; hereafter $k_{\rm B}$ is omitted when describing temperature in unit of keV) and a sizeable amount of emission is expected to be contributed by line emission owing to the collisional excitation process. A number of physical quantities of the IGrM/ICM can be derived from its X-ray spectrum based on the existing plasma models.

Galaxy groups and clusters are of fundamental interest from the cosmological perspective. For instance, the halo mass function, particularly in the massive cluster regime, is highly sensitive to both the expansion and growth history of the Universe so that it provides powerful constraints to the cosmological parameters such as Ω_m, Ω_Λ and σ_8[1] (e.g. White, Efstathiou & Frenk, 1993; Rosati, Borgani & Norman, 2002; Vikhlinin et al., 2009). The halo mass function in the group regime is also useful tool for testing the cold dark matter paradigm, in which structures on this scale are thought to have developed from the perturbations having persisted in dark matter before the last scattering. Furthermore, the dark matter structures of groups and clusters and their statistical properties provide many interesting tests for the modified gravitational theories (e.g. Schmidt et al., 2009; Hellwing et al., 2013). And it can be seen that the usage of groups and clusters as cosmological probes hinges upon the precise determination of their masses.

At present, there are four major methods for estimating mass of groups and clusters: (1) via measuring the detailed density and temperature distribution of the IGrM/ICM from X-ray observations coupled with assumption of hydrostatic equilibrium (e.g. Fabian et al., 1981; Markevitch et al., 1998; Ettori & Fabian, 1999; De Grandi & Molendi, 2002; Vikhlinin et al., 2006; Rasmussen & Ponman, 2007, 2009; Sun et al., 2009); (2) via weak gravitational lensing (e.g. Leauthaud et al., 2010; Hoekstra et al., 2013); (3) via the Sunyaev-Zeldovich (SZ) effect, which measures the distortion of the observed CMB spectrum due to the inverse Compton scattering by the hot IGrM/ICM (e.g. Zel'dovich, 1970; Zeldovich, 1972; Birkinshaw, 1999; Carlstrom, Holder & Reese, 2002; Nagai, 2006; Vanderlinde et al., 2010; McCarthy et al., 2014); (4) via caustic method, which estimates the escaping velocity of a group/cluster by interpreting the distribution of the member galaxies in redshift space (e.g. Diaferio & Geller, 1997; Diaferio, 1999; Alpaslan et al., 2012). Each of these approaches has advantages as well as drawbacks so that a promising strategy is perhaps to perform mass calibration using a combination of different techniques. To be specific, X-ray observations can simply probe a relatively complete sample of groups and clusters, and its precision has greatly advanced owing to the improved resolution and sensitivity of the new generation instruments, *XMM-Newton* and *Chandra*. However, this method relies on the assumption that the IGrM/ICM is in hydrostatic equilibrium, which can be unreliable when it comes to the unrelaxed systems that have recently

[1] σ_8 is the *rms* overdensity in cosmic matter on the scale of 8 h^{-1} Mpc, which serves as a normalization to the power spectrum of cosmic matter.

gone through merger (Mahdavi et al., 2008; Rasia et al., 2012). Even for the relaxed systems, subsonic bulk motions in ICM/IGrM, magnetic field, and cosmic rays could provide nonthermal pressure support, which renders the hydrostatic masses biased low (Nagai, Vikhlinin & Kravtsov, 2007; Laganá, de Souza & Keller, 2010). Weak gravitational lensing, on the other hand, is independent of the dynamical state of the baryonic matter but directly probes the total mass of clusters, and groups more recently by stacked lensing (Leauthaud et al., 2010). However, this method is limited to moderate redshifts owing to the shape of the lensing weight function (see discussions in Leauthaud et al., 2010). For high-redshift ($z > 1$) detections, SZ effect is the best option given the strength of SZ flux being independent of redshift. And large-scale SZ survey is also complementary to X-ray survey in that the SZ and X-ray flux have different scaling with the gas temperature and density, and therefore it can shed light upon the potential selection biases by X-ray method (see Giodini et al., 2013, for review). Regardless of its advantages, the SZ approach faces the difficulty of removing contamination from galactic dust emission, radio point sources, as well as the CMB. Lastly, the caustic method gains popularity as rapidly growing size of the spectroscopic samples (e.g. Knobel et al., 2009; Robotham et al., 2011), but the mass estimation by this method is restricted to $R_{\rm vir}$, beyond which galaxies are no longer virialized. In addition, the removal of interloping galaxies becomes a challenge for the low mass groups of which there are only a few members.

Apart from their cosmological usages, groups and clusters are also ideal laboratories for studying a number of astrophysical processes, and especially for those associated with galaxy formation and evolution. Over the years, accumulating multi-wavelength observations and increasingly detailed theoretical studies have revealed that the properties of the galaxies are strongly impacted by the environments they live in, and a variety of mechanisms in groups and clusters should be responsible for altering the properties of galaxies therein. For instance, the expected higher chance of mergers and close encounters in denser environments is consistent with the observed trend of higher ratio of early to late type galaxies in groups and clusters than in the field (e.g. Dressler, 1980; Postman & Geller, 1984; Barnes, 1988; Moore et al., 1996). Besides, dynamical friction forces cause the massive infalling galaxies to slow and sink down to the centre at sufficiently rapid rate so as to account for the presence of a massive centrally-located 'cD' galaxy in many groups and clusters (e.g. Chandrasekhar, 1942; Ostriker & Tremaine, 1975; Ostriker & Hausman, 1977; Nipoti et al., 2004; Just et al., 2011). And furthermore, ram-pressure stripping and strangulation

process are thought to be responsible for quenching star formation in the infalling satellite galaxies and therefore make them more passive than the field galaxies (e.g. Gunn & Gott, 1972; Larson, Tinsley & Caldwell, 1980; Abadi, Moore & Bower, 1999; Balogh & Morris, 2000; van den Bosch et al., 2008; Bösch et al., 2013; Haines et al., 2013; Taranu et al., 2014; Haines et al., 2015).

Conversely, a substantial amount of observational evidence has revealed that the very processes underlying the formation and evolution of galaxies — star formation, stellar nucleosynthesis, feedback and galactic outflows, etc. — also have profound impact on the wider environment. The properties of the IGrM/ICM, for example, cannot be fully understood without reference to these galactic processes and therefore they have been extensively studied and widely used as tools to constrain these processes over the years. One of the most challenging problems related to IGrM/ICM is the so-called "cooling crisis". It has been found that a substantial fraction of the groups and clusters are observed to have core cooling time far shorter than the system age (Fabian, Nulsen & Canizares, 1984; Edge, Stewart & Fabian, 1992; O'Sullivan et al., 2014). Were there no energy sources that inhibit radiative cooling, the gas deposition rate (*i.e.,*the mass of gas that cools out of the hot, X-ray emitting phase and sinks to the core per unit time) could reach hundreds to thousands of solar masses per year (Fabian, 1994). Evidence for cooling flow is indeed observed, albeit indirectly, that couples clusters exhibiting shorter cooling time or lower central gas entropy with indicators of enhanced star formation in the central galaxies (Egami et al., 2006; Cavagnolo et al., 2008; Bildfell et al., 2008; Pipino et al., 2009). Nevertheless, the inferred mass deposition rate from those systems is still one to two orders of magnitude lower than the predicted value assuming pure cooling. Increasing number of studies have pointed out that the energetic feedback from the radio active galactic nuclei (AGNs) at the group/cluster centres be the principle mechanism responsible for quenching the cooling flows. One competitive advantage of this model is that it is relatively straightforward to device a self-regulated feedback loop — gas cools down from the environment and feeds the supermassive black hole (SMBH) that is embedded in central galaxies, radio AGN is triggered, which heats the surrounding gas and reduces the cooling rate, AGN becomes quiescent and the entire process repeats — balancing heating and cooling in the central IGrM/ICM over the long term, and thereby retain the cool cores in quasi-thermal equilibrium as suggested by a wealth of observational evidence (e.g. McDonald et al., 2013). Bîrzan et al. (2004) estimated that the observed AGN-inflated "bubbles" (the cavities embedded in the IGrM/ICM that have

lower X-ray surface brightness than the surrounding) in groups/clusters can introduce $10^{58} - 10^{61}$ erg into the IGrM/ICM. This energy is sufficient to counterbalance the radiative cooling in those systems provided that the radio AGN is triggered every $\sim 10^8$ years (Simionescu, 2009). A wealth of effort has recently been devoted to studying the detail of how the energy/momentum injected from AGN is dispersed into the IGrM/ICM (e.g. Pope, 2010; Kunz, 2011; Fujita & Ohira, 2012; Kunz et al., 2012; Fujita & Ohira, 2013; Babul, Sharma & Reynolds, 2013; Arth et al., 2014; Komarov et al., 2014).

However, McCarthy et al. (2008) has argued that although feedback from central radio AGNs could be able to maintain the present-day configuration of the cool cores, it might be insufficient to transform such systems into the observed wide range of non-cool core systems as the required energy far outweighs that produced by the largest AGN outburst that has ever been observed. This fact strongly suggests that the non-cool core systems were "pre-heated", *i.e.,*heated before the collapse of the halo (Kaiser, 1991; Evrard & Henry, 1991; Balogh, Babul & Patton, 1999; Tozzi & Norman, 2001; Babul et al., 2002; McCarthy et al., 2004), as the required pre-heating energy for reaching their observed present-day configuration can thereby be significantly reduced. However, the source of pre-heating and how it is coupled with the formation of galaxies/back holes are still unclear.

The scaling relations between various global properties (e.g. X-ray luminosity and temperature, virial mass and temperature, etc) of groups and clusters are useful tool for constraining the details of non-gravitational heating. Observations show that these scaling relations have different slopes and/or normalizations with the results predicted by the non-radiative models allowing for gravity-driven processes only (e.g. gravitational shock heating and compression) (Kaiser, 1991; Helsdon & Ponman, 2000; Osmond & Ponman, 2004; Sun et al., 2009; Pratt et al., 2010; Maughan et al., 2012). While radiative cooling can reconcile this discrepancy to some degree, it alone cannot be the solution because otherwise too many stars are formed (the "cooling crisis"). In recent years, different authors used large-scale hydrodynamic simulations with implementation of energetic feedback (e.g AGN, galactic outflows) and produced scaling relations in reasonable agreement with observations (e.g. Puchwein, Sijacki & Springel, 2008; Fabjan et al., 2010; McCarthy et al., 2010; Planelles et al., 2014). Yet they almost all have difficulty in simultaneously accounting for all the observed properties of the galaxies in groups and clusters.

Apart from its thermal state, the metal[2] content of the IGrM/ICM is another feature that has garnered much attention over the years. The abundances of different elements in the IGrM/ICM can be determined by measuring the equivalent width of their characteristic emission lines via X-ray spectroscopy. Observations show that the metallicity of the IGrM/ICM can reach one-third to one-half solar value (Edge & Stewart, 1991; Peterson et al., 2003; De Grandi et al., 2004; de Plaa et al., 2007). This relatively high enrichment level of the hot halo gas is not only an archival record of the cumulative star formation history in the groups and clusters but also indicates a significant mass transfer between the galaxies and the hot halo gas. And the enrichment of the IGrM/ICM provides important constraint to the physical mechanisms responsible for this gas transfer.

The deposition of metals in the IGrM/ICM can occur via a number of processes: metal-enriched winds from the galaxies, ram-pressure stripping of the enriched interstellar medium (ISM) in the galaxies and mixing of this into the IGrM/ICM (Domainko et al., 2006), tidal stripping of the stars from the galaxies (Toomre & Toomre, 1972), followed by direct enrichment of the IGrM/ICM by the resulting unbound stellar population (Sivanandam et al., 2009), etc. Each of these processes individually results in different amounts of iron and α-elements in the IGrM/ICM. In order to investigate the role of each of these processes, Davé, Oppenheimer & Sivanandam (2008, hereafter DOS08) carried out the first systematic study of the halo gas-galaxy mass transfer and their major finding was that the simulations without large-scale galactic outflows would result in much lower α (oxygen)-to-iron abundance ratios in the hot halo gas than are observed, indicating that these outflows played a crucial role in its enrichment. Also observations show that outflows are ubiquitous in star-forming galaxies from the local up to $z \sim 3$ (see Martin, 2005, 2006; Sturm et al., 2011; O'Sullivan et al., 2012; Bradshaw et al., 2013; Veilleux et al., 2013; Williams et al., 2014; Turner et al., 2014; Villar Martín et al., 2014; Sell et al., 2014, and references therein).

Large-scale galactic outflows may be AGN-powered or stellar-powered. AGN-powered outflows (both jets and winds) are unlikely to flush the metals out of the galaxies efficiently in that the metal production, by virtue of being a byproduct of star formation, occurs in a distributed fashion across the entire galaxy, whereas the bulk of

[2]In astronomy and astrophysics, all elements heavier than helium are referred to as "metals". Most metals in the Universe are produced in stars, predominantly through thermonuclear burning, or in the processes generated by the extreme conditions in SNe.

the star-forming, metal-enriched ISM is expected to be unaffected by AGN-powered outflows. In particular, relativistic jets emanating from the AGN are observed to have narrow cone angles and large inclinations from the disk plane (O'Sullivan et al., 2012). Observations also show that luminous AGN ($L_{\rm AGN} \gtrsim 0.01 L_{\rm Edd}$) can drive wide-angle ultra-fast ($\sim 0.1c$) outflows which we will refer to as "AGN winds" (Pounds et al., 2003a,b; Tombesi et al., 2010a,b), and while they almost certainly impact the regions close to the AGN ($R \sim 1$ kpc), the more extended dense molecular disk where the bulk of the metals are deposited will remain unaffected because the relatively thin galaxy disk subtends only a small fraction of the solid angle spanned by the outflows and moreover, the AGN outflows preferentially escape through the paths of least resistance normal to the disk (*c.f.* Faucher-Giguère & Quataert, 2012; Gabor & Bournaud, 2014). On the contrary, stellar-powered outflows, namely outflows driven by stellar wind, UV photons from young stars and SN explosions, are expected to efficiently flush the metal-enriched ISM out of the galaxies and into the IGrM by virtue of its distributed launch centres over the entire galactic disk (Murray, Quataert & Thompson, 2005; Murray, Ménard & Thompson, 2011; Krumholz & Thompson, 2013; Thompson et al., 2015). To sum up, while feedback from AGN — through its powerful jets and outflows — have profound impact upon the thermal state of the IGrM/ICM, the stellar-powered outflows are expected to play a more important role in its chemical enrichment.

So far we have discussed much about the properties of groups and clusters and their use as cosmological and astrophysical probes without explicitly pointing out the reason for distinguishing them by two different names. Groups indeed can simply be regarded as the scaled-down version of clusters to first order as they do share many general features in common. Yet closer inspection has revealed some detailed physical distinction between these two hierarchies. Specifically, groups have relatively shallower potential wells, and therefore the IGrM is expected to be more susceptible to the energetic feedback from galaxies. This is supported by some observational evidence such as the increased steepness of the X-ray luminosity−temperature scaling relation at $T \lesssim 1$ keV (Edge & Stewart, 1991; Markevitch, 1998; Helsdon & Ponman, 2000; Osmond & Ponman, 2004) and stronger gas evacuation in the central regions of groups than clusters (Giodini, Pierini & Finoguenov, 2009; Sun et al., 2009). For the same reason, galactic processes such as mergers, harassment and ram-pressure stripping have different efficiency in group and cluster environment, which results in the difference of morphology and colour distribution of their member galaxies

(Helsdon & Ponman, 2003; Hoyle et al., 2012). Moreover, observations also reveal a decline of the overall metal abundances of the central hot gas as it goes from the cluster to the group regime (Sun, 2012, and references therein), indicating that either metal deposition is less efficient or the ability of retaining metals in the hot halo gas is weaker in groups than in clusters. Therefore, study on groups provides a wealth of benefits for a more comprehensive understanding of galaxy formation and evolution, galaxy-environment interplay and also the observed properties of clusters, knowing that they have been formed by successive merger of groups in the past.

The objective of this thesis is to study the impact of the stellar-powered outflows on the thermal and chemical properties of the groups by using cosmological hydrodynamic simulations. The following section will present the detail of the wind model in this simulation and its achieved success, the expectation of this work from using this model and also the thesis layout.

1.3 This Work

1.3.1 The Stellar-powered Outflow

Stars deposit copious amounts of energy and momentum into the ISM during their life and in death — a process referred to as stellar feedback. It is well known that stellar feedback plays a vital role in regulating star formation within galaxies, as early models with no such sort of feedback within ΛCDM framework have ended up with too many stars than are observed in the Universe. Stellar feedback could take various forms, such as energy and momentum injection from supernova explosions, stellar winds, photoheating and radiation pressure (see Hopkins, Quataert & Murray, 2012, for an overview). Yet the detail of how these mechanisms interplay with the ISM is still poorly understood and has been a key topic in the area of galaxy formation and evolution.

The star formation within galaxies is observed to be inefficient, in both an "instantaneous" and an "integral" sense, as summarized by Hopkins et al. (2014). Instantaneously, the observed Kennicutt-Schmit (KS) relation (Kennicutt, 1998) implies that the efficiency of converting gas into stars within most giant molecular clouds (GMCs) could be as low as a few percent per free fall time (e.g. Evans et al., 2009; Federrath & Klessen, 2013), which is now generally thought to be due to the turbulence produced by stars and SNe (e.g. Krumholz, Dekel & McKee, 2012, and references therein). This efficiency (inefficiency), being observed to be nearly universal, is simply folded into the normalization of the "sub-grid" star formation recipe in most cosmological simulations with poor spatial resolution (e.g. Springel & Hernquist, 2003; Teyssier, Chapon & Bournaud, 2010). But this inefficiency alone is not sufficient as still too much gas cools and fuels star formation, resulting in too massive galaxies in the simulations (e.g. Lewis et al., 2000; Kereš et al., 2009). Therefore, another "integral" inefficiency is required, such that either cold gas be effectively removed from galaxies or gas be prevented from feeding galaxies at the very beginning. Given the observed metal content in the intergalactic medium (IGM) and IGrM/ICM, powerful outflows driven from galaxies with significant mass loss rate are generally required to transport metals into those environments (Oppenheimer & Davé, 2006, DOS08). Recent high resolution simulations that explicitly account for the full set of stellar feedback processes (Hopkins, Quataert & Murray, 2012; Hopkins et al., 2014) confirm that they are more than capable of launching powerful galaxy-wide winds. Also, a growing

body of observational evidence is not only confirming that this is indeed happening (see, for example, Bradshaw et al., 2013; Sell et al., 2014; Geach et al., 2014), but also find, in agreement with theoretical expectations, that such winds are metal-enriched, can reach velocities > 1000 km/s, and imply a mass outflow rate that is comparable to the star formation rate.

In cosmological simulations, however, the integral efficiency (inefficiency) has been more challenging to model in comparison with the instantaneous efficiency (inefficiency). Early work attempted to model such feedback via simply thermalizing surrounding gas by an amount of energy expected to be returned from newly created stars. But it was soon discovered that the added thermal energy was radiated away so rapidly in the dense star forming regions that the desired outflows were rarely driven from galaxies (e.g. Katz, Weinberg & Hernquist, 1996; Lewis et al., 2000; Davé et al., 2001). This is primarily because the multi-phased structures in the ISM are smoothed out into a single average density and temperature on scale of the resolution limits, resulting in spuriously high cooling rate (Bournaud et al., 2010; Hummels & Bryan, 2012). To overcome this problem, often some ad hoc "tricks" are included, such as turning off radiative cooling (along with star formation and other hydrodynamic processes) for an extended period of time (e.g. Governato et al., 2007; Brook et al., 2011; Piontek & Steinmetz, 2011; Stinson et al., 2013), super-heating the surrounding gas in a stochastic manner (e.g. Dalla Vecchia & Schaye, 2012; Schaye et al., 2015; Crain et al., 2015), and simply adding kinetic kicks to the ISM particles "by hand", with their kinetic energy or momentum at injection being coupled to the energy/momentum released by star formation within the galaxies (e.g. Springel & Hernquist, 2003; Oppenheimer & Davé, 2006; Dalla Vecchia & Schaye, 2008; Dubois & Teyssier, 2008; Sales et al., 2010).

Over the years, Davé and collaborators (Oppenheimer & Davé, 2006; Davé, Finlator, & Oppenheimer, 2006; Finlator & Davé, 2008, DOS08) introduced a prescription for stellar-powered galactic outflows in their hierarchical galaxy formation simulations based on the momentum-driven wind model of Murray, Quataert & Thompson (2005, hereafter MQT05) and carried out an extensive study of associated implications. In the momentum-driven wind scenario, radiation from massive stars impinges on the dust, which then collisionally couples to the gas and flushes matter out of the galaxy, resulting in wind velocity and mass loading factor (*i.e.,*the ratio of mass loss rate to the star formation rate) being proportional and inversely proportional to the velocity dispersion of a galaxy, respectively. As shown in these papers, this outflow model

is able to account for a wide range of observations: It successfully reproduces the observed galactic properties, including galaxy mass-metallicity relation at different epochs (Finlator & Davé, 2008; Davé, Finlator & Oppenheimer, 2011a; Hirschmann et al., 2013), present-day stellar mass function below M^* (Oppenheimer et al., 2010), and observations of high-redshift galaxies (Finlator et al., 2006; Davé, Finlator & Oppenheimer, 2006; Finlator, Oppenheimer & Davé, 2011; Davé, Oppenheimer & Finlator, 2011; Anglés-Alcázar et al., 2014). It is, as will be shown in Durier et al. (in preparation), the most effective stellar feedback scheme for inducing widespread enrichment of the intergalactic medium at redshifts as early as $z \sim 5$, as indicated by observations (D'Odorico et al., 2013). And it also results in hot diffuse gas in $z = 0$ groups with iron abundance and the oxygen-to-iron ratio (*i.e.,*$\sim$[Fe/H] and [O/Fe]) that resemble the observations (DOS08). These scalings are in general agreement with direct observations of outflows (Martin, 2005; Rupke, Veilleux & Sanders, 2005) as well as results of recent high-resolution galaxy-scale simulations of Hopkins, Quataert & Murray (2012) which include explicit stellar feedback — radiation pressure, supernova and stellar wind shock heating, photoheating, mass and metal recycling, and etc.

With the adopted outflow scalings in this model, high outflow rates and frequent gas re-accretion are generated and galaxies should be viewed as co-evolving with their environments between which they continuously exchange energy, matter and metals (see OD08). This galaxy-environment ecosystem plays a key role in reproducing the variety of the observed properties as mentioned above. Yet stellar-powered outflow alone does not solve all critical problems regarding the formation and evolution of cosmic structures. For instance, to regulate star formation in massive galaxies and to account for the observed detailed properties of the hot halo gas in the group and cluster core regions may probably require additional feedback mechanisms such as AGN. Yet compared with the no-wind models, the prescription for momentum-driven wind has already gone a fair way towards reducing the long-standing discrepancy between the physical structure of simulated and real systems.

The aim of this thesis is to expand on the cosmological numerical simulation study of DOS08 to characterize in greater detail the properties of galaxy group population at $z = 0$ in the currently favoured ΛCDM hierarchical structure formation model that allows for stellar-powered galactic outflows, with specific focus on the chemical enrichment of the IGrM. The simulation does not include explicit treatment of AGN feedback, yet our aims are (a) to establish a baseline against which we will

compare future models; (b) to identify model successes that are genuinely due to stellar/supernovae-powered outflows; and (c) to pinpoint mismatches that not only signal the need for AGN feedback but also constrain the nature of this feedback. We will show in this thesis that this deficit does not significantly alter our results about how the enrichment of the IGrM unfolds, since (1) metals are flushed out of the galaxies primarily by stellar-powered galactic outflows (noted in Section 1.2) and (2) most of the metals in the IGM and in the IGrM are from lower mass galaxies whose evolution is expected to be only minimally impacted by AGN feedback, if at all. The most massive galaxies, whose evolution would be strongly impacted by AGN feedback and which, in the absence of the latter, build up a much larger stellar mass than their observed counterparts, contribute approximately 25% of the metals in the hot IGrM. A reduced contribution from these galaxies due to quenching of star formation by AGN feedback should in fact improve the agreement between our simulation results and observational data even further.

1.3.2 Thesis layout

In **Chapter 2**, we provide a brief description of our simulation setup and also discuss how we construct our catalog of galaxy groups.

In **Chapter 3**, we examine the distribution of formation epochs of the $z = 0$ groups, the distribution of the epochs at which the hot IGrM in the $z = 0$ groups is established, the distribution of epochs when this IGrM is enriched with oxygen, silicon and iron, etc. Our simulations do not include the effects of AGN feedback. We discuss how this affects our group properties. We also show that our findings concerning the bulk metallicity of the IGrM and the extent of mass recycling between the IGrM and the galaxies is unlikely to change with the addition of AGN feedback as long as the associated implementation faithfully describes AGN outflows as they are observed to behave.

In **Chapter 4**, we examine in greater detail the spatial distribution of the metals in the IGrM as well as the origin of the metals at different radii in the groups - that is, identifying (a) when the iron and α-elements at different radii are injected into the IGrM, (b) which galaxies are responsible for the enrichment, (c) how this transfer is effected, and (d) where are these metals ejected and how this injection radius compares to where they end up at z = 0. By scrutinizing these problems, we expect to establish better understanding of how enrichment of the IGrM proceeds.

In **Chapter 5**, we present the summary and conclusion of this work, as well as an outline of future work.

We thank Prof. Romeel Davé for providing us with the simulation codes and data without which this thesis could not have been completed.

Chapter 2

SIMULATING GALAXY GROUPS

2.1 Simulation Details

We extracted galaxy groups from a cosmological hydrodynamic simulation of a representative comoving volume $(100\ h^{-1}\ \mathrm{Mpc})^3$ of a ΛCDM universe with present-day parameters: $\Omega_{\mathrm{m},0} = 0.25$, $\Omega_{\Lambda,0} = 0.75$, $\Omega_{\mathrm{b},0} = 0.044$, $H_0 = 70$ km s^{-1}Mpc^{-1}, $\sigma_8 = 0.83$ and n = 0.95. These are based on the WMAP-7 best-fit cosmological parameters (Just et al., 2011) and are in good agreement with the WMAP-9 results (Hoekstra et al., 2013).

We initialized the simulation volume with 576^3 dark matter particles and 576^3 gas particles, implying particle masses of 4.2×10^8 $\mathrm{M}_\odot$ and 9.0×10^7 $\mathrm{M}_\odot$ for the dark matter and gas, respectively. In the simulation we assumed a spline gravitational softening length of $5\ h^{-1}$ kpc comoving ($3.5\ h^{-1}$ equivalent Plummer softening).

The initial conditions for the simulation volume were generated using an Eisenstein & Hu (1999) power spectrum in the linear regime, and the simulation was evolved from $z = 129$ to $z = 0$ using a modified version of GADGET-2 (Springel, 2005), a cosmological tree-particle mesh-smoothed particle hydrodynamics code that includes radiative cooling using primordial abundances as described in Katz, Weinberg, & Hernquist (1996) and metal-line cooling as described in Oppenheimer & Davé (2006, hereafter OD06). Star formation is modelled using a multiphase prescription of Springel & Hernquist (2003). In this prescription, only gas particles whose density exceeds a preset threshold of $n_{\mathrm{H}} = 0.13$ cm^{-3} are eligible to form stars. The

star formation rate follows a Schmidt law (Schmidt 1959) with the star formation time-scale scaled to match the $z = 0$ Kennicutt law (Kennicutt 1998). We assume that the mass function of forming stars is given by the Chabrier initial mass function (IMF) (Chabrier, 2003). According to this IMF, 19.8% of the stellar mass goes into massive (*i.e.*, $\geq 10\ M_{\odot}$) stars that engender Type II supernovae (Oppenheimer & Davé, 2008).

Over the course of the simulation, we account for mass loss and metal enrichment from Type Ia and Type II SNe as well as the asymptotic giant branch (AGB) stars. For a detailed discussion of how this was carried out, we refer readers to Oppenheimer & Davé (2008, hereafter OD08). An overview is as follows: In the case of Type II SNe, we use the instantaneous recycling approximation where the mass and the metals are returned immediately to the ISM. Type II SN metal enrichment uses the metallicity-dependent yields calculated from the Limongi & Chieffi (2005) supernova models. In the case of Type Ia SNe, we allow for both a prompt component as well as a delayed component using the model of Scannapieco & Bildsten (2005) in which, the former is tied to the star formation rate as in the case of Type II SNe, and the latter to the stellar mass. The mass loss and the enrichment by the prompt component is returned to the ISM instantaneously while that due to the delayed component commences after a delay of 0.7 Gyrs. As for the AGB stars, the corresponding mass and metal injection into the ISM commences after a delay of 30 Myrs following a star formation event and extends over the subsequent ~ 14 Gyrs. As discussed by OD08, the most significant impact of the AGB stars is to replenish the ISM. In general, a little more that 50% of the stellar mass in a Chabrier IMF is returned to the ISM over ~ 10 Gyrs and 30% of this comes from the AGB stars. The mass transfer from AGB stars also returns to the ISM the metals that were previously locked into these stars. Primarily, the metallicity of this gas is the same as that of ISM from which they were spawned. In detail, however, nucleosynthesis reactions during the AGB phase lead to a slight depletion of the oxygen abundance as well as an enhancement of the carbon abundance. To conclude this brief overview, we note that we explicitly track the evolution in the abundances of four metal species — carbon, oxygen, silicon, and iron. These four species are not only among the most abundant metals in the universe, they are also the species most often observed in quasar absorption line spectra probing the intergalactic medium, in the X-ray spectra of the hot intracluster and intragroup halo gas, as well as the spectra of the circumgalactic and the interstellar gas in galaxies. In the present study, we will focus primarily on the oxygen, silicon and iron.

Our numerical implementation of the kinetic winds powered by stellar feedback is based on the scheme initially developed by Springel & Hernquist (2003), modified to conform to the momentum-driven wind model scalings of MQT05. MQT05 describe a model where the energy and momentum injected into the ISM by the stars via stellar winds and supernova explosions, and by radiation pressure produced by the continuum absorption and scattering of photons on the dust grains that are collisionally coupled to the gas, propel galaxy-wide winds. A detailed discussion of the model and the particular implementation that we are using has been discussed extensively in a series of papers starting with OD06, with updates described in OD08 and Oppenheimer & Davé (2009), and has recently been shown to be in general agreement with the results of recent high-resolution galaxy-scale simulations of Hopkins, Quataert & Murray (2012); Hopkins et al. (2014); Muratov et al. (2015) that include explicit stellar feedback. For completeness, we briefly summarize below the current implementation:

The mass outflow rate scales with the star formation rate as

$$\dot{M}_{\rm wind} = \eta\, \dot{M}_{\rm star} \text{ where } \eta = (150 \text{ km/s})/\sigma_{\rm gal}$$

is the mass loading factor. Here, $\sigma_{\rm gal}$ is the galaxy velocity dispersion. It is used as a measure of the depth of the galaxy's potential and is computed using the total mass (baryons+dark matter) of the galaxies identified over the course of the simulation (*c.f.,* Oppenheimer et al., 2010). This means that when a gas particles density exceeds the threshold for star formation, it is eligible to form stars with some probability $P_{\rm star}$ but at the same time, its probability for being incorporated into a wind is $P_{\rm wind} = \eta\, P_{\rm star}$. If a particles is chosen to be in an outflow, it is given a velocity kick $v_{\rm wind}$, where

$$v_{\rm wind} = 4.3\sigma_{\rm gal}\sqrt{f_L - 1} + \beta\sigma_{\rm gal}, \tag{2.1}$$

is orientated parallel to $\pm\mathbf{v}\times\mathbf{a}$, the cross product of the velocity and the acceleration vectors of the particle prior to entrainment.

In the above equation, the first term on the right represents the wind launch velocity — with f_L, the luminosity factor in units of the galactic Eddington luminosity (*i.e.,* the critical luminosity for expelling gas from the galaxy via radiation pressure) given by equation (5) of OD08. As discussed in OD08, this wind launch velocity is

capped by limiting the value of $\sigma_{\rm gal}$ to

$$\sigma_{\rm gal,max} = 1400 \left(\frac{50{\rm Myrs}}{\tau_{\rm SF}} \right) \ {\rm km/s}, \tag{2.2}$$

where $\tau_{\rm SF}$ is the local star formation timescale, to account for the fact that in the MTQ05 model, starburst luminosities need to reach the Eddington limit to expel the gas. In practice, we find that this cap has no impact on winds from galaxies at $z > 1$ while at lower redshifts, the median wind velocity from the group central galaxies is reduced by a constant factor that grows to 20% by $z = 0$.

The second term (with $\beta = 2.9$) represents an additional velocity kick at launch, to simulate the continued dynamical pumping of the gas in the MQT05 momentum-driven wind model (see OD06 and OD08 for details). Since our simulations neither resolve the detailed structure of the ISM nor the detailed hydrodynamics of the wind flowing through the ISM, this model assigns the ejected gas particles an appropriate initial velocity to ensure that the wind has roughly the expected velocity at large radii. For the same reasons, we also decouple the wind particles hydrodynamically (but not dynamically) from their surroundings until the local gas density drops to 10% of the star formation density threshold or for a time duration equal to 200 $(v_{\rm wind}/100$ [km/s]$)^{-1}$ Myrs. In real galaxies, this outflow would be expected to flow through the ISM and out of the disk along paths of least resistance — *i.e.,* along channels formed by overlapping supernova explosions.

We reiterate that our present simulation does not include the effects of the energy and momentum output of AGNs. As we will show in

2.2 Finding Galaxies and Galaxy Groups in the Simulation Volume

Each simulation output is analyzed to identify both galaxies as well as bound halos. We identify bound halos using the spherical overdensity (SO) procedure described in Kereš et al. (2005): First, associations of dark matter particles are found using a Friends-Of-Friends (FOF) percolation algorithm. Second, after finding the local potential minima of each association, a sphere is constructed around these particles and its radius is expanded until the mean enclosed total mass density equals the virial density for the assumed cosmology at the redshift under consideration:

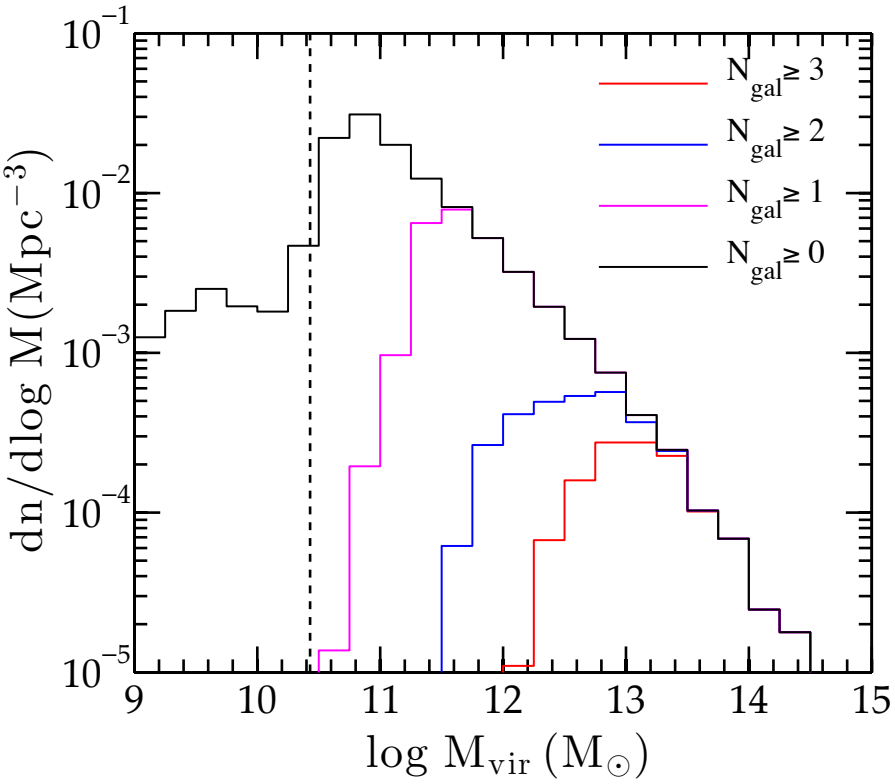

Figure 2.1: The mass function of halos with at least three (red), two (blue), one (magenta) luminous galaxies, as well as of the complete halo population in the simulation volume (black) described in Section 2.2. The dashed vertical line shows our halo mass resolution limit of $2.7 \times 10^{10} M_\odot$, corresponding to 64 dark matter particles.

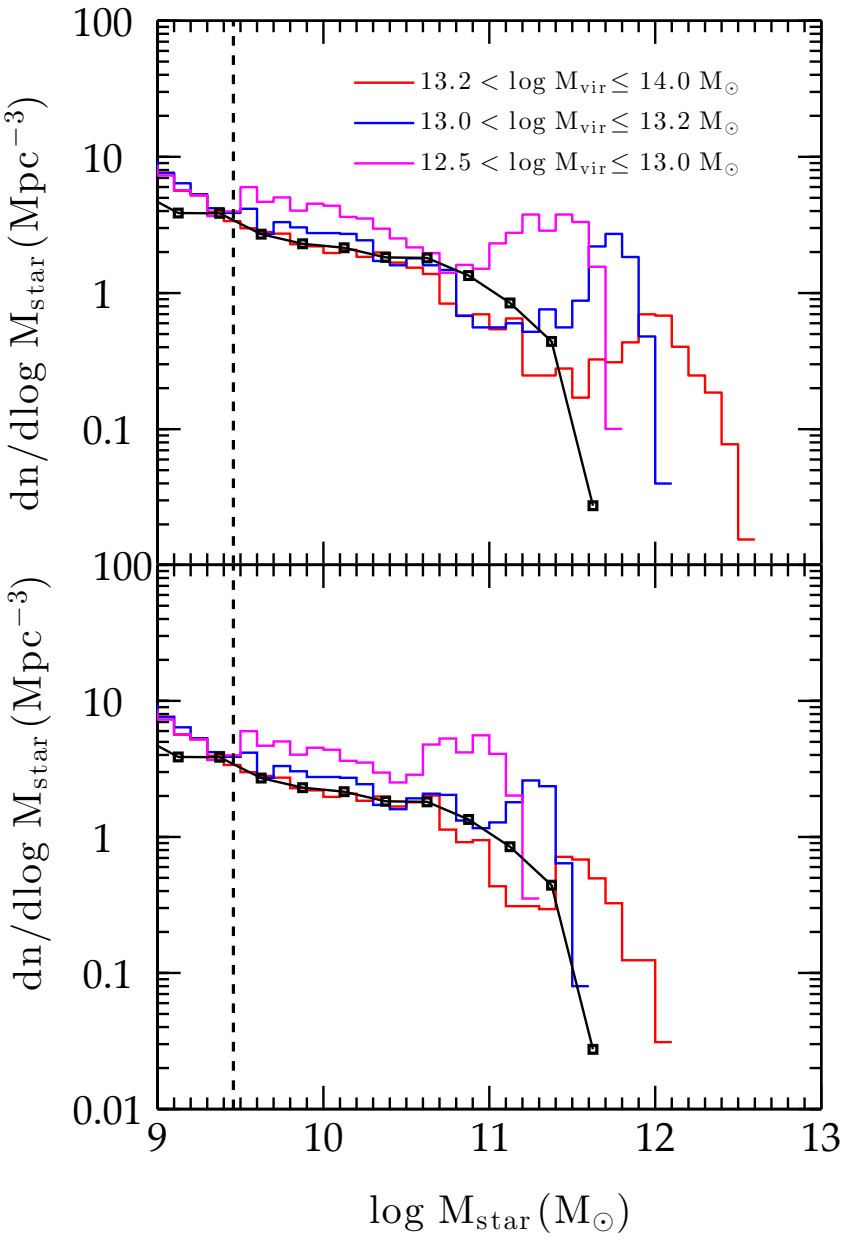

Figure 2.2: The top panel shows the $z = 0$ galaxy stellar mass function (GSMF) of all luminous galaxies in the simulated groups, sorted into three mass bins: $12.5 < \log M_{\rm vir} \leq 13.0$ $M_\odot$ (magenta), $13.0 < \log M_{\rm vir} \leq 13.2$ $M_\odot$ (blue), and $13.2 < \log M_{\rm vir} \leq 14.0$ $M_\odot$ (red). For comparative purposes, we also plot as connected black squares the GSMF for X-ray detected low mass groups spanning the mass range similar to that of our simulated groups (Giodini et al., 2012). The vertical dashed black line shows our luminous galaxy stellar mass resolution limit (see text). In anticipation of the discussion in §3.2.1, the lower panel shows the same GSMFs as in the top except that the stellar mass of galaxies in the simulation with $M_* > 10^{11} M_\odot$ has been *artificially* reduced by a factor of 3.

$$\overline{\rho_{\rm m,vir}}(z) = \Delta_{\rm vir}(z) \cdot E^2(z)\rho_{\rm crit}(0), \tag{2.3}$$

where $E(z) \equiv H(z)/H_0$ is the dimensionless Hubble parameter given by

$$E^2(z) = 1 - \Omega_{\rm m,0} + (1+z)^3\Omega_{\rm m,0},$$

and the virial overdensity factor is well-described by the following fitting function (*c.f.*, Babul et al., 2002):

$$\Delta_{\rm vir}(z) = 49 + 96\Omega_{\rm m}(z) + \frac{200\Omega_{\rm m}(z)}{1+5\Omega_{\rm m}(z)},$$

$$\Omega_{\rm m}(z) = \frac{\Omega_{\rm m,0}(1+z)^3}{1-\Omega_{\rm m,0}+\Omega_{\rm m,0}(1+z)^3}.$$

We will refer to the radius of this sphere as the virial radius, $R_{\rm vir}$, and the mass enclosed as the virial mass of the halo, $M_{\rm vir}$. Occasionally, we will reference M_Δ instead of $M_{\rm vir}$. M_Δ is the enclosed mass inside a sphere centered on the halo center within which the mean mass density is $\Delta \cdot \rho_{\rm crit}(z) = \Delta \cdot E^2(z)\rho_{\rm crit}(0)$. Commonly used values of Δ are 200, 500 and 2500. The mapping between these different quantities is redshift-dependent. At $z = 0$,

$$M_{\rm vir} \approx 1.2M_{200} \text{ and } M_{500} \approx 0.7M_{200},$$
$$R_{\rm vir} \approx 1.36R_{200},\ R_{500} \approx 0.67R_{200},\ \text{and } R_{2500} \approx 0.27R_{200}.$$

In Figure 2.1, we show the $z = 0$ mass functions of all halos in the simulation volume (black curve), as well as halos with at least three (red), two (blue) and one (magenta) "luminous" galaxies (defined below). We identify groups (and clusters) of galaxies as halos containing ≥ 3 "luminous" galaxies. On mass scales $\geq 10^{13}$ $\rm M_\odot$, nearly all halos have at least 3 galaxies while in the mass range 10^{12} $\rm M_\odot \lesssim M_{vir} \lesssim 10^{13}$ $\rm M_\odot$, only a fraction of the halos do. There are a total of 902 groups in our simulation volume at $z = 0$.

Galaxies in the simulation volume are identified using the group-finding algorithm Spline Kernel Interpolative Denmax (SKID)[1] to locate gravitationally bound clumps of star particles and cold ($T < 3 \times 10^4$ K) gas particles that are eligible to form stars (*c.f.*, Oppenheimer et al., 2010). We identify a galaxy as "resolved" if the total mass in cold gas and stars is $\geq 2.9 \times 10^9$ $\rm M_\odot$ and "luminous" if its stellar mass is $\geq 2.9 \times 10^9$

[1] http://www-hpcc.astro.washington.edu/tools/skid.html

$M_\odot$, which is equivalent to ≥ 64 star particles.

The top panel of Figure 2.2 shows the average stellar mass function of the luminous galaxies in the simulated groups at $z = 0$. We divide the groups into three mass bins: $12.5 < \log M_{\rm vir} \leq 13.0$ (magenta), $13.0 < \log M_{\rm vir} \leq 13.2$ (blue), and $13.2 < \log M_{\rm vir} \leq 14.0$ (red), with 393, 145 and 188 groups in each bin, respectively. (The sum of these is short of the total number (902) quoted above because the balance of the groups have $\log M_{\rm vir} \leq 12.5$ or > 14.0.) The size of our mass bins were chosen to ensure that the intermediate and the most massive mass bins match the bins adopted by DOS08 to facilitate comparison with their results.

For comparison, we also show, as connected black squares, the observed galaxy stellar mass function (GSMF) for the X-ray detected low mass groups in the COSMOS survey (Giodini et al., 2012) spanning the similar mass range (10^{13} $M_\odot$ < M_{200} < 2×10^{14} $M_\odot$) to that of our simulated groups (Giodini et al., 2012). It is readily apparent that the simulation shows a clear excess of galaxies with large stellar masses. In the lower two mass bins, there is typically only one 'super-sized' galaxy per group, the central galaxy, whose stellar mass exceeds 10^{11} $M_\odot$ and it is these galaxies that are responsible for the excess. In addition to a 'super-sized' central galaxy, the most massive groups also host one (and sometimes, two) 'super-sized' satellite galaxies within $R_{\rm vir}$. On closer inspection, we have confirmed that (1) these massive satellite galaxies were incorporated into the present-day groups via mergers within the past 6 Gyrs, (2) they were all central galaxies prior to the merger, and (3) these massive satellites are steadily sinking to the center and will eventually merge with the existing dominant central galaxy in the group. It is expected that AGN feedback will quench the growth of these 'super-sized' galaxies. From the resolution limit to approximately $M_* \approx 10^{11} M_\odot$, the GSMF of the group galaxies in our simulation volume agrees very well with the observations. AGN feedback is believed to play a minimal role in these galaxies; their evolution is principally governed by stellar feedback.

2.3 Computing Group Properties

To compare the characteristics of our groups to the observations, we compute various X-ray properties of our group halos. Unless explicitly noted, we focus exclusively on the properties of the hot ($T > 5 \times 10^5$ K), diffuse IGrM particles.

The first of these properties is the rest-frame 0.5-2.0 keV X-ray luminosity within R_{500}: $L_{X,0.5-2.0\,\rm keV}$. This is computed by summing over the luminosity of the individ-

ual IGrM gas particle within a distance $r \leq R_{500}$ of the halo center. The emission characteristics of gas particles is computed using the Astrophysical Plasma Emission Code[2] (APEC) from Smith et al. (2001) assuming that the gas is optically thin and in collisional ionization equilibrium. APEC uses the particles mass, SPH-weighted density, temperature and the metallicity as input, and outputs X-ray spectra, from which the luminosity is computed by summing the intensities over the required range of photon energies (*e.g.* 0.5-2.0 keV). Contributions to line and continuum emission associated with each of the individually tracked elements (iron, oxygen, silicon and carbon, along with hydrogen and helium) are computed separately and summed. The abundances of all the other elements are specified assuming that their abundance ratios relative to iron is solar (Anders & Grevesse, 1989). We note, however, that our results are not sensitive to the latter because in the IGrM temperature and density regime, the line emission is dominated by iron, oxygen and silicon.

To study the metal content of the IGrM, we consider two complementary measures: the mass-weighted and emission-weighted abundances, defined respectively as

$$Z_{\rm q}^{\rm mw} = \frac{\Sigma_{\rm i} Z_{\rm q,i} m_{\rm i}}{\Sigma_{\rm i}^{N} m_{\rm i}} \quad \text{and} \quad Z_{\rm q}^{\rm ew} = \frac{\Sigma_{\rm i} Z_{\rm q,i} L_{\rm i}}{\Sigma_{\rm i}^{N} L_{\rm i}}, \tag{2.4}$$

In these equations, "q" is the metal species under consideration, $Z_{\rm q,i}$ is the SPH kernel-weighted abundance of the i$^{\rm th}$ particle, $m_{\rm i}$ is its mass, and $L_{\rm i}$ is the X-ray luminosity of that particle. The sums run over all IGrM particles within the volume under consideration. Additionally, to facilitate comparison between numerical and observational results, we scale and report all metal abundance estimates in terms of the solar "photosphere abundance" values from Anders & Grevesse (1989): that is, $Z_{\rm O,\odot} = 0.009618$, $Z_{\rm Si,\odot} = 0.0007109$ and $Z_{\rm Fe,\odot} = 0.001875$.

We also compute two different temperature measures of the hot gas in our groups. Observationally, the temperature of the hot gas is determined by fitting its observed X-ray spectrum. Generally, the spectrum within a beam is a composite of the continuum and the line radiation from a range of gas phases with varying temperatures and metallicity. Since the emission from individual components cannot be spectrally distinguished as of yet, and the statistical quality of the observations is insufficient to detect all the features in the spectrum, and since the spectrum itself is only available within a limited range of frequencies, the current convention is to compare the composite spectrum with single-temperature, single-metallicity thermal plasma models,

[2]http://cxc.harvard.edu/atomdb/sources apec.html

and assign the temperature of the best-fit model to the observations. The question for theorists is, and has been for years now: what measure best corresponds to this temperature?

The mean emission-weighted temperature (T_X), which is an average of the temperatures of the individual components weighted by their radiative emission contributions is one possibility and in fact, is the most commonly used measure in theoretical work. We too compute this temperature but we restrict the weighing to X-ray emission within a relatively narrow energy range. In other words, our emission-weighted temperature is defined as the weighted average temperature of the gas particles, where we use the particles' rest-frame 0.5-2.0 keV X-ray luminosity as the weighting factor. As shown in Figure 2.3, T_X is tightly correlated with group mass and we will use the mass ($M_{\rm vir}$, M_{200} or M_{500}) or the mean emission-weighted temperature (T_X) interchangeably when referring to or categorizing the group halos.

Observationally, group and cluster hot gas temperatures are determined by identifying a single-temperature thermal model whose spectrum best matches the observed spectrum. Reproducing this procedure is sufficiently involved, especially if the observed spectrum is an integrated output of gas that spans a range of temperatures, that most theoretical studies have, until relatively recently, tended to rely on T_X as a stand-in. A decade ago, Mazzotta et al. (2004) showed that for clusters of galaxies, T_X is generally biased high by as much as $\sim$25% compared to the observationally determined integrated X-ray temperatures and introduced an alternate weighting scheme leading to a new temperature measure, which we will refer to as the "spectroscopic" temperature ($T_{\rm spec}$), which is intended to be directly comparable to the observationally determined temperature, at least in the case of the hot ($T > 2$ keV) intracluster gas. Vikhlinin et al. (2006) has since extended the approach to cooler groups and here we will use their algorithm. As demonstrated by Vikhlinin et al. (2006), $T_{\rm spec}$ is an accurate estimate (to within a few percent) of the fitted temperature of a multiphase plasma with components whose temperatures and metallicities span the range expected in group and cluster environments.

We compute the two temperatures mentioned above (T_X and $T_{\rm spec}$) using either all the hot diffuse particles within R_{500} or only those within the radial range $0.15R_{500} \leq r \leq R_{500}$. The latter measures will be referred to as "core-corrected" and identified with subscript "corr" (short for 'corrected'). Observational studies of groups typically quote "core-corrected" temperatures.

Comparing $T_{\rm spec}$ to T_X, we find that in the small (≤ 1 keV) groups, the two agree

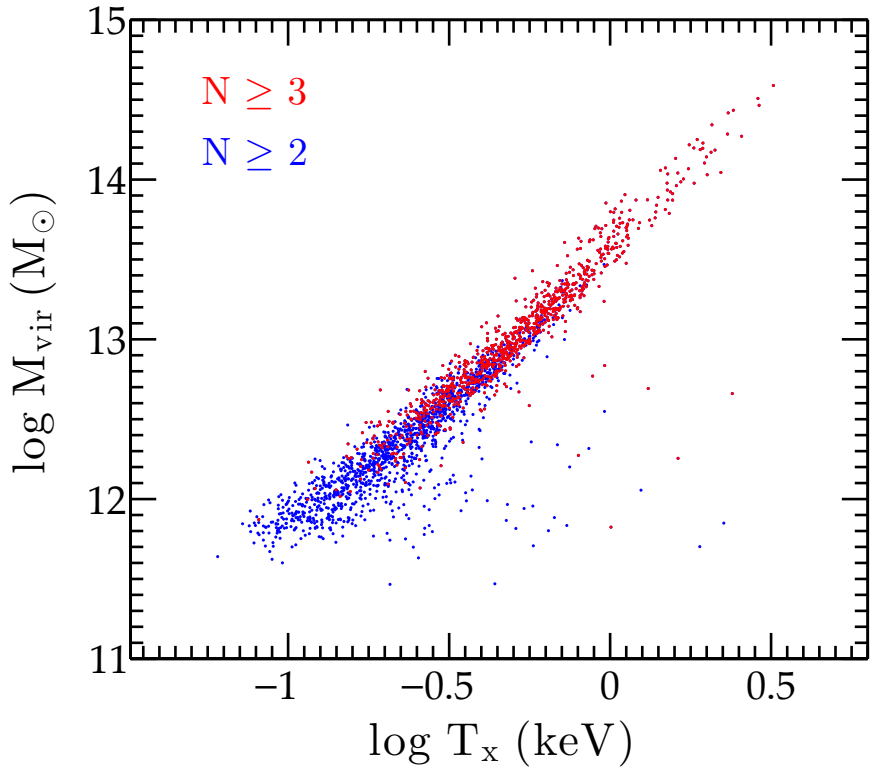

Figure 2.3: $M_{\rm vir} - T_X$ relation of galaxy groups with at least three (red) and two (blue) luminous galaxies. T_X is tightly correlated with $M_{\rm vir}$ and follows the scaling relation: $M_{\rm vir} \propto T_X^{1.7}$. Groups that lie significantly off this relationship are located near larger systems and are "contaminated" by the latters' hot diffuse gas. Excluding groups with fewer than three luminous galaxies, eliminates most of these "contaminated" halos.

with each other to within $\sim$3%, in agreement with results shown in Vikhlinin et al. (2006). However, in hotter systems the divergence is significant enough to be a cause for concern. We discuss this further in the next section. We also note that neither $T_{\rm spec}$ nor T_X is an unbiased measure of the actual mean temperature of the gas, which is much better approximated via a mass-weighted average.

Finally, we point out that to compare the X-ray scaling relations for our simulated groups across different redshifts, we adopt the common convention in the literature and plot quantities motivated by the self-similar model of group and cluster halos (Kaiser, 1986). In this model, the scaling relations are preserved when using the quantities $L_X(z)\,E(z)^{-1}$, $M_\Delta(z)\,E(z)$ and $S_\Delta(z)\,E(z)^{4/3}$, where $E(z) \equiv H(z)/H_0$ is the dimensionless Hubble parameter (*c.f.,* equation 2.3), instead of $L_X(z)$, $M_\Delta(z)$ and $S_\Delta(z)$. The self-similar model assumes that the profiles describing the internal structure of all groups and clusters have the same functional form, with the gas properties created through gravitational collapse alone, so that these properties scale only with the system mass and the critical density at the time of observation. Strictly speaking, the self-similar model is an anachronism in that it does not account for processes like radiative cooling or heating of the gas by stellar (or AGN) winds and jets, or for a variation in the IGrM fraction with halo mass. As a result, the observed scaling with mass deviates from the predictions of this model. Nonetheless, the observed scaling with redshift (for moderate redshift values) agrees surprisingly well with the self-similar predictions, suggesting that over limited periods of time the systems may well be evolving in a self-similar fashion. For further details, we refer the readers to §3.9 of Kunz et al. (2012) and to Ettori (2015).

Chapter 3

THE SIMULATED PROPERTIES OF THE IGRM

This chapter is organized as follows: In Section 3.1, we discuss the global X-ray properties of our galaxy groups, focusing on three most commonly discussed group X-ray scaling relations: the (X-ray) luminosity-temperature, the luminosity-mass, the mass-temperature and the entropy-temperature relations. We explore the evolution of the model scaling relations over the redshift range $0 \leq z \leq 3$ and also compare the $z = 0$ relations to the observational results. We discuss the baryonic content of the simulated groups in Section 3.2, investigating the variation in the total baryon fraction as well as the stellar and the hot diffuse IGrM mass fractions with group mass over the redshift range $0 \leq z \leq 3$. We compare these fractions with observational results from both low redshift groups as well as more recent results from groups at redshifts out to $z \sim 1$, and we provide a detailed analysis of the assembly of groups total mass, IGrM, and stellar mass. We then investigate the enrichment of the IGrM in Section 3.3, looking at the sources of the iron, silicon and oxygen, the abundance ratios, etc. Finally, we summarize and discuss our findings in Section 3.4.

3.1 GLOBAL X-RAY PROPERTIES OF GALAXY GROUPS

In this section, we discuss some of the global properties of galaxy groups, focusing on the observed X-ray scaling relations, of the simulated $z = 0$ groups and compare these to those of simulated groups at earlier epochs ($z = 0.5$ to 3.0), and to available

observations. As we shall show, even in the absence of AGN feedback, the present model does remarkably well in accounting for the observations.

3.1.1 The Mass-Luminosity-Temperature Scaling Relations

In the absence of feedback and cooling flows, the X-ray luminosity on the group scale ought to scale with the mean gas temperature of the IGrM as $L_X \propto T$ (Balogh, Babul & Patton, 1999; Babul et al., 2002). This relationship is *flatter* than the more familiar $L_X \propto T^2$ scaling in situations where bremsstrahlung dominates the X-ray emission because at temperatures less than 1 keV recombination radiation is as important, if not more, than bremsstrahlung. The observed scaling relationship for groups, $L_X \propto T$ [4], however, is much steeper (Helsdon & Ponman, 2000), indicating that either heating (Balogh, Babul & Patton, 1999; Babul et al., 2002) and/or cooling (Voit & Bryan, 2001) has significantly altered the hot X-ray gas distribution. Both processes eliminate the denser, lower entropy, X-ray bright, gas.

Figure 3.1 shows the rest-frame $0.5-2.0$ keV X-ray luminosity emitted within the central R_{500} versus the mean core-corrected spectroscopic temperature (solid lines) for the simulated groups at redshifts $z = 0$ (black), 0.5 (blue), 1 (red), 2 (green) and 3 (cyan). Once cosmic evolution is taken into account, the group $L_X - T_{\rm spec,corr}$ curves at $z \leq 1$ essentially lie on top of each other. At higher redshifts, however, the groups – at a given temperature – are less luminous than predicted by the self-similar evolution model. These trends can be understood in terms of the behaviour of the hot gas fraction in the groups that we will discuss in the next subsection.

Focusing on the mean $L_X - T_{\rm spec,corr}$ relationship for our simulated $z = 0$ groups, we note that this is in good agreement with the observations for $T_{\rm spec,corr} \lesssim 1$ keV. In this low temperature regime, the luminosity scales as $L_X \propto T^{5.5}_{\rm spec,corr}$. The steep nature of this relationship is partly due to the use of spectroscopic temperature. The spectroscopic temperature can differ considerably from the true temperature. To illustrate this, we plot in Figure 3.1 the $L_X - T$ relationship for our $z = 0$ simulated groups using the core-corrected mass-weighted temperature ($T_{\rm mw}$ – black dotted curve). For $T \lesssim 1$ keV, $L_X \propto T^{3.8}_{\rm mw}$. The difference between this relationship and the self-similar expectation ($L_X \propto T$) suggests that the groups have been subjected to some process that has a greater impact on the IGrM in groups with the shallowest

[2] For consistency, we use the same mass-concentration relationship adopted by Laganá, de Souza & Keller (2010).

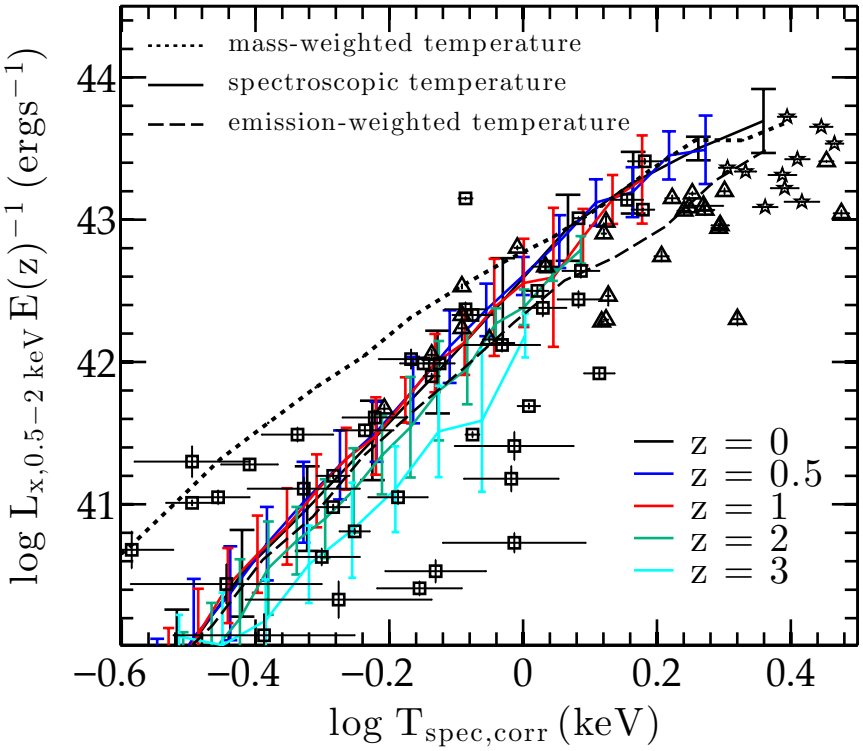

Figure 3.1: X-ray luminosity$-T$ relation for simulated groups at $z = 0$ (black), $z = 0.5$ (blue), and $z = 1$ (red), $z = 2$ (green), and $z = 3$ (cyan). The solid lines show the scaling relationship between the X-ray luminosity that is emitted by gas within R_{500} and the core-corrected spectroscopic temperature. The error bars indicate 1-σ scatter. The dotted and the dashed curves show the mean $L_X - T$ for the $z = 0$ simulated groups, where T is the mass-weighted and emission-weighted temperature (both core-corrected), respectively. Squares, stars and triangles show observed low redshift group data from Osmond & Ponman (2004), Pratt et al. (2009) and Eckmiller, Hudson & Reiprich (2011), respectively. We plot all the groups in Osmond & Ponman (2004) including those with a small radial extent in observable X-rays (i.e. their H sample). Luminosity in the Pratt et al. (2009) and Eckmiller, Hudson & Reiprich (2011) data is corrected to the $0.5 - 2$ keV band.

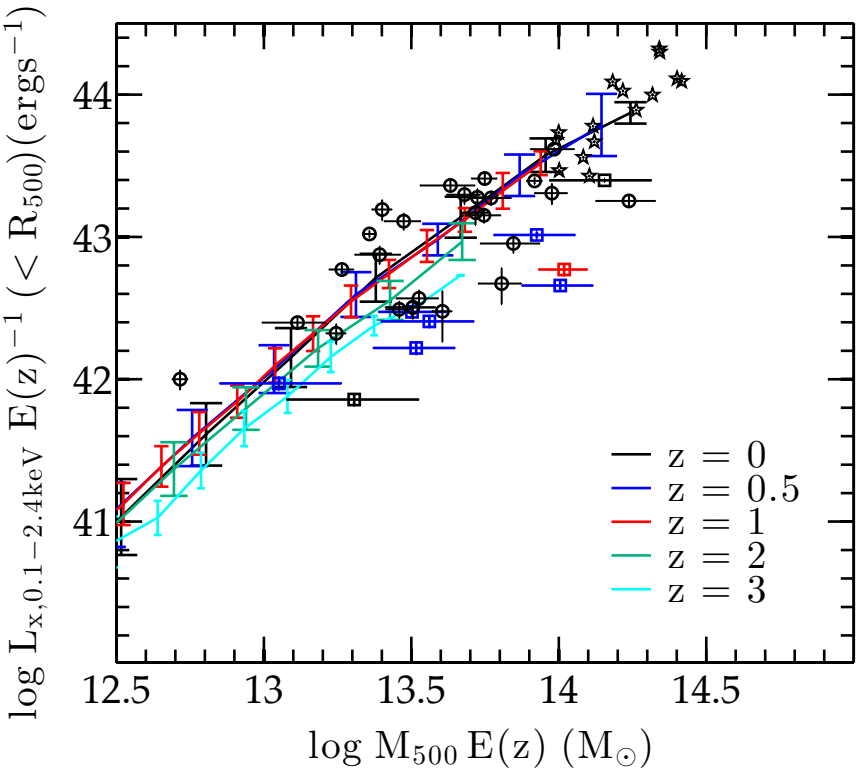

Figure 3.2: $L_X - M$ relation for simulated groups at $z = 0$ (black), $z = 0.5$ (blue), $z = 1$ (red), $z = 2$ (green), and $z = 3$ (cyan). The error bars show 1-σ scatter. The circles, stars and squares show data from Eckmiller, Hudson & Reiprich (2011), Pratt et al. (2009), and Laganá, de Souza & Keller (2010), respectively. The hydrostatic mass estimates from the first two studies have been corrected for the hydrostatic bias (Haines et al., 2015) and $L_{X,\mathrm{bol}}$ from Pratt et al. (2009) have been converted to $L_{X,0.1-2.4\,\mathrm{keV}}$. We also convert the weak-lensing M_{200} values from Laganá, de Souza & Keller (2010) to M_{500} using an NFW profile,[2] and we scale their luminosities using the median value of $L_{X,0.1-2.4\,\mathrm{keV}}(< R_{200})/L_{X,0.1-2.4\,\mathrm{keV}}(< R_{500})$ for our simulated groups. The observed groups at $z \leq 0.25$, $0.25 < z \leq 0.75$, and $z > 0.75$ are plotted as black, blue and red symbols, respectively.

potential wells (low temperatures) and less so on the gas in groups with the deepest potential wells (high temperatures). Both heating (or preheating) of the IGrM by the galactic outflows, which will cause the gas to expand out of (or resist falling into) the shallowest potential wells, as well as the removal of the IGrM by radiative cooling, are plausible mechanisms. At this point, we cannot distinguish between these two.

For $T > 1.2$ keV, the $L_X - T$ based on the spectroscopic and the mass-weighted temperatures converge, implying that in massive groups, the former is a good measure of the latter. Both scaling relations also start to flatten as bremsstrahlung grows in importance. However, we note that compared to the observations, the high mass simulated groups are more luminous, and/or a bit cooler. This suggests that the hot gas in these systems is denser than in real systems. In the scenario where the galactic outflows really do impact the gas density in shallow wells, the emergence of overluminous groups as their halo mass approaches (and exceeds) $M \approx 10^{14}$ $M_\odot$ suggests that the outflows have become ineffectual and another mechanism is necessary.

For illustrative purposes, we also plot $L_X - T$ relationship for the $z = 0$ groups using the mean emission-weighted temperature (T_X – black dashed curve). Until relatively recently, this was the relationship used to compare model $L_X - T$ to observations. For the lowest temperature groups, the emission-weighted and the spectroscopic temperatures are nearly equal, and the two $L_X - T$ curves track each other. For $T > 0.7$ keV, the emission-weighted $L_X - T_X$ deviates from that based on the spectroscopic temperature and remains in good agreement with the observations. This agreement, however, is spurious since the observations are based on the spectroscopic temperature, and indicates a need for caution: The comparison between the T_X-based relation for simulated groups and the $T_{\rm spec}-$based observations masks the need for an additional heating or redistribution mechanism in the more massive groups.

It is instructive to compare our results to those of the "stellar feedback only" run from the OWLS collaboration (referred to as the "Reference Model" in McCarthy et al. 2010 and as the "ZCool+SF+SN model" in McCarthy et al. 2011). This model (hereafter referred to as OWLS-stars) primarily accounts for only SNe feedback, which is implemented via the kinetic wind model of Dalla Vecchia & Schaye (2008), where the mass loading factor is fixed to constant ($\eta = 2$) instead of varying inversely with galaxy velocity dispersion as in our model and the wind velocity is also set to a constant, 600 km/s. Comparing the resultant $L_X - T_X$ for the simulated groups (*c.f.,* right panel of Figure 6 in McCarthy et al., 2010), we find that the groups in

the OWLS-stars run are about a factor of ~ 10 more luminous than our groups at $T \approx 0.5$ keV, and about a factor of ~ 2 more luminous than our groups at $T \approx 1$ keV. While our results match the observed $L_X - T_X$ relationship, theirs lie systematically above the observations and define a shallower trend. A comparison with the results shown in McCarthy et al. (2011) indicates that this difference is due to a larger IGrM component within R_{500} in the OWLS-stars groups and possibly that the IGrM is more centrally concentrated and hence, denser. We will comment on this further in the next section where we discuss the IGrM and the baryon fractions in our groups.

Finally, we note that the error bars on the simulation results indicate 1-σ scatter above and below the mean. The scatter in the observational data is significantly larger. There are a number of possible reasons for this difference. First, our simulations are missing AGN feedback and one can imagine that the variations introduced by yet another heating/redistribution mechanism could increase the dispersion in the X-ray luminosity of the simulated groups at a fixed temperature (see, for example, McCarthy et al., 2010). The observations, however, are also not homogeneous. For instance, we plot all groups in Osmond & Ponman (2004), including those in which the X-ray emission is only detected to a relatively small radial extent. This can artificially enhance the scatter. In fact, most group samples, including the ones plotted, are not statistically representative (O'Sullivan et al., 2014) and the inhomogeneities and biases will also be reflected in the scatter.

Figure 3.2 shows the $L_X - M$ trends for the simulated groups at redshifts $z = 0$ (black), $z = 0.5$ (blue), $z = 1$ (red), $z = 2$ (green) and $z = 3$ (cyan). This time we plot the rest-frame 0.1-2.4 keV X-ray luminosity to facilitate comparison with available observations. Like the $L_X - T_{\rm spec,corr}$ curves, once cosmic evolution is taken into account through the dimensionless Hubble parameter $E(z)$, the $L_X - M$ curves for the $z \leq 1$ group populations scale as $L_x \propto M_{500}^{1.7}$ and essentially lie on top of each other, implying a self-similar evolution over this redshift range. Like the $L_X - T_{\rm spec,corr}$ relations, the higher redshift curves lie off those at $z \leq 1$ and the deviation goes in the same direction. The groups at a given value of $M\,E(z)$ – note that temperature and $M\,E(z)$ are equivalent measures of the depth of the gravitational potential well – are less luminous than predicted by the self-similar evolution model and the underlying reasons, on which we will elaborate when we discuss the behaviour of the hot gas fraction in the groups, are also the same.

There are two different types of observational data shown in the plot: One set (black circles and stars), where the group masses are in fact hydrostatic mass estimates

derived from the X-ray measurements by Eckmiller, Hudson & Reiprich (2011) and Pratt et al. (2009), respectively, and another (black, blue and red squares), where the masses are derived using weak lensing methods (Laganá, de Souza & Keller, 2010). It is well known that the hydrostatic masses typically underestimate the true mass and to facilitate a fair comparison with our *actual* mass determinations, we have corrected the Pratt et al. (2009) and Eckmiller, Hudson & Reiprich (2011) masses using the bias factor determined by Haines et al. (2015) (see also Mahdavi et al., 2013). Our numerical results are in good agreement with the observational results. Moreover, the fact that the $L_X - M$ trends delineated by the black, blue and red points show no significant offsets from each other suggests that the evolution of the observed group $L_X - M$ relation is consistent with that predicted by the self-similar model over the redshift range $0 \leq z < 1$, which is also in agreement with our numerical results.

Figure 3.3 shows the $M - T_{\rm spec,corr}$ trends for the simulated groups at redshifts $z = 0$ (black), $z = 0.5$ (blue), $z = 1$ (red), $z = 2$ (green) and $z = 3$ (cyan). Once cosmic evolution is taken into account, all the curves, even those for $z > 1$ groups, lie on top of each other. The shape of these curves differs from that shown in Figure 2.3 because there we had plotted mass versus emission-weighted temperature whereas here we are using the core-corrected *spectroscopic* temperature. Comparing the $M - T$ relation for our simulated $z = 0$ groups to that of OWLS-stars groups (*c.f.,* Figure 5 of McCarthy et al., 2010, – this figure shows mass versus emission-weighted temperature whereas we plot mass versus spectroscopic temperature), we find that the two are in excellent agreement with each other once the differences between the two temperatures at $T_{\rm spec,corr} \gtrsim 0.8$ keV are accounted for.

As in Figure 3.2, we plot corrected hydrostatic masses (squares and triangles) and masses derived from weak lensing analyses (black and blue diamonds). Within the scatter, all the data (weak lensing and X-ray based, present-day and at moderate redshift) are consistent with each other. Focusing on measurements with $T_{\rm spec,corr} > 0.8$ keV, the scaling of mass with temperature can be well described by $M_{500} \propto T^{1.6}_{\rm spec,corr}$, which is consistent with the self-similar scaling relationship. The numerical trends, on the other hand, are steeper in the neighbourhood of 1 keV but flattens at both higher and lower temperatures. In spite of this, the numerical results are consistent with the observations except perhaps for the most massive groups with $M_{500} \gtrsim 10^{14}$ M$_\odot$. In these massive systems, the temperature in the simulated systems seems to be a bit cooler than that in the observed systems. We note that this divergence at the high mass end is also present in the $L_X - T_{\rm spec,corr}$ plot.

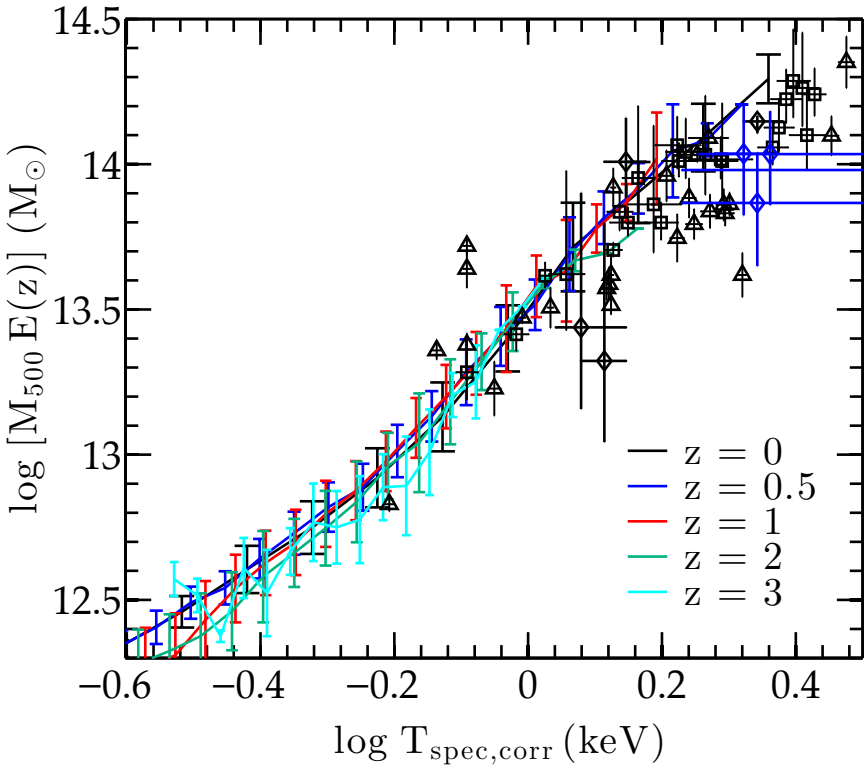

Figure 3.3: $M - T_{\rm spec,corr}$ relation for simulated groups at $z = 0$ (black), $z = 0.5$ (blue), $z = 1$ (red), $z = 2$ (green), and $z = 3$ (cyan). The error bars show 1-σ scatter. The black squares and triangles show the results from Sun et al. (2009) and Eckmiller, Hudson & Reiprich (2011). The hydrostatic mass estimates given in these two studies have been corrected for the hydrostatic bias (Haines et al., 2015). We also note that the temperatures in the latter study are not always extracted in a consistent, systematic fashion. The diamonds show results from Kettula et al. (2013); their masses are weak-lensing estimates. The observed groups at $z \leq 0.25$ and $0.25 < z \leq 0.75$ are plotted as black and blue symbols, respectively.

At various points in the preceding discussion, we have noted that the trends exhibited by the simulated groups in the $L_X - T_{\rm spec,corr} - M$ space are the consequences of two different types of processes: (1) the structure of the intergalactic medium that collapses to form the IGrM and, therefore, the properties of the IGrM itself, are altered by the galactic outflows from an earlier ($z > 2$) generation of galaxies; and (2) heating and/or cooling processes occurring once the groups form can convert the cooler, denser, X-ray luminous gas into either hotter, more diffuse (and therefore, less luminous) gas, or into cold, dense gas that is effectively dark in the X-rays. To gain insights into the relative importance of these effects, we examine the entropy of the hot X-ray emitting gas.

3.1.2 The Entropy-Temperature Scaling

Entropy is a very useful physical quantity to consider when the IGrM is subject to cooling and heating processes because the former typically lowers the entropy while the latter always raises it. This is not the case with either density or temperature because heating can cause the gas to expand, potentially lowering both quantities (see McCarthy et al., 2008, for a more detailed discussion). Additionally, the gas distribution will tend to organize itself so that the lowest entropy gas is at the group centre and the highest is at the group periphery. On the other hand, in the present situation, there is an additional complication to keep in mind: If cooling is able to cause the low entropy IGrM in the center to drop out and settle in the central galaxy, higher entropy gas from further out will flow in to take its place and the entropy in the centre will appear "enhanced" unless cooling is able to erode the entropy of this inflowing gas as quickly as it flows in. This effect was first seen in the numerical simulation by Lewis et al. (2000) and discussed more fully by Voit & Bryan (2001).

In Figure 3.4, we show the cosmic expansion corrected gas entropy at R_{500} (top panel) and R_{2500} (bottom panel), in present-day groups (black solid curve) as well as for groups at $z = 0.5$ (blue), $z = 1$ (red), $z = 2$ (green), and $z = 3$ (cyan), as a function of the integrated core-corrected spectroscopic temperature of the IGrM within R_{500} . We also plot entropy estimates from the X-ray observations of Sun et al. (2009), computed using the deprojected temperature and electron density profiles. To be precise, we are *not* plotting the actual thermodynamic specific entropy, but rather its widely accepted proxy[2] given by

[2]The 'entropy proxy' (S) and the thermodynamic specific entropy (s) are related to each other

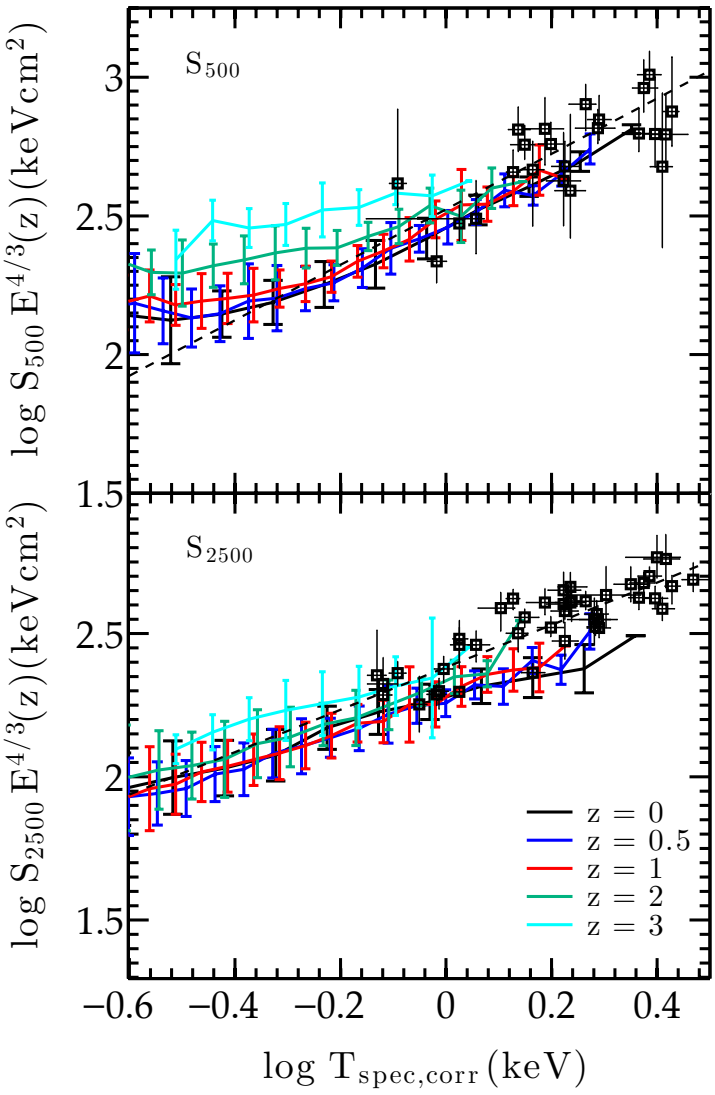

Figure 3.4: Gas entropy at R_{500} (top panel) and R_{2500} (bottom panel) of the simulated groups at $z = 0$ (black), $z = 0.5$ (blue), $z = 1$ (red), $z = 2$ (green) and $z = 3$ (cyan), as a function of core-corrected spectroscopic temperature. The error bars show 1-σ scatter. The observational data of the low redshift sample from Sun et al. (2009, hereafter S09) is shown by black squares. The dashed lines in the top and bottom panels represent the power-law fits to the $S - T$ relation at the two different radii for the full group+cluster sample from S09, with a power law index of 1 and 0.74, respectively.

$$S(r) = \frac{k_B T_{\rm spec}(r)}{n_e(r)^{2/3}} \,, \tag{3.1}$$

where k_B is the Boltzmann constant, and $T_{\rm spec}(r)$ and $n_e(r)$ are, respectively, the spectroscopic temperature and the electron number density within a thin spherical shell at radius r. We shall, hereafter, refer to $S(r)$ as 'entropy'.

Focusing first on the R_{500}, we see that scaled entropy systematically declines with time. The change is much greater at high redshifts ($z > 1$) than at low redshifts ($z < 1$) and also, much more stronger in groups with shallow potential wells than in those with deep potential wells. Both results are primarily driven by the evolution in the IGrM density at R_{500}. For group halos of a given temperature, if we take the present-day value of IGrM density at R_{500} as a reference, then we are led to conclude that the IGrM density at R_{500} at an earlier epoch is not $E(z)^2$ times the present-day value, as would be expected if the IGrM density were evolving self-similarly. Rather, it is lower than the expected value and hence, the cosmic expansion corrected entropy is higher. Put another way, the halos at $z = 3$ are IGrM poor (relative to the total matter). As the halos grow, they encompass additional dark and baryonic matter but the ratio of baryons-to-dark matter is larger than the universal value. In effect, the groups are recapturing some of the baryons that were ejected from their member galaxies at earlier times, in addition to the usual complement associated with the accreting dark matter (reminiscent of the "outside-in" IGM enrichment scenario of Oppenheimer et al. 2012). The higher temperature groups are able to recapture a greater fraction of the previously expelled baryons at an earlier time ($z > 2$) than the lower temperature groups. The outcome of this differential accretion of baryons and dark matter is that the density of hot gas in the groups evolves differently from self-similar expectations – *i.e.,* until $z \approx 1$, after which the evolution of the entropy and the density for all the group halos is consistent with self-similar evolution. We will examine the density and entropy profiles in detail in future work. However, this general behaviour also explains the self-similar evolution of the $L_X - T_{\rm spec,corr}$ and $L_X - M$ from $z = 0$ to $z = 1$ and then, the decrease in the amplitude of the (cosmic expansion corrected) scaling relation from $z = 1$ to $z = 3$ (*c.f.,* Figures 3.1 and 3.2). At higher redshifts, the groups of a given temperature or M$E(z)$ (both are equivalent measures) are not as luminous as they ought to be if they were evolving self-similarly because the IGrM is not as dense as self-similarity would predict.

as $ds \propto d\ln S$ (see Balogh, Babul & Patton, 1999).

In contrast with S_{500}, S_{2500} evolves somewhat differently. The scaled entropy evolves self-similarly from $z \approx 2$ to the present and even between $z = 3$ and $z = 2$, the change is relatively mild. The core regions tend to form earlier and we expect that they will settle down into a steady-state configuration at an earlier epoch. DOS08 compared the core entropies of groups in a simulation with and without outflows and found that the gas in the former case had higher entropy. This is a non-trivial result. As we mentioned above, it is not unexpected to see elevated entropies at R_{2500} in simulations with cooling, star formation and inefficient stellar feedback (hereafter simulations – for more details about such simulations, see Lewis et al., 2000; Kravtsov, Nagai & Vikhlinin, 2005, and DOS08), relative to a non-radiative simulation (*c.f.,* Figure 10 of Lewis et al. 2000). The inclusion of outflows, however, could just as easily have led to still higher core entropies, or lower core entropies. As DOS08 explain, the latter can occur if heating from the outflows just balances cooling, and the low-entropy gas remains in place unchanged, *i.e.,* it is neither removed via cooling nor raised to a higher adiabat. The outflows in our simulations, on average, heat the IGrM at least close to the centre of the groups.

Comparing S_{500} and S_{2500} entropy results for our simulated groups to the observations, we find that the IGrM entropy at R_{500} in our massive groups is consistent with the observations. Sun et al. (2009) find that the observed S_{500} values scale with the integrated core-corrected spectroscopic temperature of the gas within R_{500} as $S_{500} \propto T_{\rm spec,corr}$ (dashed line) across their full sample of groups and clusters. Our simulation results also follow the same scaling for $T_{\rm spec,corr} > 0.3$ keV. Below this threshold, S_{500} in the simulated groups flattens. This flattening is because of a decrease in the IGrM density with decreasing group mass. We will discuss this further in the next subsection. At R_{2500}, Sun et al. (2009) find that the observed entropy scales as $S_{2500} \propto T^{0.74}_{\rm spec,corr}$ (dashed line). The S_{2500} of the groups in the simulated sample is less steep, scaling with temperature as $S_{2500} \propto T^{0.50}_{\rm spec,corr}$, and the simulated groups at the high mass end have approximately 40% lower core entropies compared to the observations. One explanation is that the density of IGrM in the cores of the massive simulated groups is slightly higher than in real groups and this, in turn, would explain why massive simulated groups seem to be somewhat more X-ray luminous than their real counterparts.

Comparing our entropy results to those of groups in the OWLS-stars run (see Figure 2 in McCarthy et al., 2010), we find that entropy at R_{500} in the two simulations is very similar. At R_{2500}, however, the entropy in the OWLS groups is lower than

in our groups by approximately $25 - 30\%$. This supports our previous conjecture that the IGrM in OWLS groups is more centrally concentrated than in our groups, which in turn would explain the differences in the X-ray luminosities of the two group populations.

Overall our stellar-powered wind model fares remarkably well when it comes to matching the observed group $L_X - T_{\rm spec,corr} - M$ scaling relations except perhaps in the most massive groups. The behaviour of the IGrM entropy at R_{2500} and R_{500} suggests that the principal variable governing the behaviour of these relationships in our simulated groups is the IGrM density.

3.2 THE BARYON CONTENT OF GALAXY GROUPS

We now turn to direct determinations of the total baryon fraction as well as the stellar and the IGrM gas mass fractions in the simulated groups to confirm whether the IGrM density behaves as we have argued above, and try to understand the reasons behind its behaviour. The partitioning of the baryons between stars and hot gas is interesting in and of itself. We know that our model is not able to suppress the overproduction of stars in the largest galaxies in the groups (*c.f.,* Figure 2.2) but by looking into the issue more carefully, we hope to understand when and where the model starts to fail. Additionally, we also quantify the assembly of the groups using several different measures.

3.2.1 Stellar, Gas and Total Baryon Fractions

The sequence of plots in the left panel of Figure 3.5 shows the total baryon, $T > 5 \times 10^5$ K, hot, diffuse gas (IGrM), stellar, and cold gas fractions in simulated groups at $z = 0$, as function of the total group mass. All the quantities are computed with R_{500} to facilitate comparisons with the observations. The plots in the right column show the same mass fractions within R_{200} to illustrate their behaviour across group populations at different redshifts as well as beyond just the inner regions of the halos. The coloured lines show the results for groups at $z = 0$ (black), 0.5 (blue), 1.0 (red), 1.5 (magenta), 2.0 (green) and 3.0 (cyan). On the x-axis, we plot $M_{200}\,E(z)$ so that we can compare populations of halos with potentials of similar depths across the different epochs. Baryon properties, as well as the impact of feedback and radiative cooling, both tend to be strongly correlated with the depth of the halos' gravitational

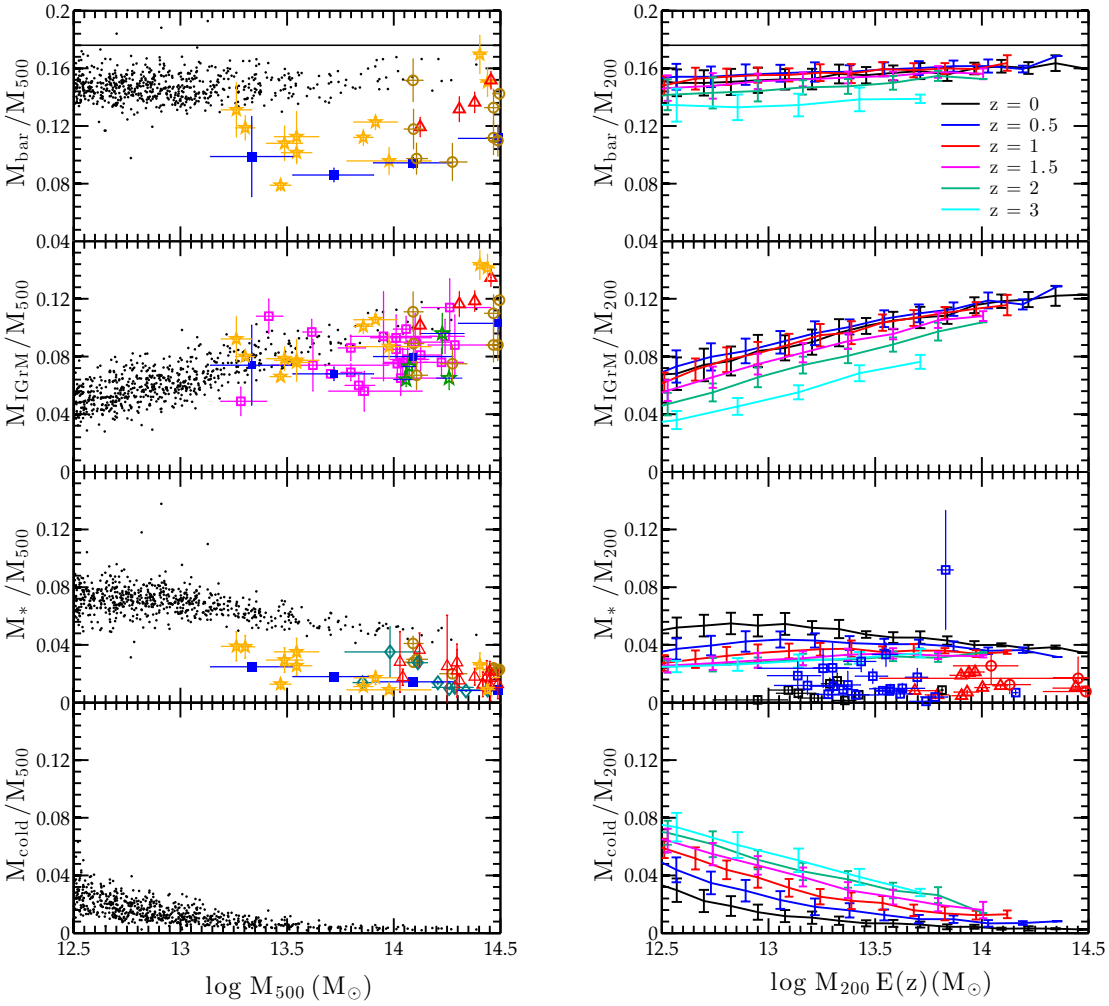

Figure 3.5: Left column: Stellar and gas mass fractions within R_{500} in simulated $z = 0$ groups. *Top panel*: Total baryonic fraction. The black line indicates the cosmological value, $\Omega_b/\Omega_m = 0.176$. The symbols (see text for details) show observational estimates for hot gas + stars. Error bars depict 1-σ scatter. *Second panel*: Hot gas fraction. *Third panel*: Stellar mass fraction. The simulation results include stars in the galaxies as well as those comprising the diffuse intragroup stars [IGS]) component. Of the observational estimates, only the golden circles (Gonzalez et al., 2013) account for the IGS. *Bottom panel*: Cold gas fraction (*i.e.* diffuse gas with $T < 5 \times 10^5$ K and the galactic ISM). Right column: The same mass fractions for simulated groups at $z = 0$ (black), $z = 0.5$ (blue), $z = 1$ (red), $z = 1.5$ (magenta), $z = 2$ (green) and $z = 3$ (cyan) computed within R_{200} to facilitate comparison with observations. Triangles, circles and squares are observational results from McCourt, Quataert & Parrish (2013), van der Burg et al. (2014) and Connelly et al. (2012), respectively. Data for $z \lesssim 0.25$ groups are in black, $0.25 < z \lesssim 0.75$ in red, and $0.75 < z \lesssim 1.25$ groups in blue. These do not account for the IGS.

potential well. For completeness, we note that we have tracked the evolution of individual groups in the right column of Figure 3.5 and find that once formed, they *do not* simply evolve vertically in these plots. Rather, they move both vertically up or down (depending on the quantity under consideration) with decreasing redshift, transitioning from one coloured line to the next, while also generally sliding to the right along the x-axis. This is because the masses of individual groups generally grow faster than expected under the self-similar growth model; *i.e.,* they increase faster than $M_{200}(z_{\rm group})\,[E(z_{\rm group})/E(z)]$, where $z_{\rm group}$ is the redshift at which the most massive progenitor halos of the present-day groups first acquire three luminous galaxies and as per our definition, become 'groups'. Consequently, the potential well of individual groups tend to deepen towards the present.

In the first panel of both columns, we investigate the total baryon fraction. The solid line indicates the cosmological baryon fraction of $\Omega_b/\Omega_m = 0.176$ for the simulation. The red triangles, blue squares, golden circles and orange stars in the left panel show observational estimates of the fraction of mass in hot gas and stars, which for massive groups is essentially the same as the total baryon fraction, from Lin, Mohr & Stanford (2003), Giodini, Pierini & Finoguenov (2009, revised[3]), Gonzalez et al. (2013), and Laganá et al. (2013), respectively. Of these, only Gonzalez et al. (2013) (golden circles) explicitly account for the extended, diffuse intragroup stellar component (hereafter referred to as the intragroup stars or IGS). The simulation results include all stars, those in the galaxies as well as those that belong to the extended population. In spite of the large scatter in the observed values, the total baryon fraction within R_{500} in our simulated present-day groups is generally greater than that in real groups by approximately $35-40\%$.

This is the first indication that powerful stellar-powered galactic outflows, in and of themselves, are not capable of preventing the over-concentration of baryons within R_{500} in the simulated groups, in comparison to the observations. This is not to say that the outflows have no impact on the galaxy groups. The baryon fraction of our simulated groups is comparable to that seen in non-radiative simulations (see for instance Crain et al., 2007) – *i.e.,*simulations that do not allow for cooling. It is most definitely lower than the values seen in the simulations (Lewis et al., 2000; Kravtsov, Nagai & Vikhlinin, 2005, DOS08), where the baryon fraction within R_{500} is typically

[3]The results for Giodini, Pierini & Finoguenov (2009) shown in Figure 3.5 differ from those in their paper because they have been revised as suggested by Leauthaud et al. (2012). See also discussion in Giodini et al. (2012). The stellar masses results presented are derived using the Chabrier IMF.

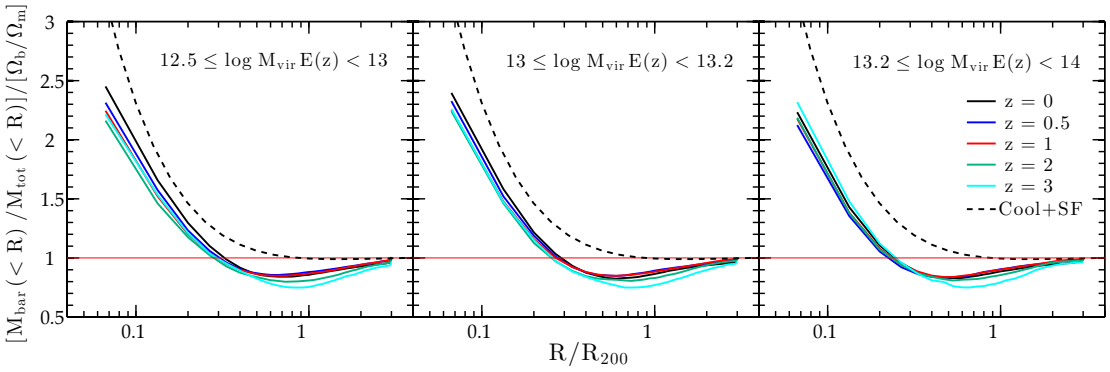

Figure 3.6: The mean baryon fraction within radius R/R_{200} in simulated groups at $z = 0$ groups (black curve), $z = 0.5$ (blue), $z = 1$ (red), $z = 1.5$ (magenta), $z = 2$ (green) and $z = 3$ (cyan), normalized to the cosmic baryon fraction $\Omega_b/\Omega_m = 0.176$ for the simulation. We have sorted the groups into three bins according to the depth of their potential wells: In each panel, the dashed black curve shows the $z = 0$ mean baryon fraction profile for the simulation from Lewis et al. (2000), which had no galactic winds.

equal to or even slightly larger than the universal value. Below we try to understand precisely how the galactic outflows affect the baryon fraction in our simulated groups.

Examining the simulation results more closely, we note that the median value of the baryon fractions within R_{500} in the $z = 0$ groups exhibits a gradual rise with increasing halo mass, going from $\sim 82\%$ of the universal cosmological value in the least massive groups to $\sim 90\%$ of the universal value in the most massive groups. Comparing these results against those for the OWLS-stars groups (in this case "ZCOOL+SF+SN" simulation; McCarthy et al. 2011), we find good agreement. The median baryon fractions in the latter groups range from 88% of the cosmological value in the lower mass groups to 92% in the high mass systems. The median baryon fractions within R_{200} of the $z = 0$ groups also increases gradually with halo mass, from $\sim 86\%$ of the universal value in our lowest mass groups to $\sim 93\%$ in the high mass groups. The baryon fractions within R_{500} are slightly but systematically lower than within R_{200} because, in our simulated groups, the principal source of outflows is the dominant central galaxy and as noted while discussing the IGrM entropy, these preferentially heat the gas in the central regions.

The trend highlighted above, of lower mass systems being more baryon depleted, is a common feature of the strong stellar feedback models. In the case of the momentum-driven wind model, Davé (2009) has shown that the baryon fraction in present-day Milky Way-sized halos ($\sim 10^{12}$ $M_\odot$) drops to 60% of the cosmic value and decreases further to below 50% of the cosmological value in lower mass galactic halos ($\sim 10^{10}$ $M_\odot$). On these galactic scales, the reason is fairly clear. The winds physically carry away a large fraction of the baryons from such systems and in fact, can drive down the baryon fraction over regions that extend well beyond the virial radius of the galactic halos. Similar results are also seen in other "no AGN" simulations where stellar feedback is implemented via a thermal prescription (see Sokołowska et al., 2015, and references therein).

As one moves up in halo mass, the deepening gravitational potential wells engender a transition from a state where the bulk of the baryonic matter within a halo is in the form of stars and cold gas localized in the galaxy (or galaxies), to one where the hot diffuse gas component that suffuses the entire halo eventually dominates the baryon budget. This transition has been discussed in detail by Knobel et al. (2009) and Gabor & Davé (2015), and references therein. Following Gabor & Davé (2015), we define the transition point between these two states as one where the hot gas mass exceeds 50% of the total *gas* mass. In our simulations, this changeover group

mass occurs at $M_{200} \approx 1.8 \times 10^{12}$ M$_\odot$ at $z = 0$, $M_{200} \approx 3 \times 10^{12}$ M$_\odot$ at $z = 1$ and $M_{200} \approx 6.3 \times 10^{12}$ M$_\odot$ at $z = 2$. These masses are comparable to the transition mass cited in Gabor & Davé (2015) although in detail our transition masses are slightly larger because we impose an additional constraint that the halos must host at least three luminous galaxies. The presence of a pervasive IGrM alters the wind dynamics: Galactic winds flowing through such a medium are subject to hydrodynamic drag, the relative importance of which grows as the density of the medium increases. In the case of our group halos, the combination of the deeper gravitational potential wells and the higher likelihood of strong hydrodynamic interactions results in the winds being almost completely confined within the halos. So the reduced baryon fraction, relative to the cosmic mean, is *not* due to the outflow of the baryons.

Instead, the reduced baryon fraction in the group halos is the result of the following two effects. First, groups typically form in regions that have been rendered somewhat baryon deficient by winds from their member galaxies at earlier times. Consequently, when the groups first form, their baryon fraction can be as low as $\sim 75\%$ of the cosmic mean, as illustrated by the baryon fraction curve for $z = 3$ groups in the top right panel of Figure 3.5. This "baryon depletion" is illustrated much more clearly in Figure 3.6. At $z \approx 3$, for example, the baryon fraction within R_{200} is $75\% - 77\%$ of the mean value for the simulation, and one would have to go out to $\sim 3R_{200}$ before the fraction returns to the cosmic mean. (For comparison, we also show the baryon fraction profile for a simulation from Lewis et al. (2000); the baryon fraction never really drops below the mean value and converges to the mean value by R_{200}.) This depletion is slightly less pronounced in the more massive groups and diminishes towards the present.

Returning to the top right panel of Figure 3.5, we have noted previously that individual groups, once formed, tend to grow in mass. And as the halos grow, their physical reach extends further out. As a result, in addition to the inflow of the usual baryonic complement of the accreting dark matter, they are also able to recapture an increasing fraction of the expelled gas previously associated with the group galaxies (*c.f.,* Ford et al., 2014, for a discussion of a similar phenomenon in galactic halos.), and the overall baryon fraction increases with halo mass.

This, however, is not all. There is a second effect at play, otherwise we would expect the baryon fraction to continue rising with decreasing redshift and approach the mean cosmological value. Instead, we observe a sharp increase in the halo baryon fraction between $z = 3$ and $z = 2$, a much more tempered rise from $z = 2$ to $z = 1$,

and very little change, if any, thereafter. This second effect is the result of the winds ejected from the group galaxies interacting with and heating the hot halo gas, which not only reduces the rate at which the halo gas cools and accumulates in the group central galaxies but also causes its distribution to *remain* more extended.

In the preceding discussion, we use the word "extended" deliberately. Hot gaseous halos generally extend beyond the virial radius (*c.f.,* Bahé et al., 2013; Gabor & Davé, 2015) but in simulations without winds, radiative cooling inside the halos leads to the loss of pressure support, which then results in a denser, more compact baryon distribution. In the case of our wind model, the hot halo gas density starts out lower than usual and it is easier for heating by the winds to compensate for a significant fraction of the radiative cooling losses and drastically slow down its collapse. As indicated in the top right panel, halos with gravitational potential wells of a given depth (*i.e.,*at a fixed $M_{200}E(z)$) establish an equilibrium distribution by $z = 1$, and the baryon fraction remains essentially constant from $z = 1$ to the present.

However, the efficacy of the galactic winds to maintain an extended hot gas distribution via heating drops with deepening potential wells because the characteristic temperature ($T_{\rm wind}$) corresponding to the complete thermalization of the kinetic energy in the outflows from any one galaxy in a group halo, even the dominant galaxy, does not grow as quickly as the group halo's virial temperature ($T_{\rm vir}$). The reason for this is that $T_{\rm wind}$ scales as $M_{\rm gal}^{2/3}$, where $M_{\rm gal}$ is the mass of individual galaxies, whereas $T_{\rm vir}$ grows as $M_{200}^{2/3}$ and as we explain below, the fraction of the baryons condensing into the cold gas+stars phase decreases with increasing group halo mass. Moreover, by virtue of being multi-galaxy systems, even the baryons that have condensed out are distributed over 3 or more "luminous" galaxies. In the end, the IGrM is not able to withstand gravitational compression despite being heated.

The second set of panels in Figure 3.5 show the diffuse hot ($T > 5 \times 10^5$ K) IGrM gas fraction in the simulated groups. The IGrM fraction within R_{500} (left column) nearly doubles, from ~ 0.05 to 0.1, in going from $M_{500} \approx 3 \times 10^{12}$ $\rm M_\odot$ to $M_{500} \approx 10^{14}$ $\rm M_\odot$. This increase with group mass is the result of the larger mass systems having deeper potential wells and higher virial temperatures. As a result, more of the diffuse gas is shock-heated to constitute the IGrM. Additionally, the deeper potential wells are also better able to compress and confine this gas.

Comparing our results against Figure 4 of McCarthy et al. (2010), we find that the IGrM gas fraction within R_{500} of comparable groups at the low mass end of the group distribution in our simulation is about 30% lower (*i.e.,* 0.053 for our groups

versus 0.07 for the OWLS-stars groups) and about 10% lower for the groups at the high mass end. The lower IGrM fraction is a key reason why our simulated groups are less X-ray luminous than the OWLS-stars groups. We do note that McCarthy et al. (2010) define the IGrM using the temperature cut of $T > 1 \times 10^5$ K instead of $T > 5 \times 10^5$ K, as we have. However, we have recomputed the IGrM fraction for our groups using this lower threshold and find negligible changes to our results.

Comparing the simulation results for the $z = 0$ IGrM fraction within R_{500} (left panel) against observations (red triangles, open magenta squares, green stars , filled blue squares, golden circles, and orange stars are data from Lin, Mohr & Stanford (2003), Sun et al. (2009), Sanderson, O'Sullivan & Ponman (2009), Giodini, Pierini & Finoguenov (2009), Gonzalez et al. (2013), and Laganá et al. (2013), respectively), we find that the two are in reasonable agreement. In detail, there is a hint that the IGrM fraction in the simulated groups is rising slightly faster with increasing group mass but it is difficult to be more definite given the large scatter in the observations. Such a trend would, however, be consistent with our previous finding that the most massive simulated groups are slightly more X-ray luminous than real systems and that the stellar-powered winds are unable to keep the baryon fraction from creeping upwards. Together, all of these suggest the need for another gas heating/redistribution mechanism.

The right panel in the second row of Figure 3.5 shows the IGrM fraction in the groups at different redshift. Like the results for the baryon fraction (top right panel), the IGrM fraction in halos with comparable potential wells increases between $z \approx 3$ and $z \approx 1$ and then, stabilizes. Since most of the freshly accreted baryons directly contribute to the IGrM over the epochs and in the halo mass regime being considered, that the total baryon and the IGrM fractions behave similarly is not surprising.

To investigate the make-up of the present-day IGrM within R_{200} in detail, we have tracked all the IGrM gas particles back in time and tagged all those that, at any point in the past, were bound to a galaxy *and* enriched while bound. We refer to this component of the present-day IGrM as "processed" and the rest of the gas as "unprocessed."[4] We find that the fraction of the present-day IGrM that is "processed" gas ranges from $\sim 15\%$ in the highest mass groups to $3-4\%$ in the lowest mass groups.

[4] "Unprocessed" material is essentially gas that has never passed through a galaxy and has entered the group halos via diffuse accretion directly from the intergalactic medium. We emphasize that "unprocessed" should *not* be interpreted as un-enriched. A significant fraction of the present-day "unprocessed" IGrM has non-primordial metallicity owing to enrichment by the diffuse IGS component.

(We relaxed the "enriched while bound" condition and repeated the analysis, and got identical results.) This increase in the fraction of "processed" IGrM or equivalently, the decrease in the fraction of "unprocessed" IGrM, with increasing halo mass is the continuation of the trend observed by Ford et al. (2014). On galactic scales ($M_{200} \sim 10^{11}$ M$_\odot$), Ford et al. (2014) find that the "unprocessed" component, which they call "ambient gas", makes up nearly all of the hot gas. That the fraction of processed gas in the IGrM is relatively small even in the most massive groups may seem surprising but only a small fraction of the metal-rich wind material ejected from central galaxies, for example, thermalizes at $T > 5 \times 10^5$ K and remains in the IGrM. Acting more like a galactic fountain, the most of the wind lifts off from the galaxy, transfers its kinetic energy to the ambient gas, and falls back into the galaxy. This behaviour has been discussed in detail in Oppenheimer et al. (2010) and Ford et al. (2014)

The fraction of the gas that is heated to $T > 5 \times 10^5$ K and is lost to cooling is relatively small. Over a Hubble time, it ranges from ∼10% at $M_{200} = 3 \times 10^{12}$ M$_\odot$, to ∼2.5% at $M_{200} = 3 \times 10^{13}$ M$_\odot$, to ∼0.2% at $M_{200} = 3 \times 10^{14}$ M$_\odot$. Most of the gas that drops out of the IGrM is initially heated only to 5×10^5 K $< T < 3 \times 10^6$ K. Metal-enriched IGrM in this temperature range sits on the broad peak of the cooling curve and is subject to efficient cooling, which even heating by stellar-powered galactic winds/fountains cannot fully offset.

The third set of panels in Figure 3.5 show the stellar mass fraction in our simulated groups. We include both stars in the galaxies as well as stars belonging to the diffuse intragroup component (IGS) when we compute the stellar mass. Comparing the stellar fraction within R_{500} in our $z = 0$ simulated groups to the same from the OWLS-stars simulation (McCarthy et al., 2011), we find that the two are similar, ranging from 0.07 in the low mass groups to 0.05 in the high mass groups. Additionally, this stellar fraction, like the baryon fraction, is a significant improvement over those seen in simulations of Lewis et al. (2000) and Nagai, Kravtsov & Vikhlinin (2007), which do not include this type of stellar feedback, confirming that galaxy-wide outflows indeed do suppress excessive star formation. This improvement, however, is not sufficient to bring the simulation results into agreement with the observations. The red triangles, blue squares, green diamonds, orange stars, and golden circles in the left panel show results from Lin, Mohr & Stanford (2003), Giodini, Pierini & Finoguenov (2009)[5],

[5]The results for Giodini, Pierini & Finoguenov (2009) shown in Figure 3.5 differ from those in their paper because they have been revised as suggested by Leauthaud et al. (2012) – see also

Balogh et al. (2011), Laganá et al. (2013), and Gonzalez et al. (2013), respectively. Of these, only the latter account for the IGS component. Compared to the observations, the simulated groups have, on the whole, a factor of ∼2 more mass in stars within R_{500}.

In the right panel, we show how the group stellar fraction within R_{200} changes with redshift. We also plot the observational estimates of the stellar fraction in groups at $z \sim 0.5$ and $z \sim 1$ as blue and red symbols, respectively. These data points should be compared to curves of the same colour. These observational results are among the first estimates of the stellar fraction in groups at higher redshifts and are subject to considerable uncertainty (*c.f.,* discussion in Leauthaud et al., 2012; Gonzalez et al., 2013, for example). This renders a detailed comparison between the simulations and the observations difficult. Nonetheless, the general trend seen in the left panel (*i.e.* at $z = 0$) — that the stellar fraction in the simulated groups is generally higher than in the observed groups – seems to hold out to $z = 1$.

Examining the $z = 0$ simulated groups in a bit more detail, we note that the 'super-sized' galaxies (*i.e.,* the galaxies with $M_* > 10^{11}$ $M_\odot$ that we mentioned when discussing Figure 2.2) contain $\sim$ 85% of the stellar mass within R_{500} in the lowest mass groups, and the fraction drops with group halo mass to $\sim$ 65% in the most massive groups. The average stellar mass of these galaxies ranges from 4×10^{11} $M_\odot$ in the lowest mass groups to 2×10^{12} $M_\odot$ in the most massive groups. Artificially reducing the stellar mass of just these super-sized systems by a factor of 3 resolves the discrepancy between the observed and model stellar mass fractions across the entire mass range over which this fraction has been observationally determined. It also goes a long way towards improving the agreement with observed galaxy stellar mass function (*c.f.,* bottom panel of Figure 2.2).

In all our groups, the group central galaxy is always a "super-sized" galaxy. In the lowest mass groups, $\sim$ 80% of the stars within R_{500} reside in the central galaxy. Examining the stellar build-up in these central galaxies, we find that about 25% of the stars formed elsewhere and were subsequently incorporated into the central galaxies through galaxy-galaxy mergers; 15% of the stars formed *in-situ* from cooled IGrM;[6] and the balance (approximately 60% of the total stellar mass at $z = 0$) formed *in-situ* either from $T < 5 \times 10^5$ K gas that was either originally funnelled onto the central

discussion in Giodini et al. (2012). We show the corrected results based on the Chabrier IMF.

[6]We remind the reader that "cooled IGrM" refers to gas in the MMP that is heated to $T > 5 \times 10^5$ K at some point in the past and cools directly onto the central galaxy.

galaxies via cold mode accretion (Knobel et al., 2009), or from cold gas that was deposited in the central galaxies by mergers. The bulk of the mergers affecting the central galaxies in low mass groups occur either before or just after the groups – that is, systems with at least three "luminous" galaxies – formed.

In the most massive groups, the contribution of the central galaxy to the total stellar mass within R_{500} drops to about 40% and as for the stars that comprise these central galaxies, about 58% were brought in by mergers, 40% formed *in-situ* from cold gas, and only about 2% formed out of cooled down IGrM. These percentages are important in two respects. First, the fraction of the stellar mass in the central galaxies that is deposited by mergers increases with overall halo mass. This trend has been noted previously by Hirschmann et al. (2013) in their study of galaxy-scale halos. Our results show that the trend continues on the group-scale. Second, and perhaps much more importantly, these results show that the overabundance of stars in our simulated groups is *not* primarily due to the cooling of the hot diffuse IGrM despite the fact that we do not have AGNs in our simulation. Unchecked cooling of the IGrM contributes only a small fraction of the excess.

The plots showing the stellar fraction in groups at different epochs offer some idea of what is going on. We have previously noted that once individual groups form, they slide to the right along the x-axis in this plot because the stellar mass in fact grows faster than the actual mass of the group halos in all except the most massive groups. This star formation is fuelled by an excess of cold gas that has accumulated in the group galaxies while these galaxies are at the centres of their own halos either *before* the groups form, in the case of the central galaxies, or *before* they are incorporated into the groups, in the case of the satellite galaxies.

We can see evidence for the presence of significant cold gas in the group galaxies in the bottom two panels of Figure 3.5. The panels show the total mass fraction of "cold" gas in the groups, where "cold gas" includes both the diffuse gas with $T < 5 \times 10^5$ K as well as the dense gas that comprises the ISM in group galaxies. In practice, the former is negligible because diffuse gas with temperatures $T < 5 \times 10^5$ K lies on the broad peak of the cooling curve, experiences very efficient cooling and ends up flowing into the central galaxy. The gas in groups is typically either hot and diffuse or cold and dense. At any redshift, the lowest mass groups, which are also typically the youngest within the population, have the most amount of cold gas. In the same vein, the earliest groups have the highest cold gas fraction. Taken jointly, these results show that the galaxies, especially the more massive galaxies, that first come together

to form the groups contain a significant cold gas reservoir. As the groups grow and age, the cold gas reservoir is not replenished as rapidly as it is consumed by star formation, and the cold gas fraction drops. We note that there is also considerable merger activity, especially early in the history of the groups, during which some of the massive satellites sink to the centre and are cannibalized by the group central galaxies, and while this impacts the distribution of the stars and the gas within the groups, it does not affect the curves in Figure 3.5 because we are considering the total stellar and cold gas fractions within R_{200}.

Demonstrating that the group galaxies host a significant fraction of cold gas is not the same as asserting that the group galaxies have an excess of cold gas. We therefore turn to two recent studies to compare the cold gas content of the most massive of our $z = 0$ group galaxies to real galaxies: (1) The Saintonge et al. (2011) sample that comprises 350 nearby massive ($M_* > 10^{10}\,\mathrm{M}_\odot$), of which 222 have both CO and HI measurements. We focus on the latter subset and compute the "cold gas" mass of each galaxy as $M_{\mathrm{coldgas}} = (M_{\mathrm{HI}} + M_{\mathrm{H_2}})/X$, where the division by $X = 0.75$, the hydrogen mass fraction, corrects for the helium mass. (2) The Catinella et al. (2013) study that lists HI measurements for 800 galaxies with stellar masses $10^{10} \lesssim M_* \lesssim 10^{11.5}\,\mathrm{M}_\odot$ and redshifts $0.025 \leq z \leq 0.05$. We convert the HI masses to total cold gas mass using a constant ratio of $M_{\mathrm{H_2}}/M_{\mathrm{HI}} = 0.295$, based on the results of Saintonge et al. (2011), and $X = 0.75$.

Both studies yield a mean cold gas mass of approximately $5 \times 10^9\,\mathrm{M}_\odot$ for galaxies with $M_* > 10^{11}\,\mathrm{M}_\odot$. We specifically restrict ourselves to such massive galaxies because the vast majority of the galaxies that populate the two most massive bins in M_* in the Catinella and Saintonge samples are, in fact, group galaxies. For the simulated galaxies, we follow Davé, Finlator & Oppenheimer (2011b) and define "cold star-forming gas" as gas within the galaxies whose density exceeds the star formation threshold of $n_{\mathrm{H}} > 0.13\ \mathrm{cm}^{-3}$ (*c.f.,* Section 2.1). The resulting cold gas mass in our simulated $M_* > 10^{11}\,\mathrm{M}_\odot$ group galaxies is 5-6 times larger.

Further investigation indicates that our hierarchical structure formation model, in which feedback is entirely due to stellar-powered galactic outflows, first breaks down not on the group scale but rather in the giant galaxies (with stellar mass $\gtrsim 4 \times 10^{10}\,\mathrm{M}_\odot$) that precede the formation of the groups. These are the first systems in the hierarchy where the deepening gravitational potential wells and a higher cross-section for hydrodynamic interactions between the galactic outflows and the shock-heated halo gas component, once the latter starts to form, are able to confine the outflowing

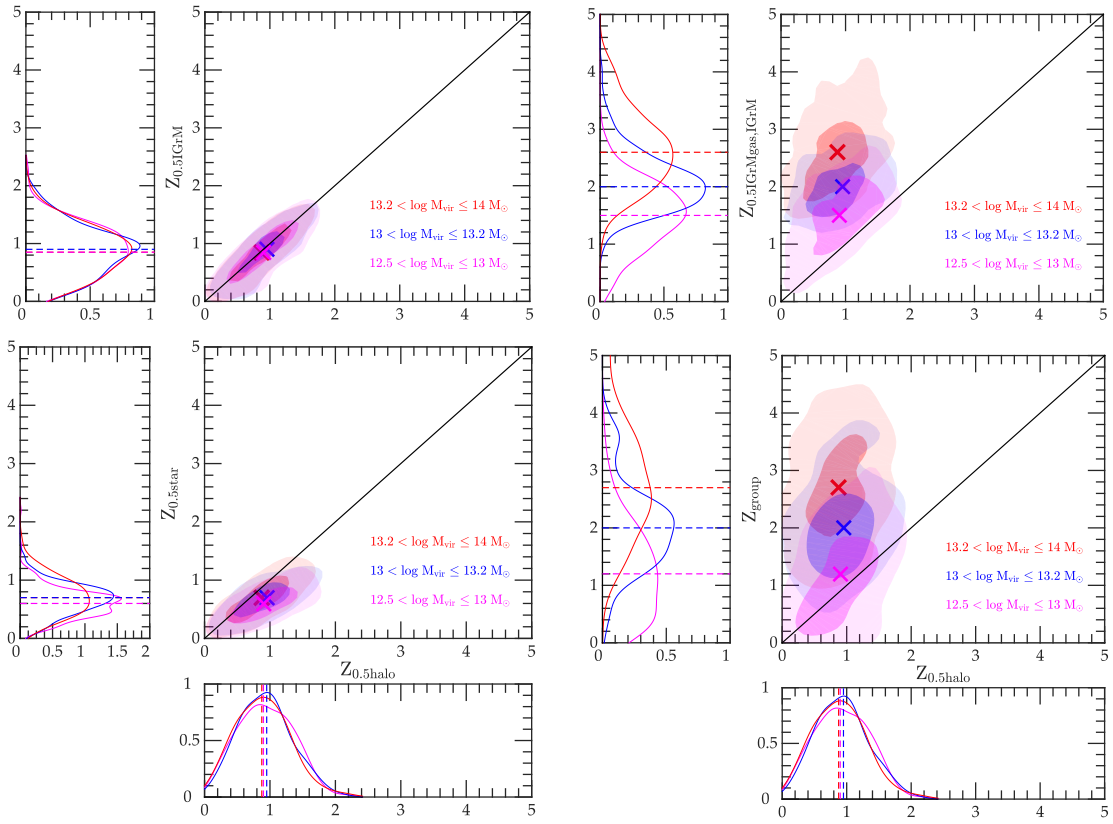

Figure 3.7: A set of four plots showing the distribution of the five key redshifts that summarize the groups' formation histories, defined in Section 4.2.2, and the relationships between them: $Z_{0.5\ \mathrm{IGrM}}$ vs. $Z_{0.5\ \mathrm{halo}}$ (top left); $Z_{0.5\ \mathrm{MMP_{gas},IGrM}}$ vs. $Z_{0.5\ \mathrm{halo}}$ (top right); $Z_{0.5\ \mathrm{star}}$ vs. $Z_{0.5\ \mathrm{halo}}$ (bottom left); and Z_{group} vs. $Z_{0.5\ \mathrm{halo}}$ (bottom right). In the main plot of each set, the different colored regions show the 2D distribution of the redshifts for the low, intermediate and high mass groups – *i.e.*, $12.5 < \log M_{\mathrm{vir}} \leq 13.0\ \mathrm{M}_{\odot}$ (magenta), $13.0 < \log M_{\mathrm{vir}} \leq 13.2\ \mathrm{M}_{\odot}$ (blue), and $13.2 < \log M_{\mathrm{vir}} \leq 14.0\ \mathrm{M}_{\odot}$ (red) – separately. The inner and the outer contours of the shaded regions of each colour correspond to 1-σ and 2-σ, while the $\times$ marks the median for all the galaxies within each mass bin. The panels to the left and below the main plots show the normalized marginalized distributions of y-axis redshift (left) and x-axis redshift (below). The different coloured curves show the redshift distributions for the three mass bins and the dashed lines indicate their median:

gas within the circumgalactic region around the galaxies. Most of this material, being extremely metal-rich, cools down and falls back into the galaxy. This is discussed at length in Oppenheimer et al. (2010) and their Figure 2 shows that in galaxies with stellar mass $\gtrsim 4 \times 10^{10}$ $M_{\odot}$, the median time between the launching of a wind particle, and it falling back into the galaxy and is either converted into a star or launched for a second time is $\lesssim$1 Gyr. In effect, the winds power galactic fountain flows rather than galactic outflows and consequently, the $\geq L_*$ galaxies can no longer moderate their star formation rates by depleting their cold gas mass via expulsion. The high cold gas mass in our group central galaxies is a consequence of this, and the overproduction of stars is a byproduct. This is nicely illustrated in Figure 4 of Oppenheimer et al. (2010), which shows that $\gtrsim$70% of the stars in massive galaxies at $z = 0$ have formed out of re-accreted wind material.

There are two potential ways of resolving the above problem: (1) Increase the wind launch velocities so that even in the giant galaxies, the winds are not confined within the circumgalactic regions and when they thermalize, the ejected material heats up to IGrM temperatures. This may help reduce both the cold gas and the stellar masses of the massive galaxies in our simulated groups but at a cost of making the IGrM mass fractions in these groups, and their corresponding X-ray properties, potentially discrepant with the observations, and it will not improve our baryon fraction results. Or, (2) $M_* \approx 4 \times 10^{10}$ $M_{\odot}$ is the transition mass scale where an alternate feedback mechanism, like AGN feedback, must come into play. The main requirement of this alternate feedback mechanism is that it must be sufficiently potent that it, either by itself or in combination with the galaxy-wide stellar powered outflows, can drive down the total baryon fractions and the cold gas mass fractions in giant galaxy or group halos with $M_{500} < 2 \times 10^{14}$ $M_{\odot}$.

3.2.2 Assembly of the Present-day Groups

Having discussed the evolution of various baryonic components comprising the groups in some detail above, we conclude our discussion of the group baryonic properties by considering the five redshifts that encapsulate the key features of the groups' formation histories. To determine these, we reconstructed each present-day group's merger history by stepping back in time from the present and identifying, at each epoch, all the individual halos that are the present-day group's ancestors. We label the largest of these the most massive progenitor (MMP). Our five redshifts are based

on the properties of the MMP. These redshifts are:

$Z_{0.5\ \mathrm{halo}}$: The redshift at which the total mass of a present-day group's MMP is half of the group's final mass;
i.e., $M_{\mathrm{MMP},200}(z) = \frac{1}{2} M_{200}(z)|_{z=0}$.

$Z_{0.5\ \mathrm{IGrM}}$: The redshift at which the hot ($T > 5 \times 10^5$ K) gas mass in the MMP is half of the group's final IGrM mass;
i.e., $M_{\mathrm{MMP,IGrM},200}(z) = \frac{1}{2} M_{\mathrm{IGrM},200}(z)|_{z=0}$.

$Z_{0.5\ \mathrm{star}}$: The redshift at which the total stellar mass in the MMP is half of the group's $z = 0$ total stellar mass; *i.e.,* $M_{\mathrm{MMP,star},200}(z) = \frac{1}{2} M_{\mathrm{star},200}(z)|_{z=0}$.

Z_{group}: The redshift at which the MMP becomes a group and hosts at least three luminous galaxies.
i.e., $N_{\mathrm{MMP,gal}}(z) \geq 3$

$Z_{0.5\ \mathrm{MMP_{gas},IGrM}}$: The redshift when the hot diffuse IGrM mass in the MMP exceeds 50% of the total gas mass.
i.e., $M_{\mathrm{MMP,IGrM},200}(z)/M_{\mathrm{MMP,allgas},200}(z) > 0.5$.

In Figure 3.7, we show the individual distribution of these redshifts as well as the relationship between them. We have chosen $Z_{0.5\ \mathrm{halo}}$, the redshift commonly referred to as the "formation redshift" of the present-day groups, as the common reference for four cross plots. To start with, we consider this redshift by itself first. The bottom panel in each of column of plots shows the normalized distribution of the formation epoch.

The distribution of formation times for groups in all three mass bins are similar and the median formation epoch is $z \approx 0.9$. If the halos populating each of the mass bins were a representative (*i.e.,* unbiased) subset of all the dark matter halos in the simulation volume with masses $12.5 < \log M_{\mathrm{vir}} \leq 13.0$ $\mathrm{M}_\odot$ (low), $13.0 < \log M_{\mathrm{vir}} \leq 13.2$ $\mathrm{M}_\odot$ (intermediate), and $13.2 < \log M_{\mathrm{vir}} \leq 14.0$ $\mathrm{M}_\odot$ (high), we would expect the "low mass halos" to be slightly older than the "intermediate mass halos" and the "high mass halos" to be younger. The groups in the intermediate (median formation redshift is indicated by the blue dashed line) and the high mass bins (median formation redshift is indicated by the red dashed line) conform to these expectations. This is perhaps not surprising. As shown in Figure 2.1, nearly all dark matter halos with masses $M_{\mathrm{vir}} > 10^{13}$ $\mathrm{M}_\odot$ are groups and, therefore the group halos

in the intermediate and the high mass bins form a representative sample. The median formation redshift of the groups in the lowest mass bin (median formation redshift is indicated by the magenta dashed line), however, breaks the expected trend: Their median formation redshift is lower than that of the intermediate mass halos. This is because the group halos that populate the low mass bins are *not* an unbiased sample of all dark matter halos with masses in the range $12.5 < \log M_{\rm vir} \leq 13.0$ $M_\odot$. Rather, these groups form a very special subset with at least three luminous galaxies and as discussed by Zhu et al. (2006), this type of constraint on the galaxy occupation number results in the selection of a relatively younger subset of halos, which is indeed what we find.

The y-axis of the top left panel of Figure 3.7 shows the distribution of $Z_{0.5\,\rm IGrM}$, the epoch when the hot diffuse IGrM mass in the MMP exceeds 50% of the IGrM mass in the final group halo. The redshift distributions for the groups in the three mass bins are very similar. Much more interestingly, the halo formation time and $Z_{0.5\,\rm IGrM}$ are very tightly correlated. This suggests that the MMPs of the present-day groups have already built up a substantial reservoir of hot diffuse gas by the time the group halos form at $Z_{0.5\,\rm halo}$. These results are consistent with the trends seen in Figure 3.5, which show that post-formation, the growth of dark matter mass and IGrM mass proceeds in lock-step.

In the top right panel of Figure 3.7, we show the joint and the marginal distributions of $Z_{0.5\,\rm MMP_{gas},IGrM}$, the redshift when the hot diffuse IGrM begins to dominate the total gas mass in the MMP, and $Z_{0.5\,\rm halo}$. The plot suggests little or no correlation between these two redshifts. However, the normalized distribution of $Z_{0.5\,\rm MMP_{gas},IGrM}$ confirms our earlier assertion that the progenitors of the most massive $z = 0$ groups (red curve) build up a substantial reservoir of hot diffuse X-ray emitting gas fairly early on; the median value of $Z_{0.5\,\rm MMP_{gas},IGrM}$ for these systems is $z = 2.6$. The distribution for the intermediate mass halos is shifted to lower redshifts, with a median of $z = 2$, and the distribution of the lowest mass groups is shifted to lower redshifts, with a median of $z = 1.5$. For the majority of the groups, the gas content of the MMPs is dominated by hot gas well before the MMP mass reaches 50% of the corresponding present-day group's final mass.

In the bottom left panel, we show the joint and the marginal distributions of $Z_{0.5\,\rm star}$, the redshift at which half of the total $z = 0$ stellar mass within R_{200} is in place within the MMP, and $Z_{0.5\,\rm halo}$. The main plot shows that these two redshifts are strongly correlated. During the early phases of group formation, the MMP grows

principally via mergers, which add to both the dark matter mass as well as the stellar mass of the system. However, if the two grow in perfect lock-step, we would expect their joint distribution to define a narrow ellipse whose major axis lies along the $1:1$ line, but they don't and even the median $Z_{0.5\,\mathrm{star}}$ is slightly lower than $Z_{0.5\,\mathrm{halo}}$, with $\Delta z \approx 0.2$–0.3. As discussed previously, the mergers not only contribute stars and dark matter, they also bring in cold gas. In Figure 3.5, we discussed the conversion of this cold gas into stars, especially at late ($z < 1$) times. This *in-situ* star formation breaks the 1-to-1 mapping between halo assembly and the establishment of the stellar mass. As we have noted previously, any additional feedback mechanism that is added to these simulations must be able to prevent the build-up of cold gas in the smaller systems because once this cold gas reservoir is established, it is unlikely that any mechanism acting solely on group or cluster scales can prevent this gas from being delivered to the central galaxies. An additional point of interest is that the median value of $Z_{0.5\,\mathrm{star}}$ indicates that half of the stellar component of today's galaxy groups was already in place about 6 billion years ago.

Finally, the bottom right panel shows the joint and the marginal distributions of $Z_{0.5\,\mathrm{halo}}$ and Z_{group}, the redshift at which one or more luminous galaxies is incorporated within the MMP and it meets our definition of a group. There are two features worth noting. First, the distribution of redshifts at which the MMPs of the present-day groups qualify as "groups" are fairly broad, much broader than the group halo formation times. Second, the MMPs of the high and intermediate mass groups generally acquire a third luminous galaxy well before half of the groups' final mass is assembled. Only in the case of the lowest mass groups do a significant fraction of the halos form first and then become groups. The median Z_{group} for the high, intermediate and low mass are $z = 2.7$, 2 and 1.2, respectively, as compared to the median formation epoch of $z \approx 0.9$ for the same three categories of groups.

3.3 METAL ENRICHMENT OF THE INTRA-GROUP MEDIUM

In addition to altering the thermal and baryonic properties of galaxy groups, large-scale galactic outflows also transport metals from the galaxies to the intergalactic space. Such outflows are key to explaining the widespread enrichment of the intergalactic medium (IGM) as early at $z \sim 5$ (Oppenheimer & Davé, 2006; Oppenheimer,

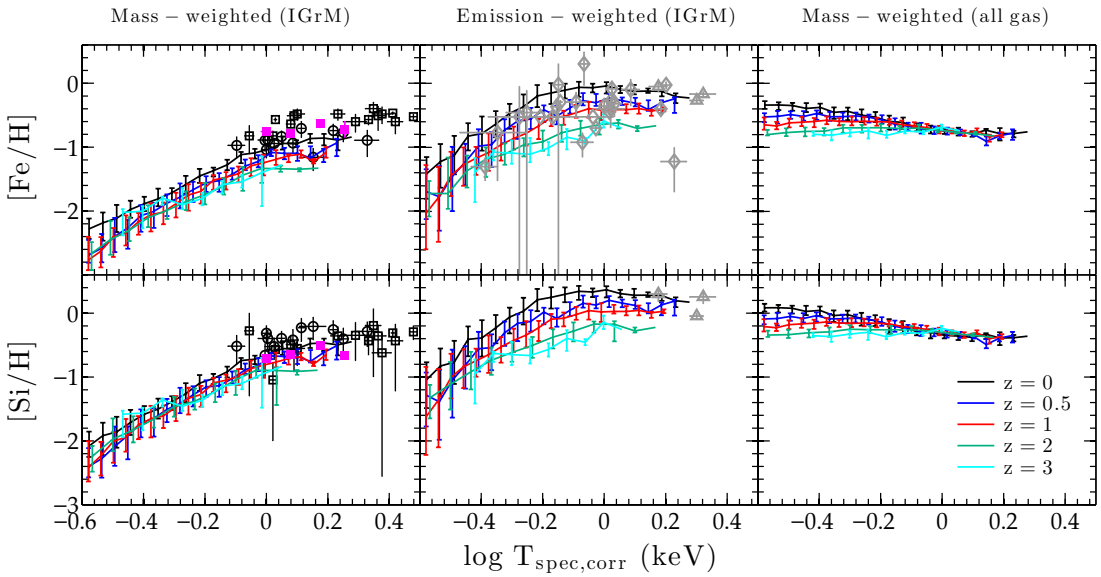

Figure 3.8: Global iron (top row) and silicon (bottom row) abundances within R_{500} of the group centers. The left column shows the mass-weighted abundances in the IGrM; the middle column shows the X-ray emission-weighted abundances in the IGrM; and the right column shows the global mass-weighted abundances of all the gas, including the cold gas within individual group galaxies. The coloured lines and the corresponding error bars show the median values and the 1-σ dispersion for group populations in the simulation volume at $z = 0$ (black), $z = 0.5$ (blue), $z = 1$ (red), $z = 2$ (green) and $z = 3$ (cyan). The open black circles, the open black squares, and the filled magenta squares in the left column show measurements from Rasmussen & Ponman (2009), Fukazawa et al. (1998) and Sasaki, Matsushita & Sato (2014), respectively. The grey diamonds and triangles are results from Helsdon & Ponman (2000) and Peterson et al. (2003), respectively.

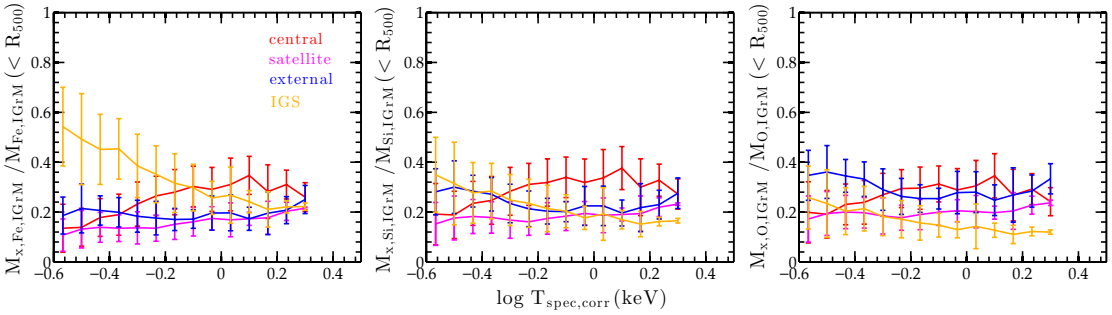

Figure 3.9: The fraction of IGrM iron (left panel), silicon (middle panel) and oxygen (right panel) mass within R_{500} in $z = 0$ groups, characterized by their $T_{\rm spec,corr}$, contributed by the central galaxies (red curve), the group satellite galaxies (magenta curve), the non-group external galaxies (blue curve), and the intragroup stars (orange curve) over cosmic time. See §5.2 for our schema for classifying galaxies as central, satellite or external. The error bars depict 1-σ error.

Davé & Finlator, 2009) and the observed mass-metallicity relation in galaxies, both today and at higher redshifts (Finlator & Davé, 2008; Davé, Finlator & Oppenheimer, 2011b; Hirschmann et al., 2013; Somerville & Davé, 2014). In this section, we focus specifically on the hot, diffuse, X-ray emitting, intragroup medium. The observed iron and silicon abundances ranging from ~ 0.1 to ~ 0.7 solar offers clear evidence that a significant fraction of the metals produced in galaxies escapes from these systems. We determine the level of iron, oxygen and silicon enrichment in the IGrM that can be attained via our momentum-driven outflows model and assess how these compare with the latest observations. We also show how the abundances and abundance ratios evolve with time. And, we discuss how our metal abundances would change if the global stellar mass in our simulated groups were to be reduced by a factor of ~ 2 to reconcile the model results with the observations (*c.f.,* Figure 3.5).

3.3.1 The metallicity of the IGrM

In Figure 3.8, we plot the global mass-weighted (left column) and emission-weighted (middle column) iron and silicon abundances in the IGrM within R_{500} of the simulated groups (top and bottom rows, respectively), as well as the global mass-weighted abundances of all the gas, including the cold gas within individual group galaxies (right column), as a function of core-corrected spectroscopic temperature. The coloured lines show the abundances at different epochs over the redshift range $0 \leq z \leq 3$. The fact that we have chosen to show both mass- and emission-weighted curves may seem

a bit excessive. For the kind of comparisons we wish to carry out, mass-weighted data is preferable. However, the available group observations (for comparison) are limited because spatially resolved, X-ray spectroscopy of galaxy groups, which is a prerequisite for mass-weighted abundance measurements, involves long observations and challenging analyses. On the other hand, there has been a steady reporting of group abundance measurements in the literature over the years but most of this data is emission-weighted. Given such circumstances, we have opted to leverage both types of measurements: In the first column on the left, the black open squares show the core-corrected data from Fukazawa et al. (1998)[7], the open black circles show the results from Rasmussen & Ponman (2007), and the magenta filled squares show the latest *Suzaku* results from Sasaki, Matsushita & Sato (2014). We focus on measurements from "warm" groups, *i.e.,* groups with $T_{\rm spec,corr} \gtrsim 0.8$ keV or $M_{500} \gtrsim 1.7 \times 10^{13}$ $M_{\odot}$, because this data range has been studied by several independent groups and collectively, the measurements are more likely to be representative. In the middle column, we show as grey diamonds the data from Helsdon & Ponman (2000) while the grey triangles show data from Peterson et al. (2003). To facilitate comparison, all metal abundances, whether theoretical or observational, are normalized to the solar "photosphere abundances" level from Anders & Grevesse (1989) (see Section 2.3).

Turning first to the mass-weighted IGrM abundance in warm $z = 0$ simulated groups, we find that [Fe/H] rises gently from -1.2 to -0.9 with temperature and then flattens, while [Si/H] rises from -0.8 to -0.45 and then flattens. The model results are in very good agreement with the observations although there is a hint that the observed iron abundance measurements might be higher by $0.1 - 0.2$ dex. This level of mismatch, if real (note that the latest *Suzaku* results are lower than the earlier *XMM-Newton* or *Chandra* results and hence, much more compatible with the model results), is not unexpected given the factor ~ 2 uncertainties in the adopted nucleosynthesis yields and supernovae rates. The emission-weighted observations and the simulation results are also in agreement; however, this is not surprising given the large scatter in the observational measurements. Interestingly, the emission-weighted silicon and iron IGrM abundances of warm $z = 0$ groups overestimate the "true", *i.e.,* mass-weighted, abundances by 0.6-0.7 dex. This is a consequence of emission-weighted results being biased towards the brighter (in X-ray) central cores

[7] As discussed in Appendix A3 of Nagashima et al. (2005), the core-corrected abundance measurements of each group in Fukazawa et al. (1998) provide a reliable estimate of the global mass-weighted abundance of the groups under consideration.

of the groups, which – if recent observations are a fair guide – are expected to be more metal-rich. We will be examining the metallicity profiles, and other related distributions, of our simulated groups in future work.

In the cooler ($T_{\rm spec,corr} \lesssim 0.8$ keV) simulated groups, the iron and silicon abundances drop with decreasing IGrM temperature. This trend is the consequence of the metal-rich diffuse gas in these systems dropping out of the IGrM more efficiently because, as we have mentioned previously, the gas sits closer to the broad peak in the cooling curve. The total iron and silicon abundances of all the gas, including the cold gas inside group galaxies, within R_{500} are, however, broadly similar across both warm and cool groups (see the right column of Figure 3.8), and at $z = 0$, perhaps even shows evidence of a slight rise towards the coolest groups. This latter trend is not surprising given that the $z = 0$ stellar fraction is the largest in the coolest groups. It is possible that the inclusion of AGN heating as well as turbulent diffusion, which is not included in our present simulation but is expected to play a role in transporting the chemical elements from regions of high metallicity within the IGrM to regions of low metallicity, may moderate the decline in the abundances towards lower temperatures.

The coloured lines in Figure 3.8 show how the abundances grow with time. On the whole, the iron abundance within R_{500} increases by a factor of $\sim 2.5 - 3$ from $z = 2$ to $z = 0$, and the silicon abundance increases by a factor of ~ 2. Both show a similar growth pattern, growing gently between $0.5 < z < 2$ and then somewhat more rapidly between $0 < z < 0.5$, with the iron abundance growing a bit faster than silicon. This late growth is fuelled by the release of metals locked up in AGB stars (iron and silicon) as well as the injection of iron by delayed Type Ia SNe. We will return to this issue when we consider the evolution of the abundance ratios in Section 3.3.3.

3.3.2 Sources of the IGrM Metals

Having compared the metallicity of the IGrM in present-day simulated galaxy groups with available observations, we now examine where the metals in the IGrM originated. We focus on the IGrM within R_{500} and label the potential sites of metal production based on their *status at the time of enrichment* as follows:

Central: The central galaxy of the present-day group or the central galaxy of the group's MMP at an earlier epoch.

Satellite: A non-central galaxy that is contained within the $z = 0$ group halo or within the group's MMP.

External: A galaxy that is neither a central nor a satellite at the time of enrichment.

IGS: Direct enrichment of the IGrM by intragroup stars, *i.e.,* stars in the present-day group or any of its progenitor subhalos that are not bound to any of the skid-identified galaxies

The left, middle and right panels of Figure 3.9 show the contribution of each of these to the total iron, silicon and oxygen mass, respectively, in the IGrM within R_{500} of the present-day simulated groups. The figure shows the results for the full sample of simulated groups: warm and cool. In the following, we will only discuss the warm (*i.e.,* $T_{\rm spec,corr} \gtrsim 0.8$ keV) simulated groups whose metallicity we are able to compare directly with observations.

As illustrated in Figure 3.9, the central galaxy is an important source of all three metal species in the warm groups. This component contributes $\sim 30\%$ of the iron mass, $\sim 32\%$ of the silicon mass, and $\sim 30\%$ of the oxygen mass. In the case of oxygen, the external galaxies contribute about the same fraction, followed by the satellite galaxies, which contribute about 20%. The IGS contribution is approximately 12% and the balance ($\sim 8\%$) comes from 'unresolved' galaxies (*i.e.* SKID-identified galaxies with a total mass in cold gas and stars $< 2.92 \times 10^9$ $M_\odot$; *c.f.,* §2.2). In the case of silicon, the satellites, the externals, and the IGS all contribute about the same amount ($\sim 20\%$) and again, the 'unresolved' galaxies contribute $< 10\%$. Since silicon and oxygen are both α-elements, it may seem surprising that the relative contributions of the four categories to IGrM mass of these two elements are not identical. However, as we elaborate in Section 3.3.3, while the two are produced via the same mechanisms, they are processed differently by AGB stars. For iron, the second most important source in the IGrM, after the central galaxy, is the IGS component. This component contributes the same amount of iron (30%) as the central galaxy in groups with $T_{\rm spec,corr} \approx 0.8$ keV but fraction drops with increasing IGrM temperature to 20% in groups with $T_{\rm spec,corr} \approx 2$ keV. The satellites and the externals both contribute the same amount: $16 - 20\%$, with the unresolved systems making up the rest ($< 10\%$). One important take-away is that the central and the satellite galaxies within the group halo or its MMP (*i.e., in-situ* wind enrichment) produce nearly half of the

total mass of all three metal species in the IGrM and are more important than the low-mass galaxies responsible for the early enrichment of the intergalactic medium.

Knowing where the metals are produced allows us to ascertain the extent to which the estimates of [Fe/H] and [Si/H] that we compare with the observations in Figure 3.8 are affected by the overproduction of stars in the group galaxies. To do so, we have determined how much of the iron and silicon mass in the warm groups originates in galaxies whose stellar mass exceeds 10^{11} $M_{\odot}$ at the time of ejection. In the case of both iron and silicon, approximately 30% of their IGrM mass is ejected from 'super-sized' galaxies. If, as an exercise in post-processing, we assume that some mechanism (*e.g.* AGN heating) quenches star formation in massive galaxies, limiting their stellar mass to a maximum of 10^{11} $M_{\odot}$, then the metals that were ejected of the galaxies after they evolved into 'super-sized' galaxies would either have not been made or would have remained locked up in the galaxies. In this case, the [Fe/H] and [Si/H] of warm groups in Figure 3.8 would decrease by 0.15, or less than space between consecutive tick marks in the plot. The [Si/H] would lie right on top of the *Suzaku* observations while the [Fe/H] would drop below the *Suzaku* results, but still be consistent with the observations given the factor ~ 2 uncertainties in the nucleosynthesis yields and supernovae rates. The main point of this exercise is to demonstrate that the metal abundance results shown in Figure 3.8, and by extension the abundance ratios that we will discuss next, are relatively insensitive to any suppression of star formation in the massive galaxies invoked to bring the overall stellar mass fraction in the groups in alignment with the observations (*c.f.,* Figure 3.5).

3.3.3 Abundance Ratios in the IGrM

In Figure 3.10, we examine the IGrM silicon-to-oxygen (top panel) and silicon-to-iron (bottom panel) abundance ratios within R_{500} for the simulated groups at different epochs. Silicon and oxygen are both α-elements and are produced by core-collapse SNe. As a result, in the absence of any other process, the silicon-to-oxygen abundance ratio would be expected to remain constant over time. The ratio in our simulation, however, increases with time. This is a consequence of silicon and oxygen being processed differently by AGB stars (Oppenheimer & Davé, 2008): When AGB stars form, the silicon and oxygen present in the ISM is locked up in these stars. Over their lifetime, these stars burn some of the oxygen while the silicon remains unaffected. Consequently, when the AGB stars release their metals back into the ISM, the amount

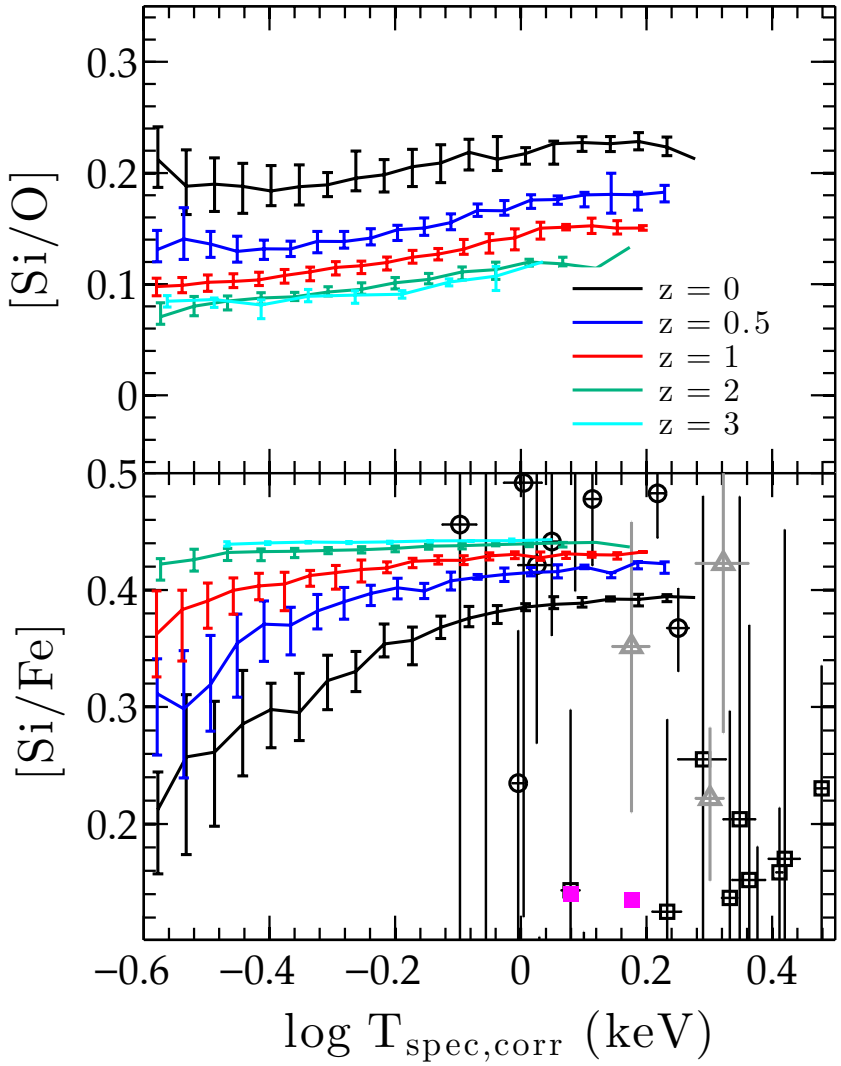

Figure 3.10: Global silicon-to-oxygen (top panel) and silicon-to-iron (bottom panel) abundance ratio within R_{500}. The symbols show data from Rasmussen & Ponman (2009) (open black circles), Fukazawa et al. (1998) (open black squares), Sasaki, Matsushita & Sato (2014) (filled magenta squares), and Peterson et al. (2003) (grey triangles). The coloured lines and the corresponding error bars show the median values and the 1-σ dispersion for group populations in the simulation volume at $z = 0$ (black), $z = 0.5$ (blue), $z = 1$ (red), $z = 2$ (green) and $z = 3$ (cyan). We point out that this y-axis scale is *not* the same as in Figure 3.8. We have deliberately zoomed in to highlight the differences between the curves.

of silicon is nearly the same as that locked up in the first place but the amount of oxygen returned is reduced. The evolution in [Si/O] in Figure 3.10 results from this differential evolution. As for the gentle rise in [Si/O] with increasing group temperature, this is a consequence of the four categories in Figure 3.9 not contributing identically to the silicon and oxygen mass. We emphasize, however, that this increase with group temperature amounts to maximum change of Δ[Si/O]$\approx$ 0.05, which is insignificant. For all intents and purposes, [Si/O] is independent of group temperature or mass.

In contrast, $z = 0$ [Si/Fe] curve (lower panel) not only increases by Δ[Si/Fe]$\approx$ 0.2 in going from the coolest to the warmest groups in our simulation sample, this change evolves from Δ[Si/Fe]$\approx$ 0 at $z = 3$ to its present-day value while the value of [Si/Fe] in the warmest group drops slightly. To zeroth order, the redshift evolution is due to delayed Type Ia SNe spewing new forged and winds from AGB stars spewing previously locked-up iron mass to their local environment. Generally, this environment is the ISM within the group galaxies. However, transporting this 'late' iron out of the galaxies and into the IGrM is not straightforward. As we have noted previously, metal-rich winds from the central galaxies in cool groups tend to behave more like galactic fountains and therefore, very little of the 'late' iron production gets into the IGrM. The central galaxies in the more massive groups are able to drive the iron into the IGrM but they are not outrightly dominant sources because they are running out of cold gas and hence, not forming stars as vigorously. Moreover, because of the size of the galaxies, the mass loading factor of the wind that is ejected is only a fraction of the star formation rate (*c.f.,* Section 2.1) and even in this case, the ejection of the 'late' iron is inefficient. However, winds are not the only way to enrich the IGrM. Direct enrichment by the IGS component is another. And as illustrated in Figure 3.9, the latter is the dominant source of iron mass in the cool groups and also the reason why [Si/Fe] in cool groups evolves much more rapidly than in warm groups.

3.3.4 The Characteristic Timescales for Metal Enrichment of the IGrM

We conclude our investigation of the metal enrichment of the IGrM by examining the redshifts by which half of the iron, silicon and oxygen mass in the $z = 0$ IGrM within R_{200} is produced by the stars, regardless of whether the metals are initially deposited in the ISM or introduced directly into the IGrM. We refer to these characteristic

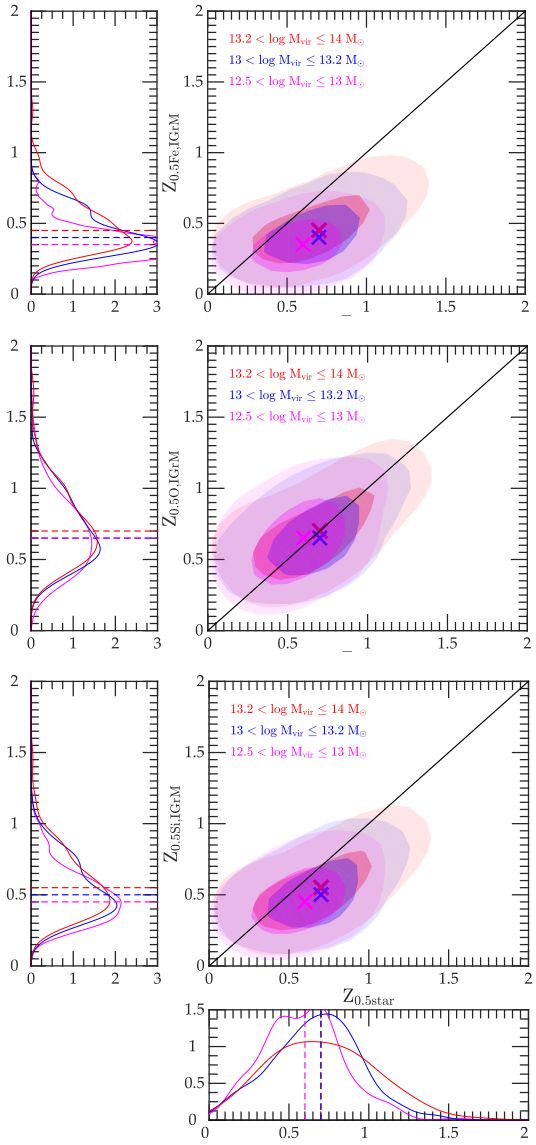

Figure 3.11: The joint distribution of $Z_{0.5\ \mathrm{XX,IGrM}}$, the redshift by which half of the metals of species XX={Fe, O, Si} in a present-day group's IGrM has been *forged* by the stars/supernova, versus $Z_{0.5\ \mathrm{star}}$, the distribution of redshifts by which half of the present-day group's stellar mass has been assembled in its MMP. The contour plots show the 2D distribution of the redshifts for the low, intermediate and high mass groups – *i.e.,* $12.5 < \log\ M_{\mathrm{vir}} \leq 13.0\ \mathrm{M}_{\odot}$ (magenta), $13.0 < \log\ M_{\mathrm{vir}} \leq 13.2\ \mathrm{M}_{\odot}$ (blue), and $13.2 < \log\ M_{\mathrm{vir}} \leq 14.0\ \mathrm{M}_{\odot}$ (red) – separately. The inner and the outer contours of the shaded regions of each colour correspond to 1-σ and 2-σ, while the $\times$ marks the median for the galaxies in each mass bin. The panels to the left and below the contour plots show the normalized marginalized distributions of $Z_{0.5\ \mathrm{XX,IGrM}}$ (left), and $Z_{0.5\ \mathrm{star}}$ (below). The different colour curves show the results for the low, intermediate and high mass groups, and the dashed lines indicate the median.

redshifts as $Z_{0.5\,\mathrm{Fe,IGrM}}$, $Z_{0.5\,\mathrm{O,IGrM}}$ and $Z_{0.5\,\mathrm{Si,IGrM}}$. We show their distributions in Figure 3.11, where we compare them to the redshifts by which half of the group's $z = 0$ stellar mass has been assembled in its MMP ($Z_{0.5\,\mathrm{star}}$). There are several other characteristic redshifts, such as the halo formation redshift ($Z_{0.5\,\mathrm{halo}}$) or the redshift at which the hot ($T > 5 \times 10^5$ K) gas mass in the MMP is half of the group's final IGrM mass ($Z_{0.5\,\mathrm{IGrM}}$), that we have compared $Z_{0.5\,\mathrm{XX,IGrM}}$ (where XX={Fe, O, Si}) against; however, we do not show these because they do not offer any additional insights and Figure 3.7 offers a straightforward map between $Z_{0.5\,\mathrm{star}}$ and the other potential redshifts of interest.

Examining the timescales in detail, the most significant feature is that in all but the most recently formed groups, the characteristic 'metal production' redshifts are lower than $Z_{0.5\,\mathrm{halo}}$ or $Z_{0.5\,\mathrm{IGrM}}$. In other words, typically more than half of the iron, silicon and oxygen in the $z = 0$ IGrM was forged after half of the groups' IGrM was already in place within the nascent groups.

The relationship between $Z_{0.5\,\mathrm{XX,IGrM}}$, where XX={Fe, O, Si} and $Z_{0.5\,\mathrm{star}}$ is more nuanced. In the case of iron (*c.f.,* the top panel of Figure 3.11), the major axis of the contours has a shallower slope relative to the one-to-one line. Since $Z_{0.5\,\mathrm{star}}$ is a measure of when stars first appear inside groups, the orientation of the contours indicates that the iron in the $z = 0$ IGrM is typically made after half of the groups' final stellar mass is in place within the MMP. This is not surprising. As we have discussed previously, AGB stars and delayed Type Ia SNe play a key role in the build-up of iron in the IGrM and there is a lag between the formation of a stellar population and the start of enrichment by Type Ia SNe and AGB stars associated with that population. However, if this was all, we would have expected the width of the contours at fixed $Z_{0.5\,\mathrm{star}}$ to be fairly narrow. Instead, as suggested by the left panel of Figure 3.9, about 20% of the $z = 0$ IGrM iron is forged by the stars/supernovae before the source galaxies become incorporated into groups. In this case, $Z_{0.5\,\mathrm{star}}$ registers the stars in these external galaxies only after they fall in; *i.e.,* if they fall in before $z = 0$, while the metal production is registered whenever it happens.

Turning to the second panel of Figure 3.11, we see that there is more of a one-to-one relationship between the timescale for oxygen production and $Z_{0.5\,\mathrm{star}}$. This alignment is the result of two effects acting in concert: (i) Between 60-70% of the oxygen in the $z = 0$ IGrM is forged by stars that are already in the groups (*c.f.,* the right panel of Figure 3.9), and (ii) oxygen production by core-collapse Type II SNe and transport into the IGrM (by winds) are both tied directly to star formation, with

no significant built-in lag between these events.

Turning to the third panel of Figure 3.11, we find that the orientation of the contours in the $Z_{0.5\ \mathrm{Si,IGrM}} - Z_{0.5\ \mathrm{star}}$ plot is midway between that of iron and oxygen. As discussed in the previous subsection, although silicon and oxygen are both produced in an identical manner, there is one significant difference. AGB stars capture and retain a non-negligible amount of silicon present in the ISM at the time their progenitor stars form, and return it to their surroundings only after a lag time. In effect, this means that silicon enrichment of the IGrM can proceed via two channels: the galactic wind and, as is the case with iron, via direct enrichment by the AGB stars in the IGS. This late-time injection of silicon differentiates the evolution of silicon from that of oxygen and shifts the distribution of $Z_{0.5\ \mathrm{Si,IGrM}}$ slightly towards lower redshifts with respect to the distribution of $Z_{0.5\ \mathrm{O,IGrM}}$.

3.4 SUMMARY AND CONCLUSIONS

There is a growing consensus that models of galaxy evolution – or for that matter, models describing the formation and evolution of galaxy groups and clusters – that do not allow for large-scale galactic outflows will fail to match the global evolutionary properties of galaxies. Observations of both local as well as high-redshift galaxies indicate that not only are large-scale galactic outflows ubiquitous, but that they have a profound impact on the conditions inside the galaxies as well as conditions in the wider environment around galaxies. For example, galactic outflows are thought to play a central role in establishing the observed mass-metallicity relation in galaxies, in promoting widespread enrichment of the IGM as far back as $z \sim 5$, and in accounting for the abundances and abundance ratios of α and iron-group elements observed in the hot diffuse X-ray emitting gas in galaxy groups and clusters. Recent observations as well as theoretical models indicate that AGNs and stars/SNe are both capable of driving powerful outflows and while definitive observational evidence outrightly favouring one over the other remains elusive, we argue that only stellar processes are capable of driving large-scale galactic outflows that can transport a significant fraction of the metal-enriched ISM out of the galaxies and into their halos and beyond.

Our main findings are as follows:

(i) The distribution of the groups' formation epochs can be reasonably approximated by a Gaussian with a median of $z \sim 1$ and $\sigma = 0.4$. Moreover, the epoch when half of a present-day group's X-ray emitting, intragroup medium (*i.e.* the diffuse halo

gas with $T > 5 \times 10^5$ K) is in place is tightly correlated with the group's formation epoch. Examining the emergence of the latter in more detail, we find that in halos with gravitational potential wells of a given depth, the median IGrM mass fraction increases with time prior to $z \approx 1$ as the halos recapture the gas that was expelled out of the galaxy-scale halos at earlier epochs, (the ratio of baryons-to-dark matter of the infalling material is larger than the universal value) and most of these baryons are shock-heated to roughly the virial temperature of the groups upon accretion. After $z \approx 1$, the IGrM fractions within R_{200} cease to increase with time because the IGrM is sufficiently extended that the newly accreted (and thermalized) baryons primarily remain at $r > R_{200}$ and become part of this extended halo gas distribution. Apart from this trend with time, the IGrM mass fractions within R_{200} also increase with halo mass at all epochs. This increase is the result of the larger mass systems having deeper potential wells and higher virial temperatures. Consequently, more of the diffuse gas is shock-heated to constitute the IGrM and the deeper potentials confine this gas more effectively.

(ii) Our stellar-powered, momentum-driven wind model yields X-ray scaling relations that are in excellent agreement with observed scaling relations (*e.g.* X-ray luminosity-temperature, mass-temperature, entropy-temperature, etc.) over much of the regime associated with galaxy groups despite the fact that the model does not include AGN feedback. These scaling relations evolve self-similarly from $z = 1$ to the present, as does $M_{\rm IGrM,200}/M_{200}$ versus M_{200}. The hot, diffuse, X-ray emitting, intragroup gas is not subject to catastrophic cooling. Typically only a percent or less of $z = 0$ IGrM mass is lost via cooling over a Hubble time. We do, however, see a tendency for the simulated galaxy groups to be slightly more X-ray luminous and/or have slightly cooler X-ray spectroscopic temperature than the observed groups on mass scales $M_{500}E(z) \gtrsim 10^{14}$ M$_\odot$. At face value, these results collectively suggest that AGN feedback is not necessary to understand the properties of the hot diffuse gas in the simulated groups until the halos approach cluster-scale.

(iii) Our simulation also successfully reproduces both the observed, spatially resolved, mass-weighted as well as the observed, unresolved, emission-weighted IGrM silicon and iron abundances within R_{500}. This agreement also includes the observed trend of [Fe/H] and [Si/H] increasing with temperature until ~ 1 keV and then flattening. Probing the origin of the metals in the IGrM in more details, we find that nearly 50% of the IGrM silicon, oxygen and iron mass in our simulated groups are

produced in the central and the satellite galaxies of a present-day group or its MMP, and infused into the IGrM via galactic outflows, while between $\sim 12\%$ (oxygen) to $\sim 30\%$ (iron) is transferred to the IGrM via direct enrichment by the IGS.

(iv) Turning our attention to the group galaxies, we find that the stellar-powered, momentum-driven wind model results in a present-day stellar mass function for group galaxies that is in excellent agreement with the observations for $M_* < 10^{11}$ $M_\odot$; however, we also find galaxies – typically, one per group and invariably, the group central galaxy – that have much larger stellar masses than any observed galaxy. These are the galaxies that are responsible for the elevated stellar and total baryonic mass fractions in our simulated groups. Artificially reducing the stellar mass in only these 'large' galaxies by a factor of ~ 3 reconciles the group stellar mass fractions with the observations across the entire mass range $12.5 \leq \log(M_*) \leq 14.0$.

(v) The excess stellar mass in these 'large' group galaxies is due to galaxies no longer being able to moderate their star formation rates by depleting their cold gas mass via expulsion once they grow larger than $M_* \approx 4 \times 10^{10}$ $M_\odot$. The deepening gravitational potential of these galaxies and a higher cross-section for hydrodynamic interactions between the galactic outflows and the shock-heated halo gas component, once the latter starts to form, confine the wind material within the circumgalactic region. Being metal-rich, most of this wind material cools down and falls back into the galaxy in a manner more akin to galactic fountains rather than outflows (*c.f.,* Oppenheimer et al., 2010). The high cold gas mass in our group central galaxies is largely a consequence of this, and the overproduction of stars is a byproduct. The breakdown of the stellar-powered winds model in our giant group galaxies generally occurs *before* the galaxies are incorporated into bonafide groups and is the earliest indication that another feedback mechanism, like AGN feedback, is needed.

(vi) We assert that in large galaxies, at least, AGN feedback cannot simply act to heat the halo gas just enough to offset the radiative cooling losses. This maintenance-mode or hot halo quenching feedback may represent a reasonable description of how AGN feedback operates in galaxy clusters and may even result in 'large' galaxies with realistic stellar properties (*c.f.,* Gabor & Davé, 2012, 2015, and references therein), but because this type of feedback is, in effect, only shifting baryons in our simulated groups from the galaxies to the IGrM component, the total baryon fraction of the groups will not change. Our simulated groups, however, already have too high a

baryon fraction (*c.f.,* Figure 3.5). At the same time, the IGrM mass fractions will become more discrepant and a denser IGrM means that the simulated groups of a given mass will be more X-ray luminous than their observed counterparts. To ensure that both the stellar masses of the 'large' galaxies and the hot gas properties of the groups agree with observations, AGN feedback (or for that matter, any new feedback mechanism or combination of mechanisms) must step in when stellar feedback starts to fail and continue to drive outflows beyond the galactic halos and perhaps even, beyond the low mass group halos.

(vii) Finally, we emphasize that we do not expect the inclusion of AGN feedback, and the expected reduction in the stellar mass within the groups, to alter the agreement between our simulation results and the observed IGrM metal abundances (and abundance ratios) in galaxy groups. Even after discounting the metals produced by 2/3 of the stars in the 'over-sized' galaxies, the absolute abundances in the simulation are still consistent with the observations, especially when one accounts for the factor $\sim$2 uncertainty in the adopted nucleosynthesis yields and supernova rates.

Chapter 4

THE ENRICHMENT OF THE IGRM - HOW? WHERE? WHEN?

In this chapter, we focus specifically on how the enrichment of the IGrM proceeds. In Section 4.1, we describe the present-day IGrM metal abundance profiles in the simulated groups, compare these to observations, and examine how these profiles have evolved over cosmic time. In Section 4.2, we explore where and when the IGrM metals at different radii of today's groups were forged by the stars/supernovae, and when and where these metals entered the hot gas phase. We also identify the sources of these metals and their relative contributions. And finally, we discuss and summarize our findings in Section 4.3.

4.1 Radial profiles

As noted in the Introduction, the metal content in the IGrM represents a record of the various astrophysical processes associated with the formation and evolution of galaxies in the dense group and cluster environments. In Chapter 3, we computed the mean mass-weighted IGrM iron ($Z_{\rm Fe}$) and silicon ($Z_{\rm Si}$) abundances within R_{500} of simulated $z = 0$ groups with core-corrected spectroscopic temperatures ranging from 0.25 keV to 2.25 keV, and compared these to available observations. We find that the amplitude and the scaling of $Z_{\rm Fe}$ and $Z_{\rm Si}$ with $T_{\rm spec,corr}$ in both the simulated and observed groups are in very good agreement with each other (*c.f.,* Figure 11 of Chapter 3). Specifically, we find that both $Z_{\rm Fe}$ and $Z_{\rm Si}$ rise steeply with temperature for systems with $T_{\rm spec,corr} \lesssim 1$ keV and then flatten. In this section, we explore the

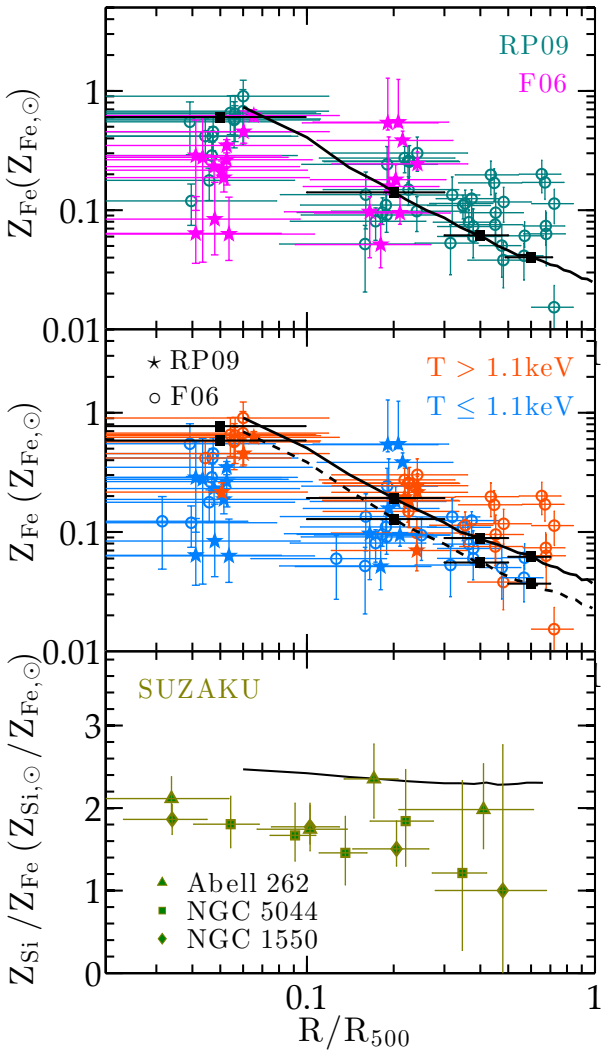

Figure 4.1: Top panel: IGrM gas mass-weighted radial abundance profile for the simulated z = 0 group (black line) and the corresponding mean abundances within radial shells (black points−the horizontal bars indicate the radial extent of the shells). The filled stars and open circles show observational data from Finlator et al. (2006); Finoguenov et al. (2007) and Rasmussen & Ponman (2009), respectively. Middle panel: Same as above except the observations for the "warm" ($T_{\rm spec,corr} > 1.1$ keV) and the "cool" ($0.5 < T_{\rm spec,corr} \leq 1.1$ keV) groups are plotted as red and blue symbols, respectively. The solid (dashed) black line and points show the simulation results for the warm (cool) systems. Bottom panel: The radial silicon-to-iron ratio. The solid line is the simulation result. The olive triangles, diamonds and squares show *Suzaku* measurements for Abell 262 (Schmidt et al., 2009), NGC 5044 (Knobel et al., 2009) and NGC 1550 (Sato et al., 2010), respectively.

spatial distribution of $Z_{\rm Fe}$, $Z_{\rm Si}$ and $Z_{\rm O}$ within the simulated $z = 0$ groups, and compare these with the observations. We then describe how these abundance profiles have evolved over time.

4.1.1 Abundance Profiles at present

The top panel of Figure 4.1 shows the mean mass-weighted spherically-averaged, radial profile of the mass-weighted radial IGrM iron abundance, $Z_{\rm Fe}(r)$, in the simulated $z = 0$ groups with $T_{\rm spec,corr} > 0.5$ keV (black line), and the mean abundances within radial shells (black points) at different distances from the group centres, scaled by R_{500} ($z = 0$). The latter not only facilitates the stacking of the simulated groups but also comparison with the observations. The width of the horizontal "error bars" indicates the size of radial bins within which the mean abundances are determined. Filled magenta stars and green circles are observational results for the mean mass-weighted $Z_{\rm Fe}$ in radial shells from Finlator et al. (2006); Finoguenov et al. (2007) and Rasmussen & Ponman (2009), respectively. We have scaled the radius of the shells for observed groups to R_{500} derived from the $R_{500} - T_{\rm spec,corr}$ relationship for the simulated groups.

The large scatter in the data notwithstanding, the observed $Z_{\rm Fe}(r)$ declines from the value of $\sim 0.3 Z_{\odot}$ in the innermost bins ($r < 0.1 R_{500}$) to just under $\sim 0.1 Z_{\odot}$ at $\sim 0.7 R_{500}$. Overall, the simulation abundance profile is in reasonably good agreement with the observations, especially the more recent Rasmussen & Ponman (2009) data. In detail, the simulation profile is a bit steeper than the observed profile. One reason for this is that the catalog of simulated groups is much more skewed towards lower temperature groups compared to the observational samples, and the lower temperature simulated groups tend to be more metal rich in the central regions than observed groups of comparable temperatures. This is illustrated in the middle panel where, following Rasmussen & Ponman (2009), we show the same observations as in the top panel but color-coded so that the results for the "warm" groups ($T_{\rm spec,corr} > 1.1$ keV) are shown in red, and those for the "cool" groups ($0.5 < T_{\rm spec,corr} \leq 1.1$ keV) are in blue. The results for the "warm" and "cool" simulated groups are illustrated by the solid and dashed black lines and points, respectively. The simulation and observational results for the warm groups are in very good agreement, although one can argue that the innermost regions of even the "warm" simulated groups are slightly more metal rich. In the case of the "cool" groups, the difference in the metallicity

in the innermost shell grows to a factor of ~ 2. This central iron excess, restricted as it is to a small fraction of the volume, does not impact the global $Z_{\rm Fe}$ within R_{500} (*c.f.,* Chapter 3).

The elevated IGrM abundance in the central regions of the simulated groups is directly linked to the star formation in the central galaxies in the groups. In Section 4.2 of the present paper, we examine when and where the metals at different radii in the present-day groups come from and show that metals in the IGrM in the central regions primarily originate in the central galaxies (*c.f.,* Figure 4.3). In Chapter 3, we showed that the current simulation results in these central galaxies having too many stars. Squelching star formation through the introduction of additional mechanisms, like AGN feedback, should lower the abundances in group centres. Moreover, any radial transport of metals from the group centre to larger radii, even if not a dramatic effect, by turbulence and bulk motions induced by AGN-powered outflows, and by drifts and wakes associated with buoyantly rising, AGN-inflated bubbles (*c.f.* Pope et al. 2010 for a theoretical discussion of bubble wakes and drifts, McNamara et al. 2014 and Russell et al. 2014 for potential observational evidence for mass uplift and Revaz, Combes & Salomé 2008 for related numerical simulations) will tend to make the IGrM abundance profile slightly less steep (*c.f.,* McCarthy et al., 2010) and further improve the agreement between the simulation results and the observations. We expect these effects to be more pronounced in groups with shallower potential wells.

In the bottom panel, we compare the radial profile of the mean mass-weighted silicon-to-iron ratio ($Z_{\rm Si}/Z_{\rm Fe}$) for the simulated $z = 0$ groups (black line) with the *Suzaku* measurements (olive symbols) for Abell 262 (Schmidt et al., 2009), NGC 5044 (Knobel et al., 2009) and NGC 1550 (Sato et al., 2010). The silicon-to-iron ratio in both the observed and the simulated groups is largely flat from the group centre out to R_{500} although on closer examination both exhibit a very gentle drop with increasing radius. The two are, however, offset from each other such that the ratio in the simulated groups is $\sim 30\%$ larger. Focusing first on the gradient with radius, the slightly elevated $Z_{\rm Si}/Z_{\rm Fe}$ in the central region occurs because of a mild drop in the IGrM iron mass there relative to the other metals. Iron is an efficient coolant and gas that is rich in iron tends to cool and drop out of the IGrM phase on a slightly shorter timescale. As for the offset, there are potentially three ways of adjusting the simulation parameters to resolve this discrepancy: Reduce the Type II SNe silicon yield; increase the production of iron through a higher Type Ia SNe rate; raise the Type Ia/II iron yields; or some combination thereof. We don't think that reducing

the silicon yield (alone) is the solution. We showed in Chapter 3 that although $Z_{\rm Si}$ within R_{500} in the simulated groups is in agreement with the observations. It is, in detail, slighly on the low side. If the silicon yield in the simulations were to be reduced, the spread between the observations and the simulated results would grow larger. Our comparison favours a slightly larger silicon yield than the one used in the simulations. On the other hand, if the iron production were to increase, not only would the agreement between the simulation results for the global $Z_{\rm Fe}$ within R_{500} and the observations improve (*c.f.,* Chapter 3), the simulated and observed silicon-to-iron ratio would also come into better agreement. Given that even for a fixed IMF, there is still a factor of ~ 2 uncertainty in the nucleosynthesis yields and supernova rates, it is not inconceivable that the correct yields and rates could result in a $\sim 30\%$ more iron mass in the IGrM.

4.1.2 The evolution of metal profiles

Next we examine how the metal distribution in the IGrM evolves over cosmic time. In the top panel of Figure 4.2, we show the mean spherically-averaged radial profiles of the mass-weighted iron abundance in the IGrM of the simulated groups with $T_{\rm spec,corr} > 0.5$ keV at selected redshifts $0 \leq z \leq 3$. We have omitted similar plots for silicon and oxygen because to first order, the shapes of the corresponding abundance profiles at the redshifts under consideration are similar to those of iron. Specifically, the abundance profiles of all three elements at the earliest time shown ($z = 3$) indicate an enhancement in the inner $0.3R_{500}$ and a long flattened plateau (corresponding to $Z_{\rm Fe} \approx 0.02 Z_{\rm Fe,\odot}$ for iron) that extends past $4R_{500}$ ($\approx 2R_{\rm vir}$). The latter is the result of the winds from the early galaxies in the proto-group regions expelling a significant fraction of their metal-enriched ISM over regions extending well beyond R_{200} of the $z = 3$ groups. We have shown in Chapter 3 that these powerful early outflows also lead to the significant reduction ($\sim 75\%$) of the baryonic mass fraction within $6R_{500}$ ($\approx 3R_{\rm vir}$), with respect to the cosmic mean value, in the early groups at $z = 3$ as well as elevate the metallicity of the affected intergalactic gas. The central enhancement is due to the outflows from groups' central galaxies.

Between $z = 3$ and $z = 1$, the abundance profiles interior to R_{500} ($\approx 0.5R_{\rm vir}$) steepen and the amplitude of the extended tail declines. We note that this period is also characterized by the growth of the groups' baryonic mass fraction, from $\sim 75\%$ to $\sim 90\%$ of the cosmic mean (*c.f.,* Chapter 3). The above two trends are due to the

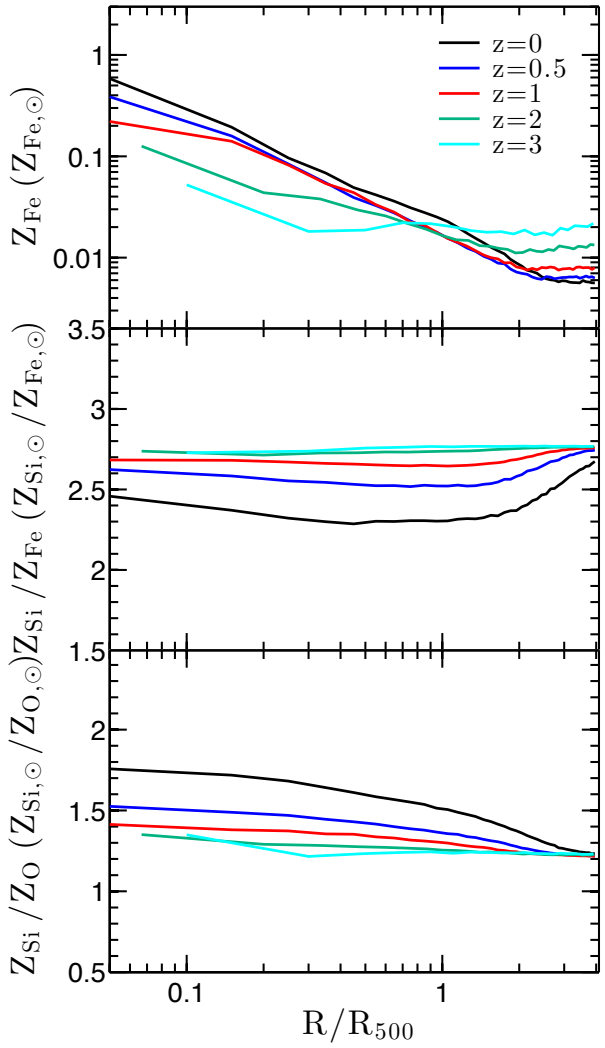

Figure 4.2: Mass-weighted radial profiles of the IGrM iron (top panel) abundance, silicon-to-iron ratio (middle panel), and silicon-to-oxygen (bottom panel) of the simulated groups at $z = 0$ (black), $z = 0.5$ (blue), $z = 1$ (red), $z = 2$ (green) and $z = 3$ (cyan).

same evolutionary processes: (1) The previously expelled metal-enriched material is re-accreted by the growing groups and the gas on successively larger scales is replaced by less enriched intergalactic medium, and (2) the newly expelled gas from the group galaxies is confined to a decreasing fraction of $R_{\rm vir}(z)$, with the intra-group spatial gradient arising due to the groups' central galaxies dominating the enrichment of the inner regions.

Below $z \approx 1$, the abundance profiles continue to steepen, but at a slower rate. This is, in part, because a significant fraction of the previously expelled metal-enriched gas by the early galaxies has been (re)incorporated into the groups; in part, because declining star formation in the central galaxies results in reduced outflows; and, in part, because the cooling of the metal-rich, dense gas in the central regions of the groups become sufficiently rapid that it partially counteracts the enrichment of the IGrM due to the winds from the central galaxies and the intra-group stars. (Note that this does not contradict with the statement in Chapter 3 that only a few per cent of the hot IGrM is lost due to cooling over cosmic time in that the limited amount of cooled IGrM is highly-enriched and therefore metal loss from the IGrM is significant.)

In detail, there are in fact differences in how the metal abundances of different metal species evolve. In the middle and the bottom panels of Figure 4.2, we show the mean radial profiles of the silicon-to-iron ($Z_{\rm Si}/Z_{\rm Fe}$) and the silicon-to-oxygen ($Z_{\rm Si}/Z_{\rm O}$) mass ratios, respectively, in the IGrM of simulated groups at various redshifts. Prior to $z \sim 2$, both the $Z_{\rm Si}/Z_{\rm Fe}$ and $Z_{\rm Si}/Z_{\rm O}$ profiles primarily reflect the yield ratios and relative rates of the Type II SNe and the prompt component of the Type Ia SNe. At lower redshifts, the metals from the delayed Type Ia SNe and the AGB stars become increasingly important. The silicon-to-iron ratio, for example, declines from 2.75 solar at $z > 2$ to $2.3 - 2.4$ solar. This drop is entirely caused by the increase in the iron mass due to the delayed Type Ia SNe. Moreover, since the Type Ia SNe produce negligible amount of silicon, the magnitude of the change implies that the delayed Type Ia SNe are responsible for $\sim 15\%$ of the total iron in the present-day IGrM. The AGB stars do not alter the abundance of iron or silicon.

The evolution of $Z_{\rm Si}/Z_{\rm O}$, on the other hand, is entirely due to the AGB stars. While these neither produce nor destroy silicon, the same is not true of oxygen. They both produce and destroy oxygen, with the overall effect being a net decrease in the oxygen mass. Consequently, the mass ejected from the AGB stars has a higher silicon-to-oxygen ratio than that of the gas from which the AGB stars were formed (see OD08). The late time increase in the IGrM $Z_{\rm Si}/Z_{\rm O}$ is the direct consequence of

this.

4.2 Dissecting the enrichment of the IGrM

Having established how the IGrM metal abundances grow with time, we now investigate in detail how this enrichment occurs. We determine the extent to which the various sources of the metals — the central galaxy, the satellite galaxies, the external galaxies and the intra-group stars (IGS) — contribute to the metallicity at different radii within the present-day group halos, and establish when and where the metals are forged by the stars/supernovae and injected into the IGrM. The approach described here is based on the approach used by Crain et al. (2013) to investigate the enrichment of the hot/warm gas that cocoons the galaxies.

4.2.1 The origin of the IGrM metals

Our simulation generates approximately 60 outputs ("snapshots") spanning the redshift range from $z = 10$ to $z = 0$, and information, such as position, velocity, metal abundances (for SPH and stellar particles) and etc, of all SPH+stellar+dark matter particles in the simulation is recorded at every snapshot. We select the IGrM particles of the simulated $z = 0$ groups and track them back in time using the unique ID assigned to each particle in the simulation. For a given gas particle, if there is metal mass increment between two successive snapshots, we flagged the particle as having been enriched. Like what we have done in Chapter 3, based on the status of the particle *at the time of enrichment*, we identify the potential site of metal production as follows:

Central: The central galaxy of the present-day group or the central galaxy of the group's most massive progenitor (MMP) at an earlier epoch.

Satellite: A non-central galaxy that is contained within the $z = 0$ group halo or within the group's MMP.

External: A galaxy that is neither a central nor a satellite at the time of enrichment.

IGS: Direct enrichment of the IGrM by intra-group stars (*i.e.,* stars in the present-day group or any of its progenitor subhalos that are not bound to any of the skid-identified galaxies) as well as the enrichment associated with the unresolved galaxies (*i.e.,* $M_{\rm tot} \lesssim 2.9 \times 10^9\ M_\odot$). [1]

We construct each group halo's merger history using its dark matter particles and at each point in time, and identify the most massive halo in tree as the MMP. Within each group, the most bound galaxy (*i.e.,* the galaxy that has the lowest total gravitational potential energy, accounting for both self-gravity as well as the gravity exerted by all the baryonic+dark matter within the simulation volume) is said to be the *central galaxy* of the group and likewise, we define the most bound galaxy within the MMP.

We note that since we only save a finite number of simulation outputs, the precise moment of enrichment will not correspond to the redshifts of the recorded snapshots. We therefore identify the enrichment environment based on the location of the gas particles at the two consecutive snapshots that bracket the enrichment event. Specifically, if at either one of the two snapshots, a gas particle is associated with a galaxy, we assume that that galaxy is responsible for the enrichment. On rare occasions, a gas particle may be associated with two different galaxies in the two snapshots. Such cases arise when two galaxies merge during intervening time. In these instances, we assign the enrichment to the snapshot with the more massive galaxy. This is different from the approach adopted by Crain et al. (2013), who classify enrichment events based only on the snapshot preceeding the enrichment event, because we also want to apply tight constraint on the enrichment associated with the IGS component, which Crain et al. (2013) do not explicitly account for in their study on the circum-galactic medium. In our study, we assume the enriched gas particles that have no galaxy ID at either of the two bounding snapshots to be enriched by the IGS.[2] We also note that the sampling in our post-run analysis is sufficient for the classification of the en-

[1] In this chapter, we define the IGS in a slightly different manner compared to what we have done in Chapter 3, such that the IGS here includes the stars that are bound to the unresolved galaxies. The new definition is valid in that the boundary between these unresolved objects and the real field stars is intrinsically ambiguous, and also they contribute very limited amount of metals to the IGrM within R_{500}.

[2] We also exclude the enrichment events that meet this criteria but where the enriched gas particle is identified as wind between the two consecutive snapshots bracketing the event. We associate these particles as having been enriched by the "galaxies" identified by the in-situ finder but not by the post-run finder. We find that the metal mass associated with these wind particles only accounts for $\sim 5\%$ of the total metal mass linked to the "IGS" category by the initial criteria.

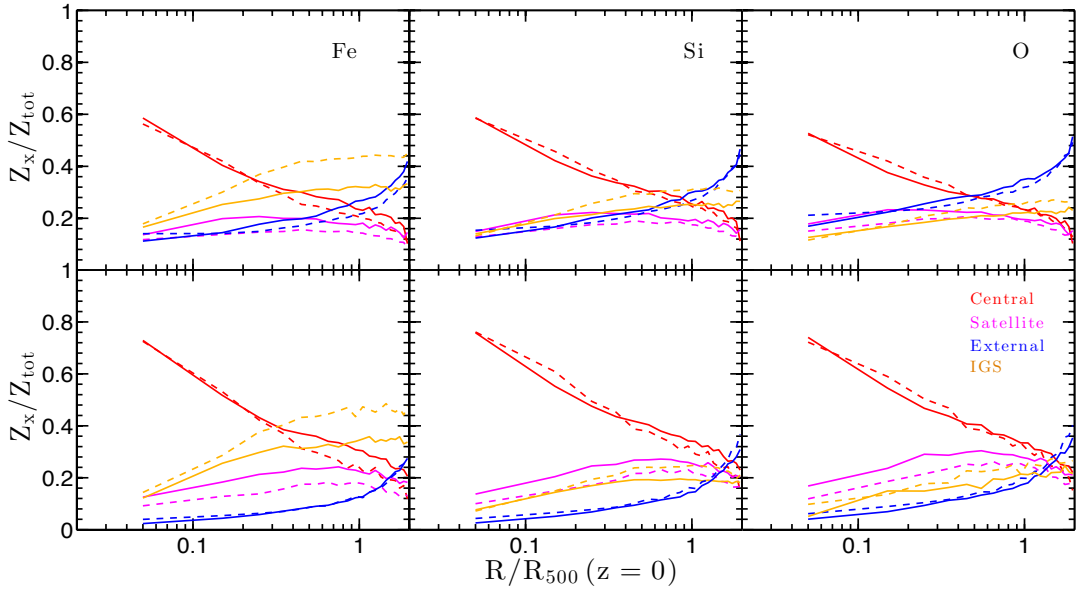

Figure 4.3: Top panels: Mass fraction of the metals in the present-day IGrM contributed by various enrichment sources: central (red), satellite (magenta), and external galaxies (blue), as well as the IGS (orange), as a function of the present-day distance of the metals from the group centre. The left, middle and right panels show the results for the three different metal species. Bottom panels: The classification of the enrichment is different from that used by the top panels, in the sense that for those metals that were ejected from a galaxy, it is based on the site of the most recent ejection. The solid and the dashed lines represent results for the warm and cool groups, respectively.

richment sources since our results do not change significantly even when our tracing algorithm uses only every second snapshot. We ignore the tiny fraction of the metals synthesized before $z = 10$.

In the top panels of Figure 4.3, we show the radial profiles for the fractional contribution by each of the four enrichment sources to the total iron (left), silicon (middle) and oxygen (right) mass in the IGrM of the present-day groups. The results for the warm and cool groups are explicitly shown by the solid and the dashed curves, respectively. Also in Figure 4.4, we show the integrated fractional contribution by the various sources over three radial bins: $0 \leq r < 0.1R_{500}$ (left column), $0.1R_{500} \leq r < R_{500}$ (middle column), and $R_{500} \leq r < 1.5R_{500}$ (right column). The odd and even rows of the pie charts correspond to the results for the the warm and cool groups, respectively. We will at first describe the general features for the entire group

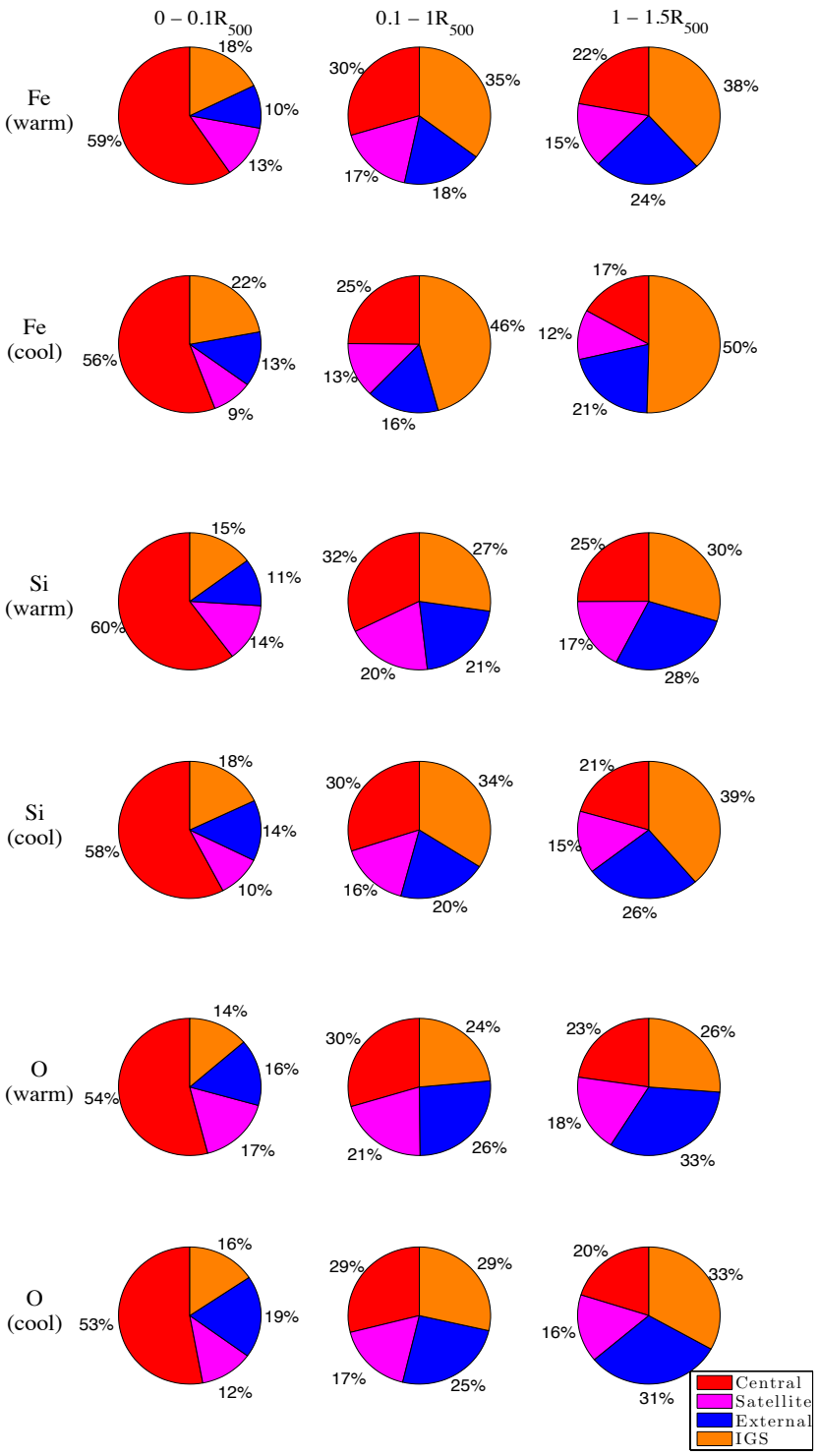

Figure 4.4: The metal budget of the present-day IGrM within different radial bins: $0-0.1R_{500}$ (left column), $0.1-1R_{500}$ (middle column), and $1-1.5R_{500}$ (right column), split by various enrichment environments: central galaxies (red), satellite galaxies (magenta), external galaxies (blue) and IGS. The results for the three different metal elements and the warm and cool groups are separately shown as labelled.

population and then turn to the difference between the warm and cool groups.

Focusing at first on the galaxy-associated categories (*i.e.,* "Central", "Satellite" and "External") in the top panels, it is apparent that the "Central" category (red) dominates the enrichment of the IGrM over any of the other two from the group centre out to $\sim R_{500}$ ($\sim 0.8-1R_{500}$ for the iron and silicon and $\sim 0.5-0.6R_{500}$ for the oxygen), beyond which the "External" category (blue) becomes dominant. The "Satellite" category (magenta) plays an important but sub-dominant role, accounting for nearly constant $10\%-20\%$ of the total metal mass over $0-2R_{500}$. The variation of the fractional contributions with $r(z=0)$ is also clearly demonstrated by the pie charts in Figure 4.4: In both warm and cool groups and for all three metal species, the central galaxies in the groups and their MMPs dominate over the satellite and external galaxies for the two inner radial bins, whereas for the other bin, the external galaxies are the most important contributors.

Comparing the enrichment style between the three different elements, it can be seen that the *relative* contribution to the iron and silicon in the IGrM by the three galaxy-related categories is very similar (The ratio between the three categories is observed to be similar by comparing the corresponding pie charts in the first two and the middle two rows in Figure 4.4). This is because in our simulation, the enrichment that takes place in the dense star forming regions within the galaxies is dominated by the combined yields from the Type II SNe and the prompt Type Ia SNe (the rate of both being scaled to the SFR), whereas the delayed Type Ia SNe (their rate being scaled to stellar mass) contribute a smaller fraction, and hence the iron-to-silicon ratio of the galaxy-associated enrichment is not sensitive to the stellar populations (galaxy types). Were it not for processing by the AGB stars, we would expect the oxygen to shows the same trend. However, there is hint that the "Central" ("External") category plays relatively less (more) important role in oxygen production compared with the iron or silicon: The ratio of the "Central" ("External") to the "Satellite" for the iron within $0.1R_{500}$ in the warm groups (top left pie chart) is $\frac{59\%}{13\%}=4.54$ ($\frac{13\%}{10\%}=0.77$), while for the oxygen within the same radial bin (the left of the fifth row), $\frac{54\%}{17\%}=3.18$ ($\frac{16\%}{17\%}=0.94$). This indicates that the ISM of the central (external) galaxies is more (less) subject to the AGB processing, in the sense that a larger (smaller) fraction of the oxygen mass was burned through the AGB stars. This is not surprising, as the ISM in the more massive galaxies is "chemically older", in the sense that the ISM has been subject to more frequent recycling as a result of these galaxies having deeper gravitational wells and because their circumgalactic

environment consists a dense gaseous halo (*c.f.,* Oppenheimer et al., 2010, Liang et al. 2015). Therefore, the gas enriched within the relatively more massive central galaxies is characterized by a lower oxygen-to-iron ratio than that associated with the satellites, whereas the gas enriched within the relatively less massive external galaxies exhibits a higher ratio.

Turning to the "IGS" category (orange), we find that the diffuse, unbound stars are important contributors of iron to the present-day IGrM. The "IGS" category is expected to be characterized by lower α-to-iron ratio than the galaxy-related categories since there is no ongoing star formation in the intra-group environments and the enrichment associated with the field stars should be primarily due to the metals from the delayed Type Ia SNe and the AGB stars. Indeed, we do see from the top three panels of Figure 4.3 as well as in Figure 4.4 that the "IGS" category accounts for a relatively smaller fraction of the α-element (silicon and oxygen) mass in the IGrM than the iron mass. The silicon and oxygen yields for the Type Ia SNe are almost negligible in our cosmic chemical model, and any contribution to these two elements by the "IGS" category should be primarily due to the mass loss from the AGB stars in the field. The metallicity of the wind from the AGB stars is that of the progenitor ISM from which they were spawned, modified by any processing that occurs in the stars during their lifetime. Specifically, oxygen burning within the AGB stars results in a lower fractional return of the oxygen mass in comparison to the silicon mass.

Comparing the results for the warm (solid) and cool (dashed) groups in Figure 4.3, we can see that in the cool systems, the IGS contributes relatively more of the metals (especially iron) in the present-day IGrM while the contribution by the galaxies is correspondingly weaker. This is because in the cool systems, transporting the more recently produced metals out of the galaxies (especially the central galaxy) is more difficult as the metal-rich outflows do not travel very far from the galaxies and when they are halted, they shock-heat to temperatures coinciding with the broad peak in the cooling curve, cool rapidly and fall back into the galaxies. In the warm systems, outflows are more energetic and a larger fraction of them shock-heat to temperatures beyond the broad peak where cooling rate becomes comparatively low. A larger fraction of the ejected metals in the cool groups end up in the cold phase (ISM or stars) than in the warm groups.

For the gas that is enriched and flushed out of the galaxies and into the IGrM by galactic outflows, the "environment" in which it is enriched need not to be the same as the one it is expelled from. For instance, let us consider the case of an initially

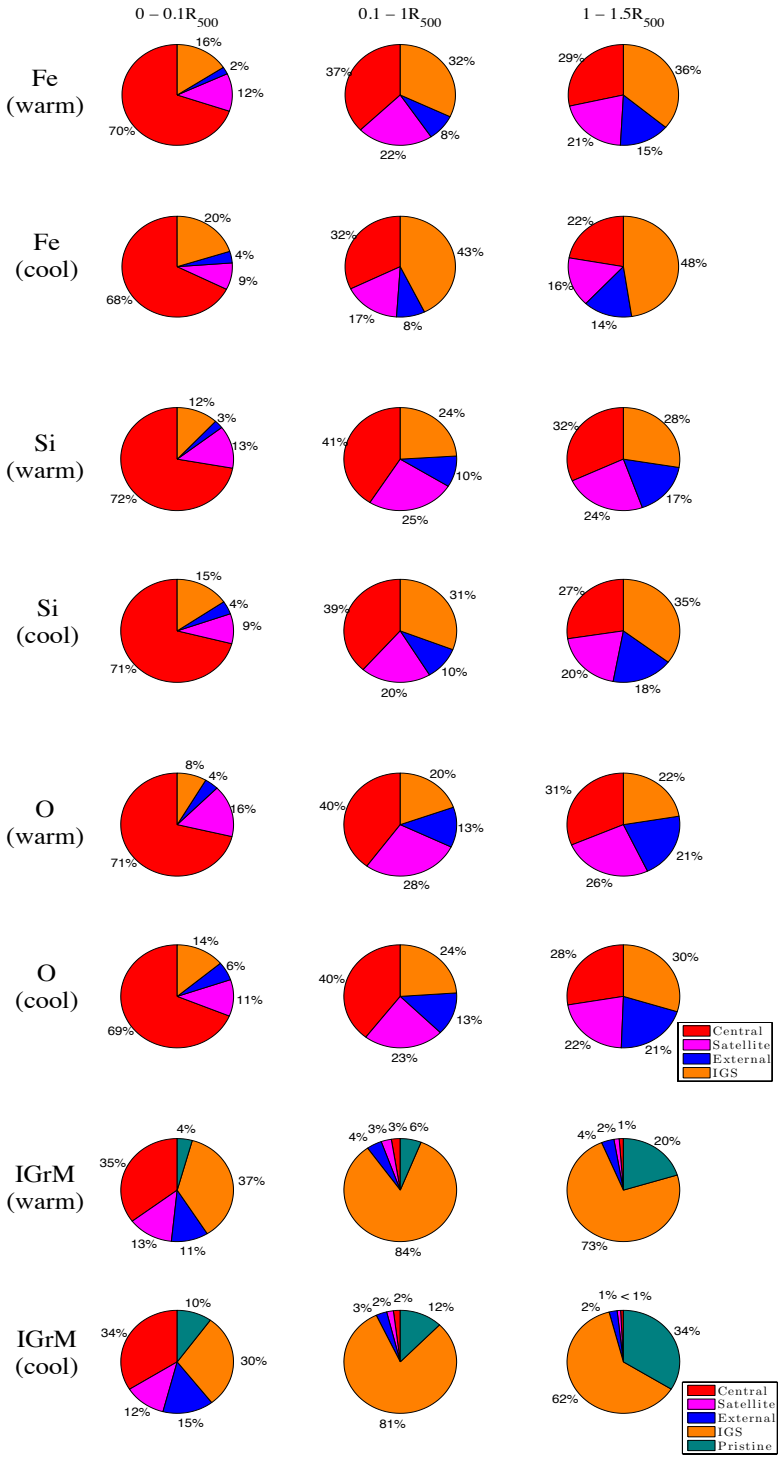

Figure 4.5: The top six rows of pie charts show the metal budget of the present-day IGrM within the four radial bins, classified according to their location at the time when they were injected into the IGrM. The color scheme is the same as that in Figure 4.3. The results for the three different metal elements and the warm and cool groups are explicitly shown. The two bottom rows show the mass fraction of the IGrM that has been injected from the central (red), satellite (magenta) and external (blue) galaxies. The orange segments illustrate the fraction of the IGrM that was not released from galaxy, but has non-primordial metal abundances. This is gas predominantly enriched by the IGS. The green segments represent the pristine gas with primordial abundances (*i.e.,* X=0.25 and Y=0.75).

"external" galaxy that at a later time is incorporated into a group and becomes a "satellite". Some of the metals produced while the galaxy is an "external" may enter the IGrM after the galaxy becomes a "satellite galaxy". In the lower panels of Figure 4.3, we show the fractional contribution of the present-day IGrM metals by various categories but here the classification is based on the local conditions at the time when redthe metals were ejected into the IGrM. Also in Figure 4.5, we show the integrated fractional contributions by these categories over the same radial bins adopted in Figure 4.4 and separately present the results for the warm and cool groups as well as the three different elements as labelled.

Comparing the top and bottom panels of Figure 4.3, it is immediately apparent that the amount of metals ejected from one class of galaxies is considerable different from the amount synthesized within the same category. For example, we can see that over $r = 0$ to $r = 2R_{500}$, the amount ejected from the central and satellite galaxies is higher than that synthesized within these galaxies, whereas for the external ones, the former is lower. Comparing the corresponding pie charts in Figure 4.4 and Figure 4.5, we find that for the warm groups (odd rows), the difference between the two classifications for the central galaxies amounts to 11% (12% vs. 16%), 7% (9% vs. 10%), and 5% (6% vs. 8%) of the total iron (silicon vs. oxygen) mass within $0 \leq r < 0.1R_{500}$, $0.1R_{500} \leq r < R_{500}$, and $R_{500} \leq r < 1.5R_{500}$, respectively. The difference for the cool groups is very similar. These numbers refer to the amount of metals that were synthesized by the stars out of the central galaxies but later entered (via galaxy merger) and were flushed out of the central galaxies through outflows. The trend of decreasing discrepancies between the two classifications with increasing $r(z = 0)$ is due to the fact that the wind particles at larger $r(z = 0)$ were on average ejected at earlier epochs, as we will discuss in more detail in Section 4.2.2. This fact, in turn, indicates that they have less chance of being enriched by some early non-central galaxies. For the satellite galaxies, we find that the amount of iron (silicon, oxygen) injected from these systems into the IGrM is higher than the amount injected by the stars within them. For the warm groups, the difference is $< 1\%$ (1% vs. 1%), 4% (4% vs. 6%), and 6% (5% vs. 6%) of the total iron (silicon vs. oxygen) mass within the three chosen radial bins. These discrepancies are attributed to the amount of the metals synthesized by the stars within some external galaxies and the unbound field stars outside of the MMP. The mass of these metals surpasses that of the metals generated within the satellites but later ejected from the central galaxies after merger. Comparing the first column of the two figures, it can be seen that in

the innermost regions ($r \leq 0.1R_{500}$), the metals produced inside the external galaxies are barely ejected directly from those galaxies. At $0.1R_{500} \leq r < R_{500}$, more than half of the metals injected from the stars within the external galaxies were ejected into the IGrM after the galaxies became incorporated into the MMP. The external galaxies only become the dominant source of the IGrM metals in the $z = 0$ groups at $r \gtrsim 1.5R_{500}$ ($\approx R_{200}$), with regards to the the local conditions at the time when the metals entered the IGrM.

It should be noted that the "IGS" category (orange) in the lower panels of Figure 4.3 (also in Figure 4.5 for the integrated results) does not include those metals that were at first injected from the IGS, but later accreted onto and ejected from a galaxy. They are instead classified to the category associated with that galaxy from which they were ejected into the IGrM. In other words, the "IGS" category in the top panels (also in Figure 4.4) is expected to account for a larger fraction of the total metal mass than that in the lower ones (also in Figure 4.5).

The last two rows of pie charts in Figure 4.5 show the mass fraction of the IGrM divided by the various categories as labelled. The red, magenta and blue segments show the fraction of the IGrM that has been processed (enriched while bound) and ejected by the central, satellite and external galaxies, respectively. Like in the pie charts above, the particles that have been ejected by multiple times as wind are classified based on the last ejection event right before they entered the IGrM. We can see that the processed IGrM accounts for a decreasing fraction of the total IGrM mass with increasing $r(z = 0)$ — within the four selected radial bins, from the center to the outskirt, the processed IGrM accounts for 59%, 10%, 7% and 5% of the IGrM mass in the warm groups, and 60%, 7%, 4% and 3% in the cool groups. That the distribution of the metal-rich processed wind material in the present-day IGrM is more concentrated towards the group center than that of the overall IGrM mass is one important (but not the only) reason for the groups' abundance gradients (see Figure 4.1). Except in the most inner radial bin ($r < 0.1R_{500}$), the processed IGrM merely accounts for a few percent of the total IGrM mass, while the majority of the IGrM has never ever been processed by any galaxy over cosmic time. Comparing the corresponding pie charts in the last two rows, we find that the cool groups contain a smaller fraction of the processed IGrM. This is, in part, due to relatively more efficient radiative cooling of the metal-rich, wind material ejected from the central and the satellite galaxies in the cool groups. Apart from that, because of the relatively shallower potential wells and weaker viscous drag in less dense environments,

the galaxies within and surrounding the cool groups ejected the outflows to further distance (in terms of the virial radius of the group) from the group center at early epochs, before they became incorporated into the groups. More of the ejected particles from those galaxies end up in the intergalactic environments by the present day. The higher mass fraction of the processed IGrM in the $z = 0$ warm groups results in their exhibiting higher metal abundance profiles compared to the $z = 0$ cool groups (see the middle panel of Figure 4.1).

The wind material ejected from the different types of galaxies has distinct metal abundances. From Figure 4.5, it can be seen that the central (external) galaxies contribute comparatively more (fewer) metals per unit gas mass. For example, within $0.1R_{500}$ of the warm groups (see the left panel of the second last row), 35% of the IGrM was ejected from the central galaxies, and it contains 70% of the total iron in that region (see the top left panel). The gas ejected from the satellite galaxies accounts for 13% of the total IGrM mass, yet this portion of gas only contains 12% of the total iron. For the external galaxies, 11% of the total IGrM containing only 3% of the total iron mass.

Figure 4.6 shows the histograms for the number distribution of the present-day IGM particles' iron abundance.[3] We explicitly show the results for the particles ejected from the resolved central (red), satellite (magenta) and external (blue) galaxies as well as for those particles that have never been processed by any galaxy but are identified to have been enriched by the IGS in the MMP (orange). The results for the four previously used radial bins are separately shown in the four different panels of the figure as labelled. And in each panel, we also show the histograms for all the enriched IGrM particles with non-zero iron abundance is shown by the black histograms. Note that in the top right and the two bottom panels, the number of the IGrM particles ejected from the galaxies is artificially increased by five times for the clarity of the illustration. The number/mass fraction of the galaxy-processed IGrM particles is as low as a few percent at large $r(z = 0)$ (*c.f.,* Figure 4.5).

It is revealed by Figure 4.6 that in all the radial bins, the gas ejected from the central galaxies has relatively the highest iron abundance whereas that from the external ones has the lowest. This, in part, arises from the galaxy mass-metallicity relation. The central (external) galaxies from which the gas was ejected are on average more (less) massive than the satellite galaxies, and therefore the winds ejected

[3]The results for the other two elements are qualitatively similar and provide no additional physical insights. We therefore choose iron as a representative case.

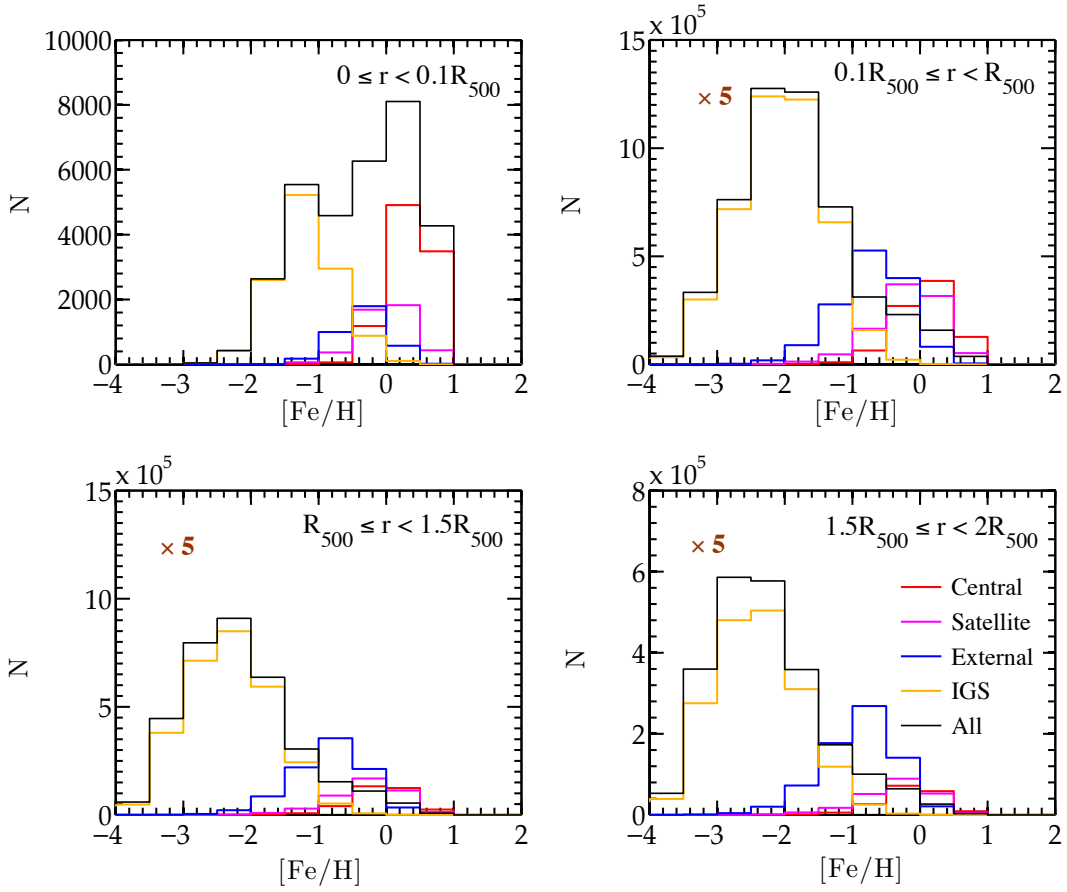

Figure 4.6: The number distribution of the iron abundance of all the IGrM particles in the simulated present-day groups (warm+cool). The four panels show the IGrM particles within the four different radial bins as labelled. The red, magenta and blue histograms represent the distribution for the particles most recently ejected from the resolved central, satellite and external galaxies, respectively. The orange histograms represent the distribution of the particles that have never been processed (enriched while being bound) by any galaxy in the simulation but have been enriched by the IGS within the MMP. The black histograms show the distribution of all the IGrM particles having non-primordial metallicities. In the top right and the two bottom panels, the number of the particles ejected from the galaxies has been artificially increased by five times for clarity of the illustration. In each panel, the black histogram is not equivalent to the sum of the four colourful histograms in that there are IGrM particles enriched by the un-resolved galaxies as well as the unbound field stars outside of the MMP.

from them are expected to be relatively more (less) enriched, given that the abundances of the winds, in our simulation, are essentially the same as those of the ISM of the parent galaxies from which the winds were ejected. Apart from the metal-rich galaxy-processed particles, there are a significantly larger number of particles identified to have been enriched by the IGS in the MMP and they have significantly lower abundances than the galaxy-processed particles. They account for the majority of the IGrM mass within R_{200} ($\sim 1.5R_{500}$), as is shown in the last two rows of pie charts in Figure 4.5.

Comparing the four different panels in Figure 4.6, it is interesting to see that for the same class of particles, there is a trend of decreasing median abundance with increasing $r(z = 0)$. For the "Central" category, the median gas abundance is ~ 2 solar within $0.1R_{500}$ (top left panel) to ~ 0.6 solar at $1.5R_{500} \leq r < 2R_{500}$ (bottom right panel); the "Satellite" category, from ~ 1 to ~ 0.65 solar; the "External" category, from ~ 0.6 to ~ 0.15 solar; and for the "IGS" category, from ~ 0.05 to < 0.01 solar. The trend of the "IGS" category is simply because of the higher concentration of the diffuse IGS toward the group center compared with the IGrM mass in the groups, which indicates that an IGrM particle at smaller $r(z = 0)$ has a higher chance of being enriched by the neighbouring IGS. For the three galaxy-associated categories, intuitively, the observed trend could be a signature of the gas at larger radius having been processed by smaller galaxies in the past, given the mass-metallicity relation. Apart from that, this could also indicate that the gas there was processed by much earlier galaxies, knowing that the ISM in the later galaxies has more chance of being recycled by earlier galaxies in the past and therefore becomes more enriched. Where and when the processed IGrM was enriched by and ejected from the galaxies are the focus of the following subsection.

4.2.2 Where and when was the gas enriched/ejected?

After examining the sources of the metals in the present-day IGrM and their fractional contribution, we now turn to elucidate when and where the metals were injected from the stars. For those that were flushed out of the galaxies through the winds, we are curious about when and where they were flushed out, and how they have been transported to their present-day location. Answering these questions provides insights into the evolution of the abundance profiles of the IGrM in the groups.

Following the approach of Crain et al. (2013) (also see Wiersma et al. 2010 and

Shen et al. 2012), we define the "enrichment radius" and the "ejection radius" as

$$R_{\rm Fe} = \frac{\Sigma_i \Delta m_{\rm i,Fe} r_i}{\Sigma_i \Delta m_{\rm i,Fe}}. \tag{4.1}$$

For the "enrichment radius", i in the above equation sums over all enrichment events, $\Delta m_{\rm i,Fe}$ is the iron increment per event, and r_i is the radial distance (in physical coordinate instead of comoving) of the enriched particle to the centre of the group (or its MMP) at the time of enrichment. A single IGrM particle can be counted for multiple times if it is identified to be associated to several enrichment event. For the "ejection radius", i instead sums over all the ejected particles, $\Delta m_{\rm i,Fe}$ represents the iron mass in that particle at the time of ejection, and r_i is the particle's radial distance at the time of ejection. In this case, an ejected particle is counted only for once. The group center is defined as the position of the most gravitationally bound dark matter particle within the group.

Likewise, we also make a quantitative diagnosis elucidating when the present-day IGrM was enriched and when the metals were ejected into the IGrM from the galaxies by defining the "enrichment redshift" and the "ejection redshift", respectively, as

$$Z_{\rm Fe} = \frac{\Sigma_i \Delta m_{\rm i,Fe} z_i}{\Sigma_i \Delta m_{\rm i,Fe}}, \tag{4.2}$$

where z_i is the redshift at which an enrichment event/ejection occurs.

It is perhaps necessary to clarify at this point that the time and place at which the gas is enriched is not equivalent to when and where the injected metals are synthesized. First of all, for the low mass stars, the lag between when metals are produced — which occurs deep in the stars — and the time when the metals are released by stellar winds can be as long as a few Gyrs. Moreover, it is known that there is significant gas recycling by star formation, such that the mass loss from the old stars can be the fuel of the new generations of stars, and the metals injected from a star particle in the simulation could have been synthesized at much earlier epochs and in difference environments. Our simulation, like many others, does not take record of when and where the metals are synthesized within the stars.

In Figure 4.7, we show $R_{\rm Fe}$ (top row) and $z_{\rm Fe}$ (second row) for the iron in the present-day IGrM, against the present-day radial distance to the group center, $r/R_{\rm vir}(z = 0)$. In the left and right panels, the quantities are defined based on the conditions of the particles at the time of enrichment and ejection, respectively. We show the results for the overall iron (back curves) in the IGrM as well as the binned results for

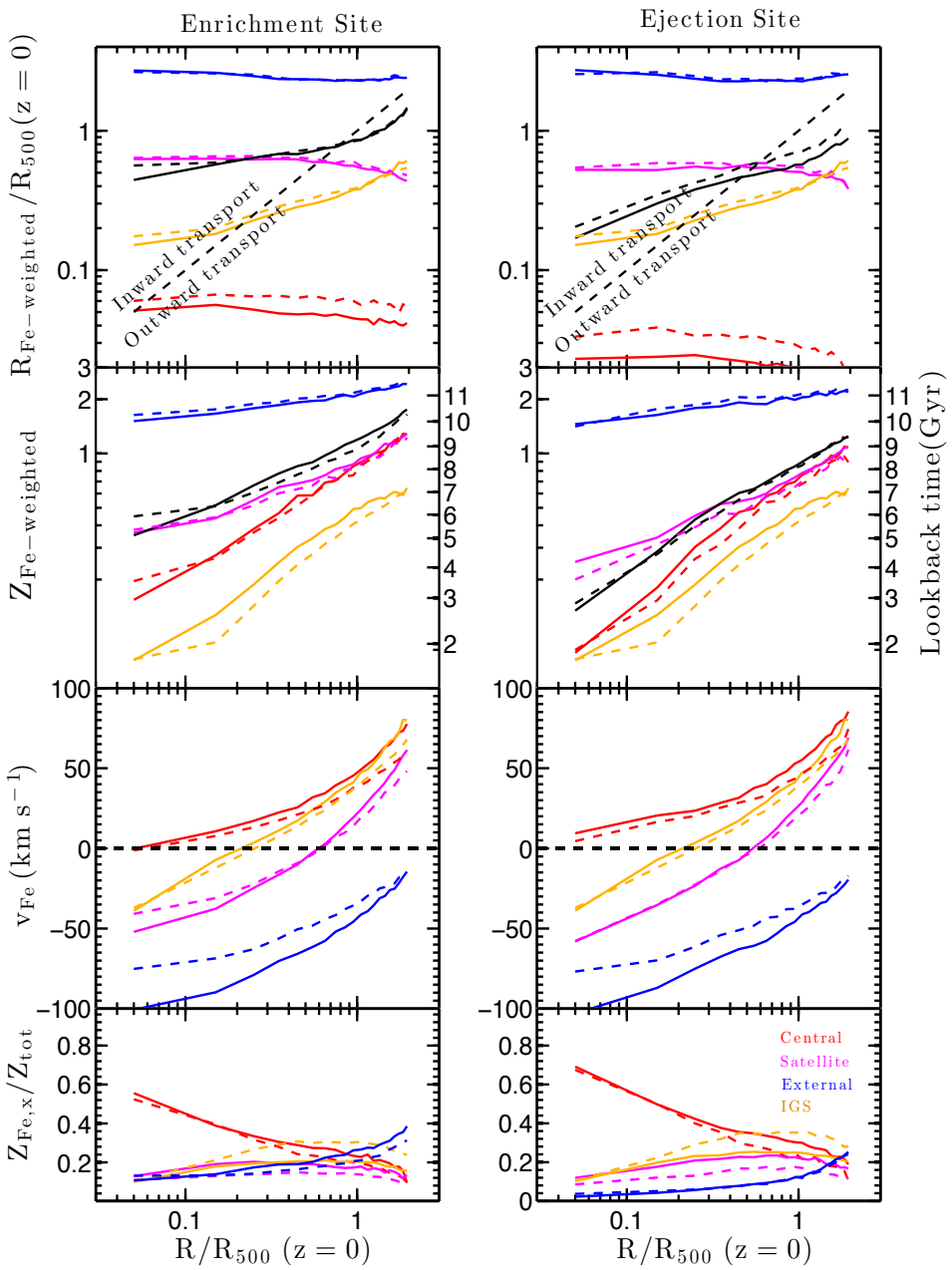

Figure 4.7: First row: The sites of enrichment (left) and ejection (right) for the iron in the present-day IGrM, against its present-day distance to the group centre. The definition of the enrichment and ejection sites is described in detail in Section 4.2.2. The red, magenta, and blue curves show the result for the iron associated with the resolved central, satellite, external galaxies, respectively, while the orange orange curves mark the result for the iron contributed by the IGS. The black dot-dash lines mark the one-to-one loci, which represent the condition where the enrichment (ejection) site is the same as the present-day location of the iron. Second row: The left and right panels show the epochs of enrichment and ejection, respectively, the definition of which is described in detail in Section 4.2.2. The classification of the iron is done in the same way as in the top two panels. Third row: The left and right panels show the averaged velocity at which the iron migrated from the enrichment site and the ejection site, respectively, to the present-day location. Bottom row: The left and right panels are the same as the top and bottom left panels in Figure 4.3, respectively. We separately show the results for the warm (solid) and cool (dashed) groups in all the panels.

the enrichment categories introduced in Section 4.2.1. The results for the warm and cool groups are exhibited by the solid and dashed curves, respectively. The dashed diagnostic black line in the top two panels marks the $R_{\rm Fe} = r(z = 0)$ locus, denoting the situation where the gas is enriched/ejected at the same place as where it locates at present day. The area below the locus indicates that the gas is enriched/ejected at some smaller radii and then transported outwards to its current location, while the area above represents inward motion. And finally, we note that only the results for iron are presented because those for the other two elements are quantitatively similar and provide no additional valuable insights.

Focusing on the top left panel, it can be seen that the iron synthesized by the central galaxies (red) was, as expected, synthesized close to the group centre and later transported outwards to larger distances. The "Satellite" category (magenta), on the contrary, shows mild correlation between $R_{\rm Fe}$ and $r(z = 0)$. Its curves intersect with the one-to-one locus at $r \approx 0.6R_{500}$, indicating that the iron at $r \lessapprox 0.6R_{500}$ in the $z = 0$ groups has been transported, on the average, inwards whereas the iron at the larger distances was transported outwards. The "External" category (blue), by definition, represents the enrichment occurring within the galaxies outside the group or its MMP and it is therefore not surprising to see that its curves lie beyond $2R_{500}$ ($\approx R_{\rm vir}$). Finally, the "IGS" category (orange) shows a mild positive correlation between $R_{\rm Fe}$ and $r(z = 0)$, with $R_{\rm Fe}$ increasing from $\sim 0.16R_{500}(z = 0)$ in the core regions to $\sim 0.4R_{500}(z = 0)$ on the outskirts and the curves intersecting with the one-to-one locus at $r \approx 0.2R_{500}(z = 0)$. The enrichment occurred at fairly inner regions, as it is where stripping by the tidal interactions and mergers is most efficient in the groups. The overall trend (black) is that the iron in the present-day IGrM within $0.8R_{500}$ is, on the average, characterized by inwards motion while that at larger distances is by outwards motion.

Turning to the top right panel, it is interesting to see that $R_{\rm Fe}$ defined based on the ejection conditions is essentially the same as that for the enrichment conditions (top left panel) for each individual category. However, for the overall iron in the IGrM (black curves), the ejection sites are, on the average, closer to the group center. This is because the weighting by different categories is different. As we have discussed in the previously, a larger (smaller) amount of metals were ejected from the central (external) galaxies into the IGrM via outflows than were actually released by the stars within the same class of galaxies. This can also be straightforwardly seen from the bottom panels of Figure 4.7 (the same as the left panels in Figure 4.3).

The second row of panels reveal that the enrichment of the IGrM proceeds, in general, in a "outside-in" fashion, such that the metals in the more diffuse IGrM at larger radial distances in the present-day groups were released from the stars (left panel)/ejected into the IGrM (right panel) at relatively earlier redshifts.

Focusing first on the left panel, it can be seen that the metals at $r \lesssim 0.1R_{500}$ in the $z = 0$ groups were on average injected from the stars to the gas phase in the last 6 Gyrs, and those at R_{500} were released over 9 Gyrs ago. The same "outside-in" fashion has previously been pointed out by Wiersma et al. (2010), in the enrichment of the intergalactic medium, and Crain et al. (2013), in that of the circum-galactic medium, and our result seems to show that this trend continues on the group-scale. It also suggests that the IGrM within R_{500} of the present-day groups is enriched *after* the groups form, *i.e.,* when the groups assemble half of their present-day mass, which happens about $8 - 9$ Gyrs ago (*c.f.,* Figure 13 of Chapter 3). Turning to the individual categories, it can be seen that each of them follows the same "outside-in" trend as the overall iron mass. The gas enriched within the external galaxies (blue) were, as expected, enriched at the earliest epochs among all categories — 10 Gyrs ago for metals at all radii. It can be seen that the metals synthesized within the central (red) and satellite (magenta) galaxies are younger than the average, whereas those produced by the external galaxies (blue) are, as expected, synthesized at much earlier epochs — over 10 Gyrs ago for metals at all radii. For the "Central" category (red), this "outside-in" trend is a clear signature of outward transport of metals, insomuch as the metals at further distance would have spent longer period of time to get transported to their present-day location. For the "Satellite" category (magenta), we observe the same but milder correlation between $Z_{\rm Fe}$ and $r(z = 0)$, and compared with the "Central" category, it appears to be chemically older. Finally, it is interesting to see that the iron injected from the IGS was, on the average, ejected most recently among all the categories, which is not surprising, as the delayed Type Ia SNe and AGB stars in the field become effective source of iron only at late epochs.

Looking at the right panel, the ejection redshift vs. $r(z = 0)$ relation of each of the three galaxy-related categories displays similar feature as the corresponding curve in the left panel, yet shows an offset towards the low-z direction. The offset is a signature of the lag in ejection, that a gas particle could be processed (bound to and enriched) within different galaxies for multiple times, which is frequently observed in massive galaxies and at low redshifts (see Oppenheimer & Davé, 2008; Oppenheimer et al., 2010). The ejection time shown in the right panel only records the last ejection

event for each ejected particle so therefore is supposed to be later than the averaged enrichment time. In detail, the discrepancy between the two red curves is greater in the core regions than on the groups' outskirts, which indicates that the gas at the inner regions, being ejected at more recent epochs, has a larger chance and longer history of being recycled by the central galaxies. It is perhaps surprising to notice that the two magenta curves also display quite significant discrepancy — the ejection curve in the right panel is $0.5-1$ Gyr lower. One might naively think that this is an indicator of gas recycling within the satellite galaxies, yet we have checked and confirmed that this could rarely happen. A fraction of the gas enriched within the satellite galaxies was later ejected from the central galaxies after merger, and on average, that is the part of gas that was enriched much earlier as it has gone through a longer period of time to enter the central galaxies, be ejected, and travel to its present-day location. In the right panel, the magenta curve does not include this early-enriched gas that was eventually ejected from the central galaxies.

Another important problem is how fast the metals have traveled to their present-day radius from the place where they were injected by the stars, and ejected by the galaxies via wind. An order of magnitude calculation can be done simply by dividing $r(z=0) - R_{\rm Fe}$ by $t_{\rm Fe}$ (the look back time corresponding to the enrichment/ejection redshift). In the third row of panels in Figure 4.7, we show the resulting quantity, $v_{\rm Fe}$, as a function of $r(z=0)$. Positive $v_{\rm Fe}$ in the two panels indicates outward transport, corresponding to the area below the one-to-one locus in the top panels, whereas negative $v_{\rm Fe}$ represents inwards motion, and to the area above the locus. In general, we see that the metals in the IGrM migrate at a few 10 km s^{-1} within the groups. Examining the individual categories, it is perhaps worth-noting that the transport speed of the in-situ wind enrichment (*i.e.,* "Central" and "Satellite" categories) is comparable with that of the gas enriched by the IGS. The key is that the metals injected from the IGS are not driven by the outflows so therefore the feature pointed out strongly indicates that the merger-induced convection, instead of the wind ejection, is the dominant mechanism for transporting the metals to their present-day location in the groups.

4.3 Conclusions

The main findings of this chapter are as follows.

(i) Our simulation produces iron abundance profiles that broadly match the observation data, except that in the innermost regions ($R \lesssim 0.1R_{500}$), the simulated abundances are more concentrated, due to the overproduction of stars in the groups' central galaxy. The flattened shape of the $Z_{\rm Si}/Z_{\rm Fe}$ profiles out to R_{500} is consistent with the recent *Suzaku* observations.

(ii) Under the schema of the momentum-driven wind, the produced iron abundance profiles show increasing concentration with decreasing redshift at $z \gtrsim 1$. This is because of the wind particles ejected from the central as well as infalling galaxies becoming confined to a smaller fraction of the virial radius of the parent halos, ram-pressure stripping being more efficient at inner regions where density is higher, and the re-accretion of processed, enriched gas that are ejected at higher redshifts.

(iii) We find that from $z = 3$ to $z = 0$, the $Z_{\rm Si}/Z_{\rm Fe}$ of the hot gas within $R_{\rm vir}$ declines by $\sim 15\%$. Knowing that the Type II SNe dominate the silicon production based on our cosmic chemical model (see OD08). The $Z_{\rm Si}/Z_{\rm Fe}$ of the hot gas at $z = 3$ is essentially the combined yields of the Type II SNe and the prompt Type Ia SNe, we estimate from the decline of $Z_{\rm Si}/Z_{\rm Fe}$ that the delayed Type Ia SNe contribute roughly 1/7 of the iron in the present-day IGrM. The decline of the $Z_{\rm Si}/Z_{\rm Fe}$ of the hot halo gas extends to $\sim 4R_{500}$, beyond which the $Z_{\rm Si}/Z_{\rm Fe}$ is essentially unchanged.

(iv) The IGrM in the present-day groups is dominated by the gas that has never been processed (bound and enriched) by any galaxy during the assembly history of the groups. The overall mass fraction of the galaxy-processed IGrM shows strong gradient against radius, declining from above 50% at $r \leq 0.1R_{500}$ to $\sim 5\%$ at $r = 2R_{500}(\approx R_{\rm vir})$. The warm groups have a higher fraction of the IGrM processed by the galaxies than the cool groups, accounting for the higher abundance profiles.

(v) The metals found in the IGrM can be synthesized by the stars within the central, satellite galaxies of the groups' most massive progenitors (MMP), the external galaxies outside the MMPs, as well as by the diffuse and unbound intra-group stars (IGS). We find that the central galaxies dominate the production of the metals in the IGrM from the group centre to $\sim R_{500}$, and the metals in the outer regions are more synthesized by the external galaxies. The satellite galaxies are

important but sub-dominant contributors to the metals at all radii in the groups. And importantly, we find that the IGS contribute nontrivial amount of iron in the IGrM. The IGS account for relatively lower fraction of the oxygen and silicon mass in the $z = 0$ IGrM than the iron. This results from the fact that the enrichment associated with the IGS, being old stellar populations stripped from the galaxies, is primarily due to the metals from the delayed enrichment from the Type Ia SNe and the AGB stars.

(vi) Finally, we find that the enrichment of the IGrM follows an outside-in fashion, that is, the IGrM in the more inner regions is enriched at later epochs by various resources than at larger distances. There is a trend of outward transport of the IGrM metals over the assembly history of the groups, of which the average speed is a few 10 km s^{-1}. The metal transport in the IGrM is more driven by the merger-induced gas convection inside the groups.

Chapter 5

SUMMARY AND FUTURE OUTLOOK

A wealth of observational and theoretical studies have advanced galaxy groups as the best candidates for studying the very processes associated with galaxy formation and evolution. The hot and diffuse gaseous component that permeates the group halos, or the intra-group medium (IGrM), is accessible to X-ray observations, and its observable properties provide very important constraints to these processes. This dissertation represents one such effort, where we examine the growth and chemical enrichment of the IGrM using the cosmological simulation that includes a well-constrained prescription for large-scale, momentum-driven, galactic outflows powered by stars and supernovae, as well as a sophisticated model for cosmic chemical evolution. Our wind and chemical models have previously been shown to be very successful at reproducing the intergalactic medium (IGM) observations simultaneously with a range of galaxy observables (e.g. Oppenheimer & Davé, 2009; Davé, Oppenheimer & Finlator, 2011). Extending the study to galaxy groups, Davé, Oppenheimer & Sivanandam (2008) found that it could also yield both the iron abundance and the oxygen-to-iron ratio of the present-day IGrM that well match the observations. Nevertheless, the simulation produced more stars in the groups than observed, indicating that another feedback mechanism, such as AGN feedback, should be introduced to provide further quenching of star formation. We follow the work by DOS08, to investigate in greater detail how the enrichment of the IGrM proceeds based on the simulation schemes, how much the excessive star formation in the groups would affect the robustness of the success, and hope to get better constraints to the nature of AGN feedback.

In the "Conclusions" sections of the two main chapters (Chapter 3 and 4), we provide a detailed description of all our findings. Here in this Chapter, we only summarize the most important of them:

• Our simulation with momentum-driven outflows is very successful at regulating the stellar mass of the group galaxies at $M_* < 10^{11}\ M_\odot$; however, we also find galaxies — typically, one per group and invariably, the group central galaxy — that has much larger stellar mass than any observed galaxy. The excess stellar mass of the groups is, in contrast with expectations, *not* owing to catastrophic cooling of the IGrM, but rather the build-up of cold gas in those massive galaxies *before* they are incorporated into the groups. Our finding suggests that in order to reduce the stellar mass fraction to match the observed data, the required additional feedback mechanism must be powerful enough to expel a significant fraction of the emerging halo gas component from the galactic halos.

• The simulated hot gas fraction of the simulated $z = 0$ groups is in broad agreement with the observations, except perhaps that in the rich group regime, it is slightly higher than the latter. This results in several scaling relationships, depending on the structure and state of the IGrM, fitting fairly well with the observational results, but for the most massive groups tending to be more luminous in X-ray than are observed. This indicates that the stellar-powered outflows become ineffectual and a required additional feedback mechanism is needed to effectively puff the hot IGrM to more extended configuration in those massive systems. Comparing the groups at different redshifts, we notice that for groups with comparable temperature (depth of potential well), the IGrM mass fraction increases between $z = 3$ to $z = 1$, as the efficacy of galactic winds to maintain an extended hot gas distribution via heating declines during this period. This evolution of IGrM mass fraction has imprints upon the scaling relationships over the same time period, the cosmic expansion-corrected X-ray luminosity increases, whereas the corrected core gas entropy declines accordingly as the hot gas becomes more compact in the groups. At $z \lesssim 1$, the hot gas in the groups tends to stabilize, and so do the scaling relationships.

• We find that the simulated iron and silicon abundances of the present-day IGrM, both emission-weighed and mass-weighted, fit fairly well with the observations. We specifically identified the sources of metals in today's IGrM. A rough estimation reveals that even after removing the metals synthesized by the excessive amount of stars in the "over-sized" galaxies, the global abundances are still within the accept-

able range given the uncertainties in the metals yields and supernova rates. The central galaxies dominates the metal production in the central regions, but its fractional contribution declines as a function of distance towards the group centre. A non-trivial amount of metals in the IGrM were synthesized within the galaxies while they were satellites or outside of the group MMP, and they account for larger fractional contribution of metals as it goes to outer regions of the groups. There's clear age gradient, such that metals in the inner regions were produced more recently than those at outer regions. It should be stressed that the IGS in the groups produce significant amount of iron to today's IGrM, via delayed Type Ia SNe and AGB mass loss, and it's relative contribution increases with decreasing group mass.

It is somehow fortunate that though our simulation has failed at reproducing the observed stellar mass fraction of galaxy groups due to lacking AGN, the produced metal content of the IGrM is still in broad agreement with observations, primarily because the amount of metals deposited into the IGrM does not grow linearly with star formation of the galaxies in the groups. For those 'over-sized" galaxies in the groups, the mass outflow rate becomes only a fraction of the star formation rate, indicating that the metals produced within those galaxies are more likely to be locked in stars. Moreover, those galaxies reside in the densest regions in the simulation volume where gravitational and viscous drag are most efficient, so that the wind particles behave more like fountains and therefore very limited fraction of the excessive metals are retained in the IGrM.

Certainly this thesis does not mark the end of the project, but only the first step in a long journey towards faithfully reproducing all, or more safely speaking, as many observables related to galaxy groups (and clusters) by state-of-art simulation techniques. And in order to achieve so, we will continue incorporating the simulation with new prescriptions for the missing physics. These physics may have limited, or only second-order influence on the large-scale distribution of metals in the IGrM (in comparison with the resolution limit of $\sim$5 kpc), which is the main focus of this work, but for many other problems, can be of vital importance — e.g. star formation in the central galaxies, core gas entropy, the observed population of cool-core groups/clusters, the observed scatter in the scaling relationships, etc. Here we list three main problems that currently attract most of our attention:

1. *AGN feedback*

Observational evidence of AGN interacting with the environments has been widely seen, including high-speed winds, jet-induced bubbles, shock fronts and ripples (McNamara & Nulsen, 2007; Fabian, 2012, and references therein). Yet the implementation of AGN feedback in cosmological simulations turns out to be a non-trivial task, given that the accretion of gas onto the blackholes and the coupling of feedback energy with the environments involve a variety of physical processes that operate on spatial scales spanning across many orders of magnitude. To model all these processes *simultaneously* is far beyond the capability of the current cosmological simulations and moreover, many details of these processes are still theoretically and observationally ill-constrained. At present, there is a wide variance in the sub-resolution recipes adopted in different cosmological simulations, lying in five major aspects — 1) how the mass accretion rate onto the blackhole is calculated given the limited resolution; 2) how individual gas particles are "absorbed" by the blackhole in the simulations; 3) how much of the accreted rest mass is returned as feedback energy and the way in which it is returned (i.e. by thermalizing nearby SPH particles or by increasing their momentum); 4) the blackhole advection algorithm (to avoid the blackholes from being inappropriately dragged around by two-body forces); and 5) blackhole merger algorithm — as summarized by Wurster & Thacker (2013). These different recipes often introduce a number of free parameters that are calibrated in an ad hoc fashion to fit the variety of observational results, such as the blackhole growth, the correlations between blackholes and host galaxies, the comic star formation history, and the hot gas and baryonic faction within halos (e.g. Power, Nayakshin & King, 2011; Dubois et al., 2012; Rosas-Guevara et al., 2013; Vogelsberger et al., 2013; Anglés-Alcázar et al., 2015; Crain et al., 2015). A detailed physical understanding of the ad hoc parameterization remains lacking, and is where much progress can be made.

2. *Turbulent mixing*

   As a "classical" particle-based, Lagrangian method, SPH does not include any implicit diffusion of scalar quantities such as metals, leading to artificial inhomogeneities in metal distribution (Wiersma et al., 2009). In nature, however, turbulence is prevalent and is expected to cause mixing of metals between gases. For instance, the ISM is known to be highly turbulent, owing to SN explosions, thermal and gravitational instability (Elmegreen & Scalo, 2004; Mac Low &

Klessen, 2004; Yang & Krumholz, 2012; Petit et al., 2015). Turbulence is also expected to be prevalent in ICM/IGrM given the high Reynold number associated with its violent dynamical motions (Fujita, Takizawa & Sarazin, 2003). As for the IGM, the strongest recent evidence of turbulence is from the study of low-z O_{VI} absorption (Oppenheimer & Davé, 2009; Oppenheimer et al., 2012). One would also anticipate that the large shear velocity between the outflowing material in the winds and the ambient halo gas is likely to drive turbulence via Kelvin-Helmholtz instability, leading to metal mixing. There are recent attempts to impose sub-grid recipes for turbulent diffusion into the hierarchical galaxy formation models (e.g. Greif et al., 2009; Shen, Wadsley & Stinson, 2010), but it still remains unclear how efficiently metals can mix on different scales and in different environments, since the related physical processes are still poorly understood. And moreover, we are also particularly interested in how turbulent mixing promotes heat transfer in the IGrM/ICM, the interplay between turbulence, magnetic field and cosmic rays, and how this interplay may impact the mixing properties of the IGrM/ICM. There are several important observational projects taking place, or on the horizon, that may advance our knowledge of the detailed gas dynamics in various environments, and out to high redshifts (e.g. *Astro-H*, *ALMA*, *SKA*) (see Somerville & Davé, 2014, for reviews).

3. *Magnetohydrodynamic instabilities*

   The IGrM/ICM is comprised of weakly collisional magnetized plasma where the Coulomb mean free path of the elementary particles is many orders of magnitude larger than their gyroradius, and the conductive flow of heat is strongly anisotropic with respect to the local magnetic field direction since the thermal collisions across the field lines are largely restricted. The anisotropic conduction in the IGrM/ICM is expected to drive two kinds of convection instabilities: the magnetothermal instability, or MTI (Balbus, 2000; Parrish, Stone & Lemaster, 2008), occurring when temperature increases in the direction of gravity and the heat-flux-driven-buoyancy instability, or HBI (Parrish & Quataert, 2008; Quataert, 2008), with inverted temperature profiles. It has been found that the MTI and HBI instabilities could have profound impact on the thermal conduction in the IGrM/ICM by altering the local topology of the magnetic field. We are interested in its implications for the observed bi-modality of groups/clusters

and the non-thermal pressure support in the IGrM/ICM (Parrish, Quataert & Sharma, 2009, 2010; Parrish et al., 2012).

To summarize, while this simulation has produced thermal and chemical properties of the IGrM in reasonably good agreement with the observations, there is still much work to be done to get many other observable properties of galaxy groups/clusters correct. Adding new improvements to the code could be extremely exhilarating yet challenging, as it requires advancement in observational and numerical techniques, as well as deeper understanding of the core physical processes involved. We are ready to welcome the forthcoming new twists, shocking surprises, and unexpected new discoveries.

Bibliography

Abadi M. G., Moore B., Bower R. G., 1999, MNRAS, 308, 947

Alpaslan M. et al., 2012, MNRAS, 426, 2832

Anders E., Grevesse N., 1989, Geochim. Cosmochim. Acta, 53, 197

Anglés-Alcázar D., Davé R., Özel F., Oppenheimer B. D., 2014, ApJ, 782, 84

Anglés-Alcázar D., Özel F., Davé R., Katz N., Kollmeier J. A., Oppenheimer B. D., 2015, ApJ, 800, 127

Arth A., Dolag K., Beck A. M., Petkova M., Lesch H., 2014, ArXiv e-prints

Babul A., Balogh M. L., Lewis G. F., Poole G. B., 2002, MNRAS, 330, 329

Babul A., Sharma P., Reynolds C. S., 2013, ApJ, 768, 11

Bahé Y. M., McCarthy I. G., Balogh M. L., Font A. S., 2013, MNRAS, 430, 3017

Balbus S. A., 2000, ApJ, 534, 420

Balogh M. L., Babul A., Patton D. R., 1999, MNRAS, 307, 463

Balogh M. L., Mazzotta P., Bower R. G., Eke V., Bourdin H., Lu T., Theuns T., 2011, MNRAS, 412, 947

Balogh M. L., Morris S. L., 2000, MNRAS, 318, 703

Barnes J. E., 1988, ApJ, 331, 699

Bildfell C., Hoekstra H., Babul A., Mahdavi A., 2008, MNRAS, 389, 1637

Binney J., Tremaine S., 1987, Galactic dynamics

Birkinshaw M., 1999, Phys. Rep., 310, 97

Bîrzan L., Rafferty D. A., McNamara B. R., Wise M. W., Nulsen P. E. J., 2004, ApJ, 607, 800

Bösch B. et al., 2013, A&A, 549, A142

Bournaud F., Elmegreen B. G., Teyssier R., Block D. L., Puerari I., 2010, MNRAS, 409, 1088

Bradshaw E. J. et al., 2013, MNRAS, 433, 194

Brook C. B. et al., 2011, MNRAS, 415, 1051

Carlstrom J. E., Holder G. P., Reese E. D., 2002, ARA&A, 40, 643

Carroll S. M., Press W. H., Turner E. L., 1992, ARA&A, 30, 499

Catinella B. et al., 2013, MNRAS, 436, 34

Cavagnolo K. W., Donahue M., Voit G. M., Sun M., 2008, ApJ, 683, L107

Chabrier G., 2003, PASP, 115, 763

Chandrasekhar S., 1942, Principles of stellar dynamics

Connelly J. L. et al., 2012, ApJ, 756, 139

Crain R. A., Eke V. R., Frenk C. S., Jenkins A., McCarthy I. G., Navarro J. F., Pearce F. R., 2007, MNRAS, 377, 41

Crain R. A., McCarthy I. G., Schaye J., Theuns T., Frenk C. S., 2013, MNRAS, 432, 3005

Crain R. A. et al., 2015, MNRAS, 450, 1937

Dalla Vecchia C., Schaye J., 2008, MNRAS, 387, 1431

Dalla Vecchia C., Schaye J., 2012, MNRAS, 426, 140

Davé R., 2009, in Astronomical Society of the Pacific Conference Series, Vol. 419, Galaxy Evolution: Emerging Insights and Future Challenges, Jogee S., Marinova I., Hao L., Blanc G. A., eds., p. 347

Davé R. et al., 2001, ApJ, 552, 473

Davé R., Finlator K., Oppenheimer B. D., 2006, MNRAS, 370, 273

Davé R., Finlator K., Oppenheimer B. D., 2011a, MNRAS, 416, 1354

Davé R., Finlator K., Oppenheimer B. D., 2011b, MNRAS, 416, 1354

Davé R., Oppenheimer B. D., Finlator K., 2011, MNRAS, 415, 11

Davé R., Oppenheimer B. D., Sivanandam S., 2008, MNRAS, 391, 110

De Grandi S., Ettori S., Longhetti M., Molendi S., 2004, A&A, 419, 7

De Grandi S., Molendi S., 2002, ApJ, 567, 163

de Plaa J., Werner N., Bleeker J. A. M., Vink J., Kaastra J. S., Méndez M., 2007, A&A, 465, 345

Diaferio A., 1999, MNRAS, 309, 610

Diaferio A., Geller M. J., 1997, ApJ, 481, 633

D'Odorico V., Cupani G., Cristiani S., Maiolino R., Molaro P., Nonino M., Centurión M., Cimatti, 2013, MNRAS, 435, 1198

Domainko W. et al., 2006, A&A, 452, 795

Dressler A., 1980, ApJ, 236, 351

Dubois Y., Devriendt J., Slyz A., Teyssier R., 2012, MNRAS, 420, 2662

Dubois Y., Teyssier R., 2008, A&A, 477, 79

Eckmiller H. J., Hudson D. S., Reiprich T. H., 2011, A&A, 535, A105

Edge A. C., Stewart G. C., 1991, MNRAS, 252, 414

Edge A. C., Stewart G. C., Fabian A. C., 1992, MNRAS, 258, 177

Egami E. et al., 2006, ApJ, 647, 922

Eisenstein D. J., Hu W., 1999, ApJ, 511, 5

Elmegreen B. G., Scalo J., 2004, ARA&A, 42, 211

Ettori S., 2015, MNRAS, 446, 2629

Ettori S., Fabian A. C., 1999, MNRAS, 305, 834

Evans, II N. J. et al., 2009, ApJS, 181, 321

Evrard A. E., Henry J. P., 1991, ApJ, 383, 95

Fabian A. C., 1994, ARA&A, 32, 277

Fabian A. C., 2012, ARA&A, 50, 455

Fabian A. C., Hu E. M., Cowie L. L., Grindlay J., 1981, ApJ, 248, 47

Fabian A. C., Nulsen P. E. J., Canizares C. R., 1984, Nature, 310, 733

Fabjan D., Borgani S., Tornatore L., Saro A., Murante G., Dolag K., 2010, MNRAS, 401, 1670

Faucher-Giguère C.-A., Quataert E., 2012, MNRAS, 425, 605

Federrath C., Klessen R. S., 2013, ApJ, 763, 51

Finlator K., Davé R., 2008, MNRAS, 385, 2181

Finlator K., Davé R., Papovich C., Hernquist L., 2006, ApJ, 639, 672

Finlator K., Oppenheimer B. D., Davé R., 2011, MNRAS, 410, 1703

Finoguenov A., Ponman T. J., Osmond J. P. F., Zimer M., 2007, MNRAS, 374, 737

Ford A. B., Davé R., Oppenheimer B. D., Katz N., Kollmeier J. A., Thompson R., Weinberg D. H., 2014, MNRAS, 444, 1260

Fujita Y., Ohira Y., 2012, ApJ, 746, 53

Fujita Y., Ohira Y., 2013, MNRAS, 428, 599

Fujita Y., Takizawa M., Sarazin C. L., 2003, ApJ, 584, 190

Fukazawa Y., Makishima K., Tamura T., Ezawa H., Xu H., Ikebe Y., Kikuchi K., Ohashi T., 1998, PASJ, 50, 187

Gabor J. M., Bournaud F., 2014, MNRAS, 441, 1615

Gabor J. M., Davé R., 2012, MNRAS, 427, 1816

Gabor J. M., Davé R., 2015, MNRAS, 447, 374

Geach J. E. et al., 2014, Nature, 516, 68

Giodini S. et al., 2012, A&A, 538, A104

Giodini S., Lovisari L., Pointecouteau E., Ettori S., Reiprich T. H., Hoekstra H., 2013, Space Sci. Rev., 177, 247

Giodini S., Pierini D., Finoguenov A. e., 2009, ApJ, 703, 982

Gonzalez A. H., Sivanandam S., Zabludoff A. I., Zaritsky D., 2013, ApJ, 778, 14

Governato F., Willman B., Mayer L., Brooks A., Stinson G., Valenzuela O., Wadsley J., Quinn T., 2007, MNRAS, 374, 1479

Greif T. H., Glover S. C. O., Bromm V., Klessen R. S., 2009, MNRAS, 392, 1381

Gunn J. E., Gott, III J. R., 1972, ApJ, 176, 1

Haines C. P. et al., 2015, ArXiv e-prints

Haines C. P. et al., 2013, ApJ, 775, 126

Hellwing W. A., Li B., Frenk C. S., Cole S., 2013, MNRAS, 435, 2806

Helsdon S. F., Ponman T. J., 2000, MNRAS, 315, 356

Helsdon S. F., Ponman T. J., 2003, MNRAS, 339, L29

Hinshaw G. et al., 2013, ApJS, 208, 19

Hirschmann M. et al., 2013, MNRAS, 436, 2929

Hoekstra H., Bartelmann M., Dahle H., Israel H., Limousin M., Meneghetti M., 2013, Space Sci. Rev., 177, 75

Hopkins P. F., Kereš D., Oñorbe J., Faucher-Giguère C.-A., Quataert E., Murray N., Bullock J. S., 2014, MNRAS, 445, 581

Hopkins P. F., Quataert E., Murray N., 2012, MNRAS, 421, 3522

Hoyle B., Masters K. L., Nichol R. C., Jimenez R., Bamford S. P., 2012, MNRAS, 423, 3478

Hummels C. B., Bryan G. L., 2012, ApJ, 749, 140

Just A., Khan F. M., Berczik P., Ernst A., Spurzem R., 2011, MNRAS, 411, 653

Kaiser N., 1986, MNRAS, 222, 323

Kaiser N., 1991, ApJ, 383, 104

Katz N., Weinberg D. H., Hernquist L., 1996, ApJS, 105, 19

Kennicutt, Jr. R. C., 1998, ApJ, 498, 541

Kereš D., Katz N., Davé R., Fardal M., Weinberg D. H., 2009, MNRAS, 396, 2332

Kereš D., Katz N., Weinberg D. H., Davé R., 2005, MNRAS, 363, 2

Kettula K. et al., 2013, ApJ, 778, 74

Knobel C. et al., 2009, ApJ, 697, 1842

Komarov S. V., Churazov E. M., Schekochihin A. A., ZuHone J. A., 2014, MNRAS, 440, 1153

Kravtsov A. V., Nagai D., Vikhlinin A. A., 2005, ApJ, 625, 588

Krumholz M. R., Dekel A., McKee C. F., 2012, ApJ, 745, 69

Krumholz M. R., Thompson T. A., 2013, MNRAS, 434, 2329

Kunz M. W., 2011, MNRAS, 417, 602

Kunz M. W., Bogdanović T., Reynolds C. S., Stone J. M., 2012, ApJ, 754, 122

Laganá T. F., de Souza R. S., Keller G. R., 2010, A&A, 510, A76

Laganá T. F., Martinet N., Durret F., Lima Neto G. B., Maughan B., Zhang Y.-Y., 2013, A&A, 555, A66

Larson R. B., Tinsley B. M., Caldwell C. N., 1980, ApJ, 237, 692

Leauthaud A. et al., 2010, ApJ, 709, 97

Leauthaud A. et al., 2012, ApJ, 746, 95

Lewis G. F., Babul A., Katz N., Quinn T., Hernquist L., Weinberg D. H., 2000, ApJ, 536, 623

Limongi M., Chieffi A., 2005, in Astronomical Society of the Pacific Conference Series, Vol. 342, 1604-2004: Supernovae as Cosmological Lighthouses, Turatto M., Benetti S., Zampieri L., Shea W., eds., p. 122

Lin Y.-T., Mohr J. J., Stanford S. A., 2003, ApJ, 591, 749

Lokas E. L., Hoffman Y., 2001, in Identification of Dark Matter, Spooner N. J. C., Kudryavtsev V., eds., p. 121

Mac Low M.-M., Klessen R. S., 2004, Reviews of Modern Physics, 76, 125

Mahdavi A., Hoekstra H., Babul A., Bildfell C., Jeltema T., Henry J. P., 2013, ApJ, 767, 116

Mahdavi A., Hoekstra H., Babul A., Henry J. P., 2008, MNRAS, 384, 1567

Markevitch M., 1998, ApJ, 504, 27

Markevitch M., Forman W. R., Sarazin C. L., Vikhlinin A., 1998, ApJ, 503, 77

Martin C. L., 2005, ApJ, 621, 227

Martin C. L., 2006, ApJ, 647, 222

Maughan B. J., Giles P. A., Randall S. W., Jones C., Forman W. R., 2012, MNRAS, 421, 1583

Mazzotta P., Rasia E., Moscardini L., Tormen G., 2004, MNRAS, 354, 10

McCarthy I. G., Babul A., Bower R. G., Balogh M. L., 2008, MNRAS, 386, 1309

McCarthy I. G., Balogh M. L., Babul A., Poole G. B., Horner D. J., 2004, ApJ, 613, 811

McCarthy I. G., Le Brun A. M. C., Schaye J., Holder G. P., 2014, MNRAS, 440, 3645

McCarthy I. G., Schaye J., Bower R. G., Ponman T. J., Booth C. M., Dalla Vecchia C., Springel V., 2011, MNRAS, 412, 1965

McCarthy I. G. et al., 2010, MNRAS, 406, 822

McCourt M., Quataert E., Parrish I. J., 2013, MNRAS, 432, 404

McDonald M. et al., 2013, ApJ, 774, 23

McNamara B. R., Nulsen P. E. J., 2007, ARA&A, 45, 117

McNamara B. R. et al., 2014, ApJ, 785, 44

Mo H., van den Bosch F. C., White S., 2010, Galaxy Formation and Evolution

Moore B., Katz N., Lake G., Dressler A., Oemler A., 1996, Nature, 379, 613

Muratov A. L., Keres D., Faucher-Giguere C.-A., Hopkins P. F., Quataert E., Murray N., 2015, ArXiv e-prints

Murray N., Ménard B., Thompson T. A., 2011, ApJ, 735, 66

Murray N., Quataert E., Thompson T. A., 2005, ApJ, 618, 569

Nagai D., 2006, ApJ, 650, 538

Nagai D., Kravtsov A. V., Vikhlinin A., 2007, ApJ, 668, 1

Nagai D., Vikhlinin A., Kravtsov A. V., 2007, ApJ, 655, 98

Nagashima M., Lacey C. G., Baugh C. M., Frenk C. S., Cole S., 2005, MNRAS, 358, 1247

Nipoti C., Treu T., Ciotti L., Stiavelli M., 2004, MNRAS, 355, 1119

Oppenheimer B. D., Davé R., 2006, MNRAS, 373, 1265

Oppenheimer B. D., Davé R., 2008, MNRAS, 387, 577

Oppenheimer B. D., Davé R., 2009, MNRAS, 395, 1875

Oppenheimer B. D., Davé R., Finlator K., 2009, MNRAS, 396, 729

Oppenheimer B. D., Davé R., Katz N., Kollmeier J. A., Weinberg D. H., 2012, MNRAS, 420, 829

Oppenheimer B. D., Davé R., Kereš D., Fardal M., Katz N., Kollmeier J. A., Weinberg D. H., 2010, MNRAS, 406, 2325

Osmond J. P. F., Ponman T. J., 2004, MNRAS, 350, 1511

Ostriker J. P., Hausman M. A., 1977, ApJ, 217, L125

Ostriker J. P., Tremaine S. D., 1975, ApJ, 202, L113

O'Sullivan E. et al., 2012, MNRAS, 424, 2971

O'Sullivan E., Kolokythas K., Raychaudhury S., Vrtilek J. M., Kantharia N., 2014, ArXiv e-prints

Parrish I. J., McCourt M., Quataert E., Sharma P., 2012, MNRAS, 422, 704

Parrish I. J., Quataert E., 2008, ApJ, 677, L9

Parrish I. J., Quataert E., Sharma P., 2009, ApJ, 703, 96

Parrish I. J., Quataert E., Sharma P., 2010, ApJ, 712, L194

Parrish I. J., Stone J. M., Lemaster N., 2008, ApJ, 688, 905

Peterson J. R., Kahn S. M., Paerels F. B. S., Kaastra J. S., Tamura T., Bleeker J. A. M., Ferrigno C., Jernigan J. G., 2003, ApJ, 590, 207

Petit A. C., Krumholz M. R., Goldbaum N. J., Forbes J. C., 2015, MNRAS, 449, 2588

Piontek F., Steinmetz M., 2011, MNRAS, 410, 2625

Pipino A., Kaviraj S., Bildfell C., Babul A., Hoekstra H., Silk J., 2009, MNRAS, 395, 462

Planelles S., Borgani S., Fabjan D., Killedar M., Murante G., Granato G. L., Ragone-Figueroa C., Dolag K., 2014, MNRAS, 438, 195

Pope E. C. D., 2010, MNRAS, 404, 451

Pope E. C. D., Babul A., Pavlovski G., Bower R. G., Dotter A., 2010, MNRAS, 406, 2023

Postman M., Geller M. J., 1984, ApJ, 281, 95

Pounds K. A., King A. R., Page K. L., O'Brien P. T., 2003a, MNRAS, 346, 1025

Pounds K. A., Reeves J. N., King A. R., Page K. L., O'Brien P. T., Turner M. J. L., 2003b, MNRAS, 345, 705

Power C., Nayakshin S., King A., 2011, MNRAS, 412, 269

Pratt G. W. et al., 2010, A&A, 511, A85

Pratt G. W., Croston J. H., Arnaud M., Böhringer H., 2009, A&A, 498, 361

Puchwein E., Sijacki D., Springel V., 2008, ApJ, 687, L53

Quataert E., 2008, ApJ, 673, 758

Rasia E. et al., 2012, New Journal of Physics, 14, 055018

Rasmussen J., Ponman T. J., 2007, MNRAS, 380, 1554

Rasmussen J., Ponman T. J., 2009, MNRAS, 399, 239

Revaz Y., Combes F., Salomé P., 2008, A&A, 477, L33

Robotham A. S. G. et al., 2011, MNRAS, 416, 2640

Rosas-Guevara Y. M. et al., 2013, ArXiv e-prints

Rosati P., Borgani S., Norman C., 2002, ARA&A, 40, 539

Rupke D. S., Veilleux S., Sanders D. B., 2005, ApJS, 160, 115

Russell H. R. et al., 2014, ApJ, 784, 78

Saintonge A. et al., 2011, MNRAS, 415, 32

Sales L. V., Navarro J. F., Schaye J., Dalla Vecchia C., Springel V., Booth C. M., 2010, MNRAS, 409, 1541

Sanderson A. J. R., O'Sullivan E., Ponman T. J., 2009, MNRAS, 395, 764

Sasaki T., Matsushita K., Sato K., 2014, ApJ, 781, 36

Sato K., Kawaharada M., Nakazawa K., Matsushita K., Ishisaki Y., Yamasaki N. Y., Ohashi T., 2010, PASJ, 62, 1445

Scannapieco E., Bildsten L., 2005, ApJ, 629, L85

Schaye J. et al., 2015, MNRAS, 446, 521

Schmidt F., Lima M., Oyaizu H., Hu W., 2009, Phys. Rev. D, 79, 083518

Sell P. H. et al., 2014, MNRAS, 441, 3417

Shen S., Madau P., Aguirre A., Guedes J., Mayer L., Wadsley J., 2012, ApJ, 760, 50

Shen S., Wadsley J., Stinson G., 2010, MNRAS, 407, 1581

Simionescu A., 2009, PhD thesis, Ludwig-Maximilians-Universität München

Sivanandam S., Zabludoff A. I., Zaritsky D., Gonzalez A. H., Kelson D. D., 2009, ApJ, 691, 1787

Smith R. K., Brickhouse N. S., Liedahl D. A., Raymond J. C., 2001, ApJ, 556, L91

Sokołowska A., Mayer L., Babul A., Madau P., Shen S., 2015, ArXiv e-prints

Somerville R. S., Davé R., 2014, ArXiv e-prints

Springel V., 2005, MNRAS, 364, 1105

Springel V., Hernquist L., 2003, MNRAS, 339, 289

Stinson G. S., Brook C., Macciò A. V., Wadsley J., Quinn T. R., Couchman H. M. P., 2013, MNRAS, 428, 129

Sturm E. et al., 2011, ApJ, 733, L16

Sun M., 2012, New Journal of Physics, 14, 045004

Sun M., Voit G. M., Donahue M., Jones C., Forman W., Vikhlinin A., 2009, ApJ, 693, 1142

Taranu D. S., Hudson M. J., Balogh M. L., Smith R. J., Power C., Oman K. A., Krane B., 2014, MNRAS, 440, 1934

Teyssier R., Chapon D., Bournaud F., 2010, ApJ, 720, L149

Thompson T. A., Fabian A. C., Quataert E., Murray N., 2015, MNRAS, 449, 147

Tombesi F., Cappi M., Reeves J. N., Palumbo G. G. C., Yaqoob T., Braito V., Dadina M., 2010a, A&A, 521, A57

Tombesi F., Sambruna R. M., Reeves J. N., Braito V., Ballo L., Gofford J., Cappi M., Mushotzky R. F., 2010b, ApJ, 719, 700

Toomre A., Toomre J., 1972, ApJ, 178, 623

Tozzi P., Norman C., 2001, ApJ, 546, 63

Turner M. L., Schaye J., Steidel C. C., Rudie G. C., Strom A. L., 2014, MNRAS, 445, 794

van den Bosch F. C., Aquino D., Yang X., Mo H. J., Pasquali A., McIntosh D. H., Weinmann S. M., Kang X., 2008, MNRAS, 387, 79

van der Burg R. F. J., Muzzin A., Hoekstra H., Wilson G., Lidman C., Yee H. K. C., 2014, A&A, 561, A79

Vanderlinde K. et al., 2010, ApJ, 722, 1180

Veilleux S. et al., 2013, ApJ, 776, 27

Vikhlinin A., Kravtsov A., Forman W., Jones C., Markevitch M., Murray S. S., Van Speybroeck L., 2006, ApJ, 640, 691

Vikhlinin A. et al., 2009, ApJ, 692, 1060

Villar Martín M., Emonts B., Humphrey A., Cabrera Lavers A., Binette L., 2014, MNRAS, 440, 3202

Vogelsberger M., Genel S., Sijacki D., Torrey P., Springel V., Hernquist L., 2013, MNRAS, 436, 3031

Voit G. M., Bryan G. L., 2001, Nature, 414, 425

White S. D. M., Efstathiou G., Frenk C. S., 1993, MNRAS, 262, 1023

Wiersma R. P. C., Schaye J., Dalla Vecchia C., Booth C. M., Theuns T., Aguirre A., 2010, MNRAS, 409, 132

Wiersma R. P. C., Schaye J., Theuns T., Dalla Vecchia C., Tornatore L., 2009, MNRAS, 399, 574

Williams C. C. et al., 2014, ApJ

Wurster J., Thacker R. J., 2013, MNRAS, 431, 2513

Yang C.-C., Krumholz M., 2012, ApJ, 758, 48

Zel'dovich Y. B., 1970, A&A, 5, 84

Zeldovich Y. B., 1972, MNRAS, 160, 1P

Zhu G., Zheng Z., Lin W. P., Jing Y. P., Kang X., Gao L., 2006, ApJ, 639, L5